Aerodynamic Study of a Strut and a Row of Guide Vanes in Tandem Configuration

by

Andrei Bronipolsky

A thesis submitted to the Faculty of Graduate and Postdoctoral Affairs
in partial fulfillment of the requirements for the degree of

Master of Applied Science
in
Mechanical Engineering

Carleton University
Ottawa, Ontario

Abstract

This thesis aimed to study the aerodynamic interaction of a strut and a row of guide-vanes located in the inter-turbine duct (ITD) of a typical turbofan gas-turbine engine through experiments and numerical analysis in the context of optimizing their relative positioning to minimize the total profile loss. The study was intended to use numerical analysis to determine promising axial and pitchwise positions of the strut relative to the guide-vane row to create a test matrix for further experimental study. For this analysis, the Baseline Reynolds-stress turbulence model was used in a series of benchmarking exercises using published and experimental low-speed wind-tunnel data. The RANS-based BSL Reynolds-stress model was found to be limited in its ability to accurately generate the flow physics in a free-shear layer despite being capable of approximating the momentum thickness in the wake of a strut and a row of guide-vanes in tandem configuration and the mixing-layer growth rate of a planar turbulent free-shear layer. The study also presents the design of a rectilinear test section, to facilitate future aerodynamic studies of a strut and a row of guide-vanes in tandem configuration at high subsonic Mach numbers in the Carleton University high-speed wind-tunnel. The structural performance of the design was evaluated through finite-element analysis and manufactured using a combination of conventional subtractive methods and additive methods.

Acknowledgments

I would like to acknowledge my thesis supervisor, Dr. Metin I. Yaras for providing me this opportunity to better myself and for his patience and dedicated mentorship throughout this journey. I also wish to thank Pratt and Whitney Canada as well as the Natural Sciences and Engineering Research Council (NSERC) for their financial support. My sincerest appreciation goes out to the technical and support staff of the university: Alex Proctor, Neil McFadyen, Kevin Sangster, and Stephan Biljan whose expertise were relied on countless times. Lastly but most certainly not least, I wish to thank my colleagues, Andrew Copping, Chanon Pretorius, Riley Simpson, Shuhao Wu, Ted Gan, and Utku Caylan, who's collaboration and friendship made this journey worthwhile.

Table of Contents

List of Tables

List of Figures

Nomenclature

a	speed of sound (m/s)
$[A]$	coefficient matrix (Eq. 3.17)
$[b]$	source term vector (Eq. 3.17)
c	chord length (m)
c_P	specific heat at constant pressure (J/kg K) (Eq. 2.1)
c_x	axial chord length (m)
c_{s_x}	strut axial chord length (m)
c_V	specific heat at constant volume (J/kg K)
c_v	guide-vane chord length (m) (Eq. 4.2)
c_{v_x}	guide-vane axial chord length (m)
c_{v_t}	guide-vane tangential chord length (m)
C_1	BSL Reynolds-stress modeling constant = 1.8
C_2	BSL Reynolds-stress modeling constant = 0.52
C_f	skin friction coefficient (Eq. 4.1)
C_P	static pressure coefficient (Eq. 2.4)
C_{P_o}	total pressure loss coefficient (Eq. 4.3)
$\widetilde{C}_{P_o}$	mass-averaged total pressure loss coefficient (Eq. 2.3)
C_t	tangential force coefficient (Eq. 4.2)
C_{ω_s}	vorticity coefficient (Eq. 2.5)
$CD_{k\omega}$	BSL Reynolds-stress model limiting constant (Eq. 3.7)

d	hatch spacing (mm) (Eq. K.1);
	cross-sectional length of an additive manufactured layer (mm)
D^{μ}_{ij}	Reynolds-stress viscous diffusion tensor (Eq. 3.12)
D^{τ}_{ij}	Reynolds-stress turbulent diffusion tensor (Eq. 3.13)
e_a	approximate relative error (Eq. F.6)
e_{ext}	extrapolated error (Eq. F.7)
F_1	turbulence model blending function (Eq. 3.6)
F_t	tangential (circumferential) force component (N) (Eq. 4.2)
F_{total}	total vane loading (N), $F_{total} = \sqrt{F_x^2 + F_t^2}$
F_x	axial force component (N)
h	enthalpy (kJ/kg); representative grid-node spacing (m) (Eq. F.1)
h_o	stagnation enthalpy (kJ/kg)
h_{o_1}	stagnation enthalpy (kJ/kg) at the entrance state
h_{o_2}	stagnation enthalpy (kJ/kg) at the exit state for the actual process
h_1	ITD inlet annulus height (m) $= R_{casing} - R_{hub}$ (Fig. 1.1)
h_2	enthalpy (kJ/kg) at the exit state for the actual process
h_{2s}	enthalpy (kJ/kg) at the exit state for the isentropic process
h_s	strut span length (m)
h_v	guide-vane span length (m) (Eq. 4.2)
H	shape factor, ($H = \delta^*/\theta$)
i	incidence angle (deg.)
GCI	grid convergence index (Eq. F.8)
k	turbulence kinetic energy (m^2/s^2) (Eq. 3.3)
k^+	normalized sand-grain roughness height, $k^+ = k/\delta_\nu$
k_s	sand-grain roughness height (m)
l_t	turbulence length scale (m) (Fig. 4.23);

L	ITD axial length (m) (Fig. 1.1);
L_{fp}	flat-plate length (m) (Section 4.4.1);
L_{sp}	splitter-plate length (m) (Fig. 4.18);
M	Mach number $= u/a$
M_S	shock Mach number (Eq. J.2)
N	total grid-node count (Eq. F.1)
N_b	number of guide-vanes on hub (Table 4.1 and Fig. 4.1)
N_{wake}	grid-node count in the wake along the direction of maximum velocity gradient (Fig. E.1)
o	throat width (m) (Table 4.1 and Fig. 4.1)
p	time-averaged static pressure (Pa) (Eq. 3.2); apparent grid-cell order (Eq. F.2)
P	static pressure (Pa)
P_{ij}	Reynolds-stress production tensor (Eq. 3.10)
P_k	rate of production of turbulence kinetic energy (Eq. 3.5)
P_L	laser power (W) (Eq. K.1)
P_o	stagnation pressure (Pa)
r	radial spatial coordinate (m); velocity ratio, $r = u_2/u_1$ (Eq. 2.12)
R	ideal gas constant (J/kg K) (Eq. 2.1)
R_{casing}	casing radius (m)
R_a	average roughness height (m)
R_{hub}	hub radius (m)
R_{LE}	leading edge radius (m) (Table 4.1 and Fig. 4.1)
R_{TE}	trailing edge radius (m) (Table 4.1 and Fig. 4.1)
R_q	rms roughness height (m)
R_z	average peak-to-valley roughness height (m)

Re	Reynolds number $= \frac{\rho U L}{\mu}$
Re_{c_x}	Reynolds number based on axial chord length $= \frac{\rho U c_x}{\mu}$
Re_{h_1}	Reynolds number based on ITD inlet annulus height $= \frac{\rho U h_1}{\mu}$
$Re_{L_{fp}}$	Reynolds number based on flat-plate length $= \frac{\rho U L_{fp}}{\mu}$
$Re_{L_{sp}}$	Reynolds number based on splitter-plate length $= \frac{\rho U L_{sp}}{\mu}$
Re_θ	Reynolds number based on momentum thickness $= \frac{\rho U \theta}{\mu}$
$Re_{\theta_{ext}}$	extrapolated Reynolds number based on momentum thickness (Eq. F.5)
s	density ratio $= \rho_2/\rho_1$ (Eq. 2.13); guide-vane pitch (m)
S	entropy (J/kg) (Eq. 2.1)
S_{ij}	local strain rate tensor (Eq. 3.15)
t	tangential spatial coordinate (m); time (s); layer thickness (mm)
t_{sp}	splitter-plate thickness (m)
T	static temperature (K)
T_o	stagnation temperature (K)
Tu	turbulence intensity (%)
u	local velocity (m/s)
u^+	normalized velocity, $u^+ = u/u_\tau$
u^*	velocity parameter (Eq. 2.6)
u'	velocity fluctuation (m/s) (Eq. 3.2)
u_1	high-speed freestream velocity (m/s) (Eq. 2.6)
u_2	low-speed freestream velocity (m/s) (Eq. 2.6)
u_{min}	minimum velocity in guide-vane wake (m/s) (Appendix E)
U_{ref}	reference velocity (m/s)
U_x	x-component of velocity (m/s)
U_y	y-component of velocity (m/s)
U_z	z-component of velocity (m/s)

u_τ	local friction velocity (m/s), $u_\tau = \sqrt{\tau_w/\rho}$
VEM	volumetric energy density (J/mm^3)($Eq.K.1$)
V_s	scan speed (mm/s) (Eq. K.1)
x	streamwise spatial coordinate (m)
x_o	axial location of mixing-layer origin (Eq. 2.7)
x_{TE}	axial location downstream of guide-vane trailing edge (Appendix E)
y	wall-normal spatial coordinate (m)
y^+	normalized wall-normal distance, $y^+ = y/\delta_\nu$
y_1	minimum pitchwise spatial boundary (m)
y_2	maximum pitchwise spatial coordinate (m)
y^+_{n1}	normalized distance for the first grid-node off the wall (Section 4.1.3)
y_o	transverse location of centre of mixing-layer origin (m) (Eq. 2.7)
z	spanwise spatial coordinate (m)

Greek Symbols

α_1	$k-\omega$ modeling constant (Table 3.1)
α_2	$k-\epsilon$ modeling constant (Table 3.1)
α_{k1}	$k-\omega$ modeling constant (Table 3.1)
α_{k2}	$k-\epsilon$ modeling constant (Table 3.1)
$\alpha_{\omega 1}$	$k-\omega$ modeling constant (Table 3.1)
$\alpha_{\omega 2}$	$k-\epsilon$ modeling constant (Table 3.1)
β'	modelling constant = 0.09
β_1	$k-\omega$ modelling constant (Table 3.1)
β_2	$k-\epsilon$ modelling constant (Table 3.1)
β'_{in}	inlet metal angle (deg.) (Table 4.1 and Fig. 4.1)
β'_{out}	exit metal angle (deg.) (Table 4.1 and Fig. 4.1)
δ^*	boundary layer displacement thickness (m) $= \int_{y_1}^{y_2}(1-\frac{u}{U_{ref}})dy$

δ_{99}	boundary layer thickness based on 99% local freestream velocity (m)
δ_{ij}	Kronecker delta (Eq. 3.11)
δ_m	mixing-layer thickness (m) (Eq. 2.11)
δ_ν	viscous length scale, $\delta_\nu = \nu/u_\tau$
ΔV	grid-cell volume (m^3)
Δx	streamwise grid-node spacing (m)
Δx^+	normalized streamwise grid-node spacing, $\Delta x^+ = \Delta x/\delta_\nu$
Δy	wall-normal grid-node spacing (m)
Δy^+	normalized wall-normal grid-node spacing, $\Delta y^+ = \Delta y/\delta_\nu$
ϵ	turbulence dissipation rate (m^2/s^3)
ϵ_{ij}	Reynolds-stress dissipation tensor (Eq. 3.11)
ϵ_{in}	leading-edge inlet half-wedge angle (deg.) (Table 4.1 and Fig. 4.1)
ϵ_{out}	trailing-edge exit half-wedge angle (deg.)
γ	turbulence intermittency; specific heat ratio, $\gamma = (c_P/c_V)$
λ_θ	Thwaites pressure gradient parameter (Fig. 2.3)
η	shear layer similarity parameter (Eq. 2.7)
θ	momentum thickness (m) $= \int_{y_1}^{y_2} \frac{u}{U_{ref}}(1 - \frac{u}{U_{ref}})dy$
θ_p	angle of guide-vane pressure-surface normal (deg.)
θ_s	angle of guide-vane suction-surface normal (deg.)
θ_u	unguided turning angle (deg.) (Table 4.1 and Fig. 4.1)
μ	dynamic viscosity (Pa s); friction coefficient
μ_t	turbulence eddy viscosity (kg/m s)
ν	kinematic viscosity (m^2/s)
ν_t	turbulence kinematic viscosity (m^2/s) (Eq. 3.4)
ξ	primary loss coefficient $= 1 - \frac{h_{o_2} - h_2}{h_{o_1} - h_{2s}}$ (Fig. 2.5)
ρ	air density (kg/m^3)

σ	spread-rate parameter for dual-stream mixing-layer (Eq. 2.12)
σ_a	stress amplitude (MPa)
$\sigma_{min/max}$	stress ratio $= \sigma_{min}/\sigma_{max}$
σ_{max}	maximum stress (MPa)
σ_{min}	minimum stress (MPa)
σ_o	spread-rate parameter for single-stream mixing-layer (Eq. 2.12)
τ_w	local wall shear stress (N/m^2)
ψ	general scalar variable (Eq. 3.8)
ω	specific turbulence dissipation rate (s^{-1}) (Eq. 3.3)
ω_s	streamwise component of vorticity (s^{-1})
ϕ	ITD mean rise angle (deg.) (Fig. 1.1); dependant vector (Eq. 3.17)
Φ_{ij}	Reynolds-stress pressure-strain rate tensor (Eq. 3.14)

Subscripts

adm	admissable
atm	atmospheric
i, j, k	indices for the x, y and z coordinate directions, respectively
min	minimum
max	maximum
mix	mixed
p	pressure surface
ref	reference
s	suction surface
x	vector component in x-direction
y	vector component in y-direction
z	vector component in z-direction

Abbreviations

AM	additive manufacturing
AR	ITD outlet-to-inlet area ratio
BSL	Baseline Reynolds-stress
CFD	computational fluid dynamics
DED	direct energy deposition
$DMLS$	direct laser metal sintering
DNS	direct numerical simulation
EBM	electron beam melting
FEA	finite element analysis
HIP	hot isostatic pressing
HPC	high-pressure compressor
HPT	high-pressure turbine
ICD	inter-compressor duct
ILU	incomplete lower-upper
ITD	inter-turbine duct
LRR	Launder, Reece, Rodi
LPC	low-pressure compressor
LPT	low-pressure turbine
NRC	National Research Council Canada
PBF	powder bed fusion
$RANS$	Reynolds-averaged Navier-Stokes
SSG	Speziale, Sakar, Gatski
VG	vane geometry

Chapter 1

Introduction

The inter-turbine duct (ITD) located in a typical turbofan aeroengine, as shown in Figure 1.1, is the annular, S-shaped duct that provides pressure recovery for the gas flow between the high-pressure (HPT) and low-pressure turbine (LPT) sections. This is converse to the inter-compressor duct (ICD) where the flow is guided in the presence of a favourable pressure gradient between the low-pressure (LPC) and high-pressure (HPC) compressor sections. Typically, there are 6 to 12 circumferentially spaced stationary struts located in the ITD that are responsible for transferring bearing loads from the main shaft to the outer casing in addition to housing service lines (Zhang et al., 2011). The typical bluff-body shape of the struts produce wakes that interact with the downstream low-pressure guide-vanes, potentially resulting in high aerodynamic losses. Due to the added complexity of diffusing streamwise flow and endwall streamwise curvature, the complete aerodynamics of the strut and guide-vane interaction in the ITD is not fully understood. Furthermore, the demand for lighter and more efficient gas turbine engines has pushed towards more aggressive ITD designs, with increasing outlet-to-inlet area ratio (AR), mean rise angle (ϕ) and decreasing length-to-inlet annulus height ratio (L/h_1) (Zhang et al., 2011). Therefore, an understanding of the flow physics

is crucial in maintaining low aerodynamic losses. A layered approach wherein the aerodynamic characteristics of individual geometric features are first studied in isolation and then in combinations of increasing complexity has proven to be an effective strategy. This strategy was adopted in the present study, which focused largely on the total pressure loss and momentum deficit within the wakes of the strut and guide-vanes. The study is based on complementary use of wind-tunnel experiments and numerical solutions of the governing Navier-Stokes equations in Reynolds-averaged form.

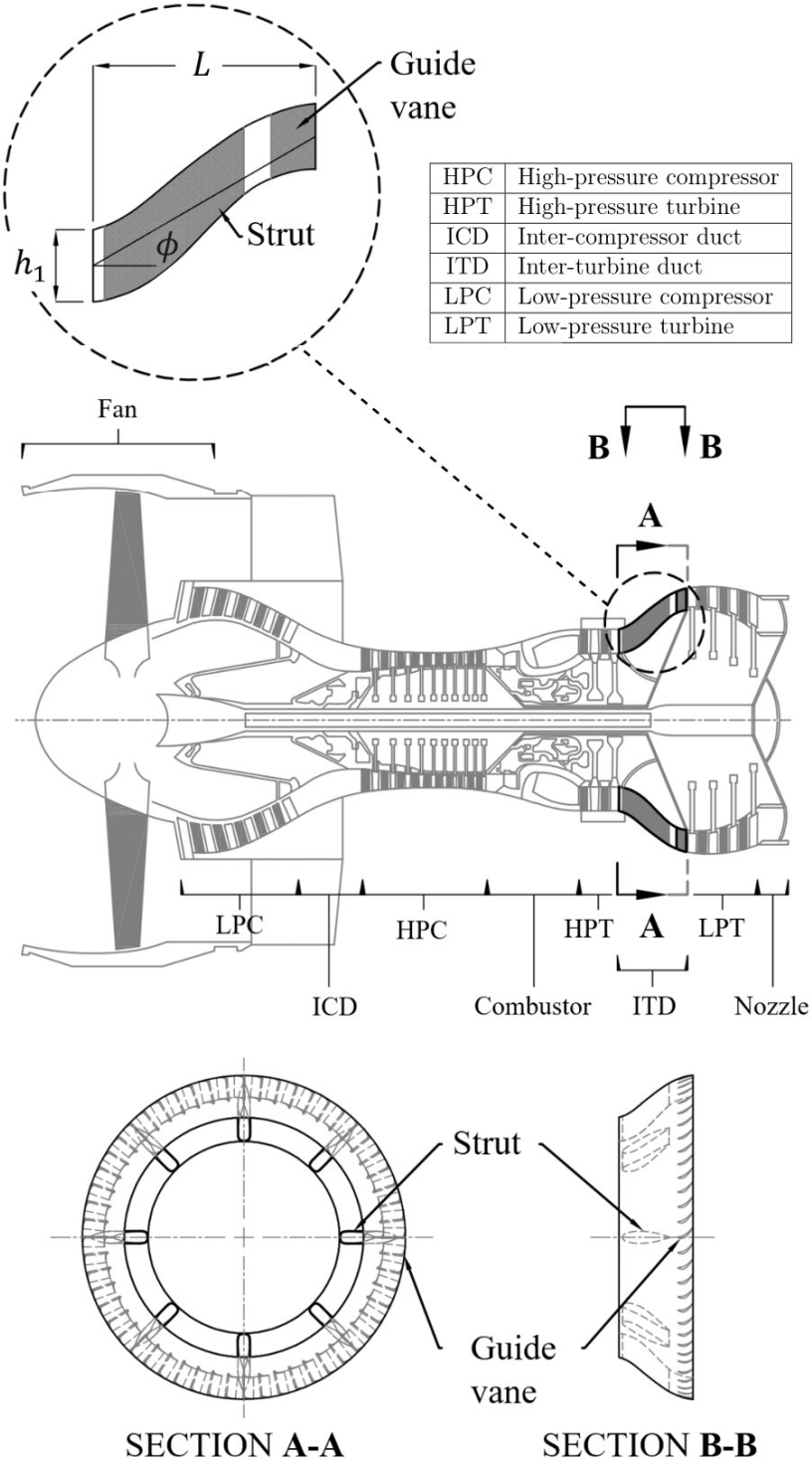

Figure 1.1: Typical ITD region in a turbofan gas-turbine engine

Chapter 2

Literature Review

This chapter provides a brief summary of the aerodynamic loss mechanisms in axial turbine rotors and begins with an explanation of how these losses are quantified. This is followed by a description of the typical inflow conditions at the ITD and the prevailing loss mechanisms within the ITD and midspan region of the strut and guide-vanes. The chapter concludes with a description of planar turbulent free-shear layers which serves to contextualize the viscous mixing that occurs between the strut and guide-vane wakes.

2.1 Aerodynamic Loss Generation Mechanisms in Axial Turbine Rotors

Aerodynamic losses are characterized by flow features that produce viscous mixing that result in the production of entropy, S, and a reduction in turbine efficiency (Denton, 1993). For an ideal gas, the change in entropy can be expressed as a function of temperature, T, and pressure, P, using:

$$dS = c_P \frac{dT}{T} - R\frac{dP}{P} \tag{2.1}$$

where c_P is the specific heat at constant pressure and R is the ideal gas constant. For an arbitrary finite process between two states where c_P is assumed to be constant, Eq. 2.1 can written as:

$$\Delta S = c_P \ln\left(\frac{T_2}{T_1}\right) - R \ln\left(\frac{P_2}{P_1}\right) \tag{2.2}$$

Eq. 2.1 and 2.2 are applicable to static or stagnation properties. In the case of a rotating turbine blade row where the stagnation quantities are defined relative to the blade frame of reference, the total temperature, T_o, is constant under an adiabatic process and the entropy rise is only a function of the total pressure drop, ΔP_o, which can be readily measured. For this reason, loss coefficients in turbomachine practise are typically defined using total pressure, P_o. Other loss coefficients based on enthalpy, h, have been defined by Kacker and Okapuu (1982), Mee et al. (1992) and Denton (1993) amongst others. The aerodynamic losses for the present study will be expressed as a mass-averaged total pressure loss coefficient, $\widetilde{C}_{P_{o,2}}$, given by:

$$\widetilde{C}_{P_{o,2}} = \frac{\widetilde{P}_{o,1} - \widetilde{P}_{o,2}}{P_{o,1} - P_1} \tag{2.3}$$

where $\widetilde{P}_{o,1}$ and $\widetilde{P}_{o,2}$ is the mass-averaged total pressure at the inlet and exit plane, respectively, of a chosen control volume and P_{o1} and P_1 is the total pressure and static pressure, respectively, at a specific reference point located in a region of undisturbed flow at the control volume inlet plane.

Based on the definition of aerodynamic loss expressed in Eq. 2.3, the following paragraphs provide a brief summary of the aerodynamic loss-generation mechanisms in an axial turbine rotor which, as shown in Figure 2.1, are typically divided into secondary, profile, and tip-leakage losses.

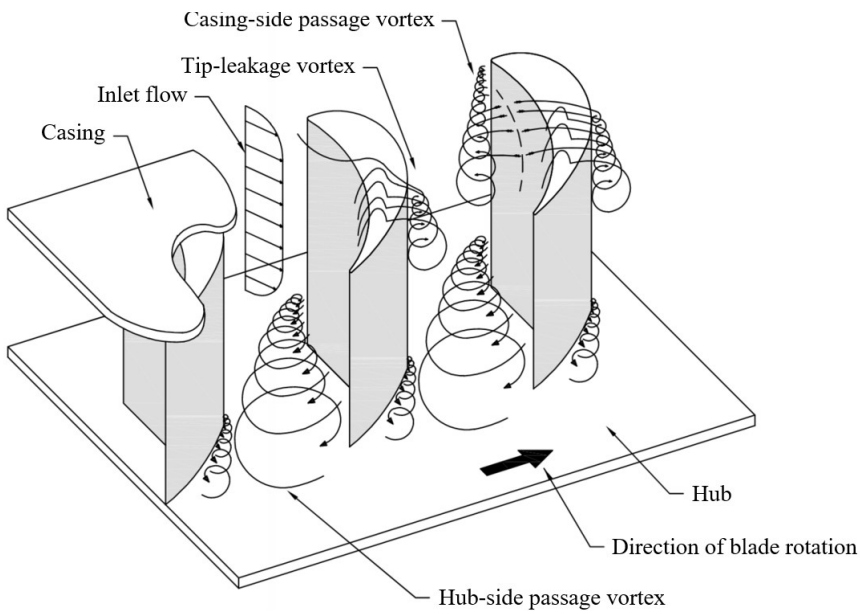

Figure 2.1: Vortical flow structures in an axial turbine rotor (adapted from Kibsey, 2015)

Secondary losses are associated with the endwall (casing and hub) boundary layer and are characterized by the presence of various vortical structures that form due to the interaction of the endwall boundary layers with the blades (Denton, 1993). Profile losses are associated with the boundary layers on the blade surfaces and the wakes that form downstream of the blade trailing edge. Tip-leakage losses occur due to the gap that exists between the unshrouded rotor blade tips and the casing. Fluid flows or "leaks" through this gap from the pressure side to the suction side of the blade, and rolls into a tip-leakage vortex.

The present study focuses on the aerodynamics of the strut and guide-vane interaction in the ITD. In an ITD, the primary aerodynamic loss mechanisms can largely be broken down into secondary and profile losses, where the former are associated with the ITD endwall and cross-stream flows, and the latter are associated with the strut(s) and LPT guide-vanes. These loss mechanisms are strongly influenced by the periodic unsteady inflow conditions of the ITD caused by the HPT stator and rotor blade rows that produce wakes, secondary flows, tip-leakage flows and trailing edge shocks (Gottlich, 2011). The next section provides a brief review of the literature pertaining to the inflow conditions of a typical ITD. This is followed by a discussion of secondary and profile losses in the ITD.

2.1.1 Inflow Conditions of the ITD

Detailed information about the inflow conditions for gas-turbine ITDs is not widely available as the design of these engines is proprietary and confidential. Walsh and Fletcher (2004) identify a typical ITD inflow Mach number range of 0.3 to 0.5 for turbofan engines. Modern gas-turbine engines now possess a notably higher Mach number range of 0.6 to 0.9 (Yaras, 2022). Generally, Mach and Reynolds numbers used to study the flow in an ITD are based on experimental data found in literature. Table 2.1 provides a list of inflow Mach numbers, M, and Reynolds numbers, Re_{h_1}, used in ITD wind-tunnel experiments. The subscript h_1 denotes the characteristic length scale defined by the ITD inlet annulus height.

Table 2.1: Summary of experimental ITD inflow conditions in the published literature

Inflow Parameters		**Area Ratio**	**Reference**
$\mathrm{Re}_{h_1}(\times 10^5)$	M		
3.9	<0.3	1.5	Dominy and Kirkham (1996)
3.2	0.2	1.5	Dominy et al. (1998)
–	0.6	1.5	Gottlich et al. (2007)
1.5	<0.3	1.27	Hu et al. (2011)
–	0.6	1.5	Marn et al. (2009)
1.55*	0.98	–	Miller et al. (2004)
3.9	<0.3	1.5	Norris et al. (1999)
2.0	<0.3	1.275	Zhang et al. (2013)

* = Re based on HPT axial chord length, c_x

– = Not listed

2.1.2 Secondary Losses in the ITD

The secondary losses in the ITD refer to the losses concentrated in the casing and hub boundary layers and the resultant cross-stream migration of this boundary-layer fluid under the influence of cross-stream pressure gradients. The nature of these losses is heavily dependant on the inflow conditions produced by the upstream HPT stage. The majority of wind-tunnel studies have used stationary guide-vanes to simulate HPT blade wakes with and without swirl at the exit of the HPT. The following paragraphs briefly summarize the characteristic flow features in the ITD in the absence of struts or guide-vanes based on the experimental work of Zhang et al. (2010). The results

presented are representative of a typical gas-turbine ITD. These flow features will vary for different inflow conditions and ITD geometries that have different rise angles and varying streamwise distributions of flow areas. As shown in the surface pressure plot in Figure 2.2, the flow along the casing and hub experiences different regions of favourable, adverse or almost zero streamwise pressure gradient which are affected by the streamwise variation in flow area, local streamwise curvature and the extent of flow nonuniformity across the ITD flow area. The surface pressure is expressed in terms of a static pressure coefficient, C_P, given by:

$$C_P = \frac{P - P_1}{P_{o,1} - P_1} \tag{2.4}$$

where the subscript 1 denotes the static pressure at Plane 1 corresponding to the ITD inlet plane in Figure 2.2. As shown in Figure 2.2, the static pressure at the first bend is lower at the casing than at the hub while the opposite is true at the second bend. Along the hub, there exists an adverse pressure gradient at the first bend followed by a region of an almost zero pressure gradient and then a favourable gradient in the first portion of the second bend followed by an adverse pressure gradient. Conversely, the casing experiences a favourable pressure gradient at the first bend followed by an adverse pressure gradient throughout most of the ITD. The pressure differences between the casing and hub result in radial (cross-stream) pressure gradients, which create secondary flows that promote the formation of streamwise vortices that drive the redistribution of mass flow.

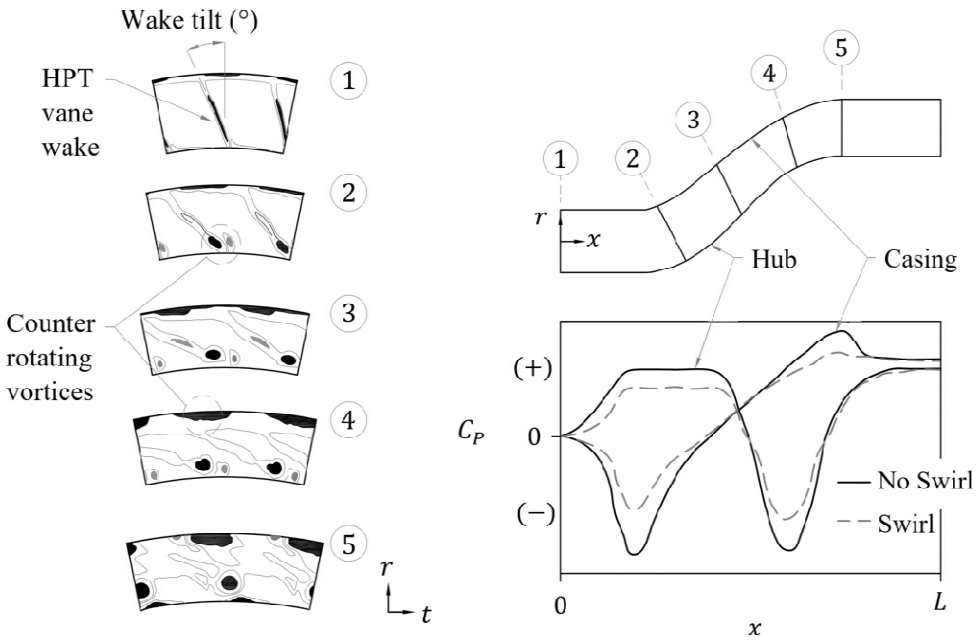

Figure 2.2: Streamwise vorticity at Plane 1 to Plane 5 of the ITD and static pressure distribution along the hub and casing

The contour plot in Figure 2.2 illustrates schematically the evolution of streamwise vorticity as defined in normalized form by the coefficient C_{ω_s} given by:

$$C_{\omega_s} = \frac{\omega_s h_1}{U_1} \tag{2.5}$$

where ω_s, is the streamwise component of the vorticity vector, U_1 is the freestream velocity at Plane 1 and h_1 is the annulus height at Plane 1. Darker regions of the contour plot in Figure 2.2 indicate a higher magnitude of C_{ω_s}. At Plane 1, the vorticity is concentrated in the HPT wake region. Further downstream at Plane 2, a strong radial pressure gradient at the first bend produces two counter-rotating streamwise vortices near the hub, while the HPT

wakes diffuse and tilt at a magnitude proportional to the radial swirl variation dictated by the HPT blade twist and radial flow equilibrium in the context of prevailing radial variations in axial velocity (Brookfield et al., 1996). At Plane 3, the growing hub counter-rotating vortices at the hub become stronger and migrate radially towards the casing where an adverse streamwise pressure gradient produces boundary layer separation. At Plane 4, the wake continues to tilt and dissipate, while the radial pressure gradient reverses, causing the flow and counter-rotating vortices to be driven towards the hub. The separated boundary layer at the casing promotes the formation of counter-rotating streamwise vortices. At Plane 5, the wake has decayed further and the boundary layer at the hub begins to separate while the counter-rotating vortices at the hub and casing are strongly pronounced.

The presence of swirl at the ITD inlet introduces a tangential (t) velocity component which effectively creates a longer flow path through the ITD and a reduction in local curvature that leads to a lower adverse streamwise pressure gradient when compared to the case without swirl (Gottlich, 2013). Due to the conservation of angular momentum, the tangential component of flow is largely independant of the axial velocity which varies along the length of the ITD (Lohmann et al., 1979). The exaggerated effect of swirl on the casing and hub surface pressures in Figure 2.2 illustrate the reduction in radial pressure gradient along the length of the ITD. Kumart et al. (1980) observed that an increase in swirl angle reduced the likelihood of flow separation at the casing, particular near the second bend where the aerodynamic losses increase more rapidly than at the first bend. This is supported by the study of Zhang et al. (2011), however, they also determined that a strong radial swirl gradient produced higher losses overall due to the presence of stronger counter-rotating vortices at the hub.

2.1.3 Profile Losses

The profile losses are associated with the blade surface boundary layers and the free-shear layer downstream of the trailing edge (Denton, 1993). Experimental studies of profile loss are often done using stationary turbine cascades and are concentrated in the blade midspan region where the flow can be considered two-dimensional. The standard convention has been to quantify profile losses in the absence of secondary losses and tip leakage losses when applicable and then merely superimposing the loss mechanisms to obtain the total loss. This approach has been remarkably successful, despite neglecting the mutual interactions of the loss mechanisms. The state of the boundary layer, i.e. laminar or turbulent, and the location and length of the transition region strongly influence the profile loss. Turbulent boundary layers generate higher shear forces at the blade surface, while they help to delay the onset of possible separation and thus mixing losses, that might otherwise occur in a laminar boundary layer. The laminar-to-turbulent boundary layer transition process generally occurs via three modes: natural transition, bypass transition and separation-induced transition (Roberts, 2005; Mayle, 1991). Due to the periodic unsteady flow processes that exist in turbomachinery, transition may occur by different modes at different locations on the same surface at the same time (Mayle, 1991). Natural transition of a boundary layer occurs in low-disturbance environments and is characterized by the presence of viscous instabilities (Ancrum, 2016). At a certain critical value of Reynolds number, the laminar boundary layer experiences instabilities in the form of two dimensional Tollmien-Schlichting (T-S) waves that amplify at an initially linear logarithmic scale to become three dimensional in the form of Λ-shaped and subsequently hairpin-shaped vortices (Schlichting, 1979). This creates turbu-

lent spots in the layer which grow and convect downstream before coalescing into a fully-developed boundary layer (Mayle, 1991). Although this mechanism has been studied extensively, it is not particularly relevant to turbomachinery, where the existence of high freestream turbulence, streamwise pressure gradients, surface roughness, streamline curvature and cooling jet flows promote accelerated transition, known as bypass transition. Bypass transition is the most common mode of transition in turbomachinery and is characterized by the absence of the linear growth and secondary instability phases of natural transition (Mayle, 1991). Instead, turbulent spots are produced directly in the boundary layer and their characteristics are independant of the source of the initial disturbance (Schubauer and Klebanoff, 1956).

Emmons(1951) was the first to provide a statistical theory for the turbulent spot production using the concept of intermittency, γ which is defined by a value of zero and unity for a laminar and fully-turbulent boundary layer, respectively. Values between zero and unity represent a transition region, where the flow is partially laminar and partially turbulent. For the higher freestream turbulence intensities ($> 2\%$) present in gas turbine engines, the onset of transition is dictated largely by the freestream turbulence intensity and to a lesser extent by the pressure gradient (Abu-Ghannam and Shaw, 1991), as shown in Figure 2.3.

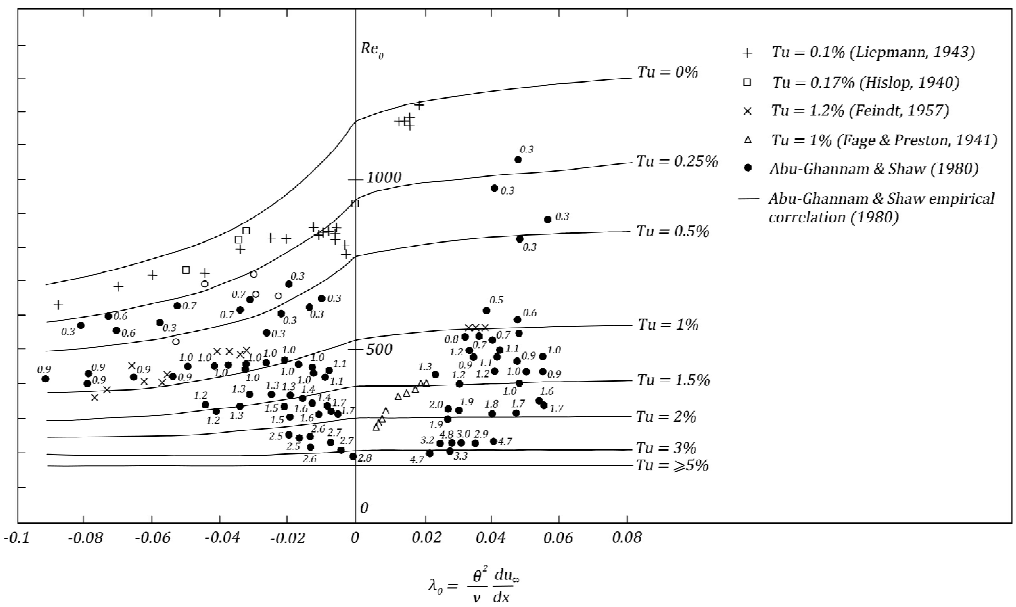

Figure 2.3: Influence of freestream turbulence level on the Reynolds number at transition onset (Abu-Ghannam and Shaw, 1980)

Figure 2.4 schematically relates the state of the boundary layer and the transition location to the total profile loss for an airfoil. As shown, the location of the transition point on the blade surface tends to move farther upstream towards the leading edge with increasing Reynolds number. For very high Reynolds numbers (a), the transition point is located near the leading edge such that the turbulent boundary layer covers most of the blade surface. As the Reynolds number decreases (b), the transition point moves farther downstream and the profile losses decrease due to the larger portion of laminar boundary layer with its lower wall-shear stress.

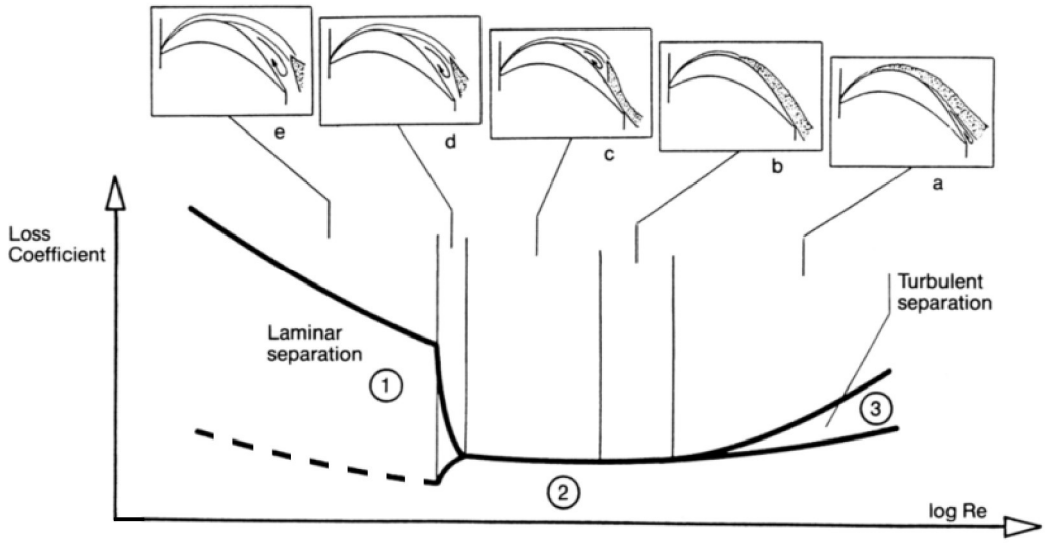

Figure 2.4: Effect of Reynolds number on profile losses (Hourmouziadis, 1989)

This continues until the losses reach a minimum (c), at which point a further decrease in Reynolds number causes the laminar boundary layer to separate from the blade surface where the free-shear layer transitions to turbulence due to its highly inflectional hence inviscid unstable velocity profile and then reattaches with the aid of the increased wall-normal momentum exchange in the turbulent state to form a separation bubble. A further decrease in the Reynolds number (d) causes the separation bubble to grow until it can no longer reattach resulting in a "stalled" blade/vane. In this scenario, the total profile loss is dominated by viscous mixing. Separation bubble lengths are typically classified as being either "long" or "short" (Gaster, 1969). Long separation bubbles are characterised by the presence of multiple re-circulation zones that affect the overall pressure distribution over the blade surface. Short bubbles, however, produce only a local effect on the pressure distribution, and possess a single dominant recirculating region within the bubble. Alternatively,

separation bubbles can be avoided and the laminar boundary layer can remain attached along the entire blade surface as indicated by the dashed line on Figure 2.4. This is possible with strategic chordwise distribution of aerodynamic loading to produce moderate adverse pressure gradients. As shown in Figure 2.5, at low subsonic Mach numbers the profile loss is largely concentrated in the boundary layer along the suction surface where the local wall-normal velocity gradient is highest. A smaller portion of loss is attributed to viscous mixing downstream of the trailing edge which relates to the velocity deficit in the wake (Denton, 1993). As shown in Figure 2.5, as the exit flow approaches $M_2 = 1.0$, regions of supersonic flow develop along the suction surface that produce shocks, which affect the pressure distribution of the airfoil, resulting in higher losses (Kibsey, 2015). The present study of the aerodynamics of the strut and guide-vane interaction focuses only on incompressible flow conditions as the flow Mach number in regions of the ITD where struts and guide-vanes are typically positioned is not high enough to prompt significant compressibility effects. The topic of viscous mixing is explored in the next section in the context of a planar turbulent free-shear layer.

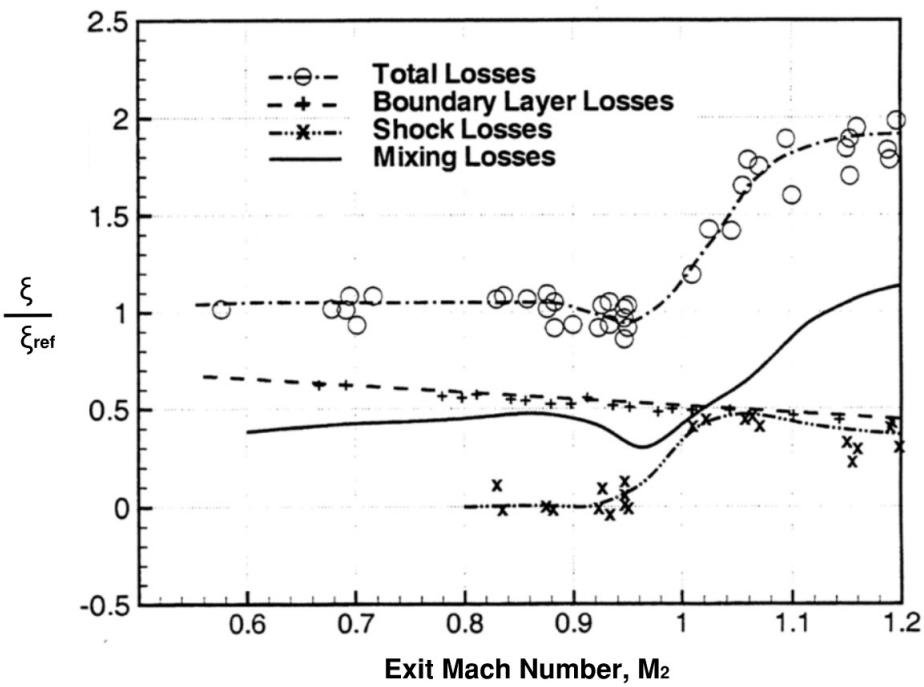

Figure 2.5: Kinetic energy loss coefficient at the midspan of a transonic turbine cascade (Mee et al., 1992)

2.2 Turbulent Planar Free-Shear Layer

The present study of profile losses involves an analysis of the interaction of the wake of an upstream strut with a row of guide-vanes. To provide context for the interpretation of this interaction, the fundamental dynamics of a planar turbulent free-shear layer is reviewed in this section. Figure 2.6 identifies the terminology pertaining to a planar free-shear layer created downstream of a splitter-plate.

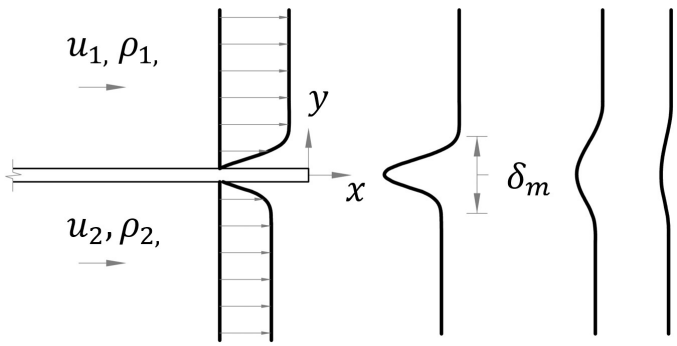

Figure 2.6: Planar mixing-layer

The planar turbulent free-shear layer represents one of the most fundamental free-shear layer flows and is often used as a benchmark to evaluate turbulence models (Yoder, 2005). This type of flow consists of two parallel streams of differing velocities at zero streamwise pressure gradient that are initially separated by a splitter-plate of small thickness and then allowed to come into contact. As shown in Figure 2.6, a shear layer develops between the high-speed and low-speed flows, the thickness, δ_m, of which increases with distance downstream of the splitter-plate trailing edge. The velocity profiles at axial locations far downstream of the splitter-plate are self-similar, i.e. they can be defined by a single profile when plotted in terms of specific similarity parameters. The turbulent solution of Gortler (1942) is the most widely used to define the velocity profile of an incompressible planar free-shear layer and is expressed in terms of a nondimensional velocity parameter, u^*, given by:

$$u^*(y) = \frac{u(y) - u_2}{u_1 - u_2} = \frac{1}{2}\left(1 + erf(\eta)\right) \tag{2.6}$$

where u is the local streamwise velocity. The subscripts 1 and 2 denote the high-speed and low-speed freestream velocities, respectively, on either side of

the splitter-plate. η is a nondimensional similarity parameter defined by:

$$\eta = \sigma \frac{y - y_o}{x - x_o} \tag{2.7}$$

where σ is the spread-rate parameter which is determined experimentally, x_o is the axial location of the virtual origin commonly defined at the splitter-plate trailing edge and, y_o is the transverse location of the center of the shear layer. Eq. 2.6 is plotted in Figure 2.7.

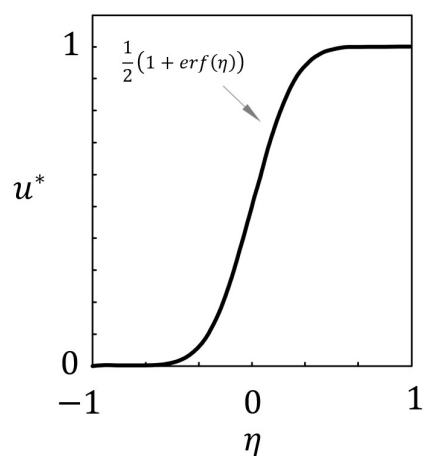

Figure 2.7: Error-function velocity profile representing the self-similar planar turbulent free-shear layer

2.2.1 Mixing-layer Thickness

Much like the boundary layer thickness, δ, there is no precise way to measure the mixing-layer thickness, δ_m. Several definitions exist including visual definitions based on photographs, however most definitions of the mixing-layer thickness use Gortler's error-function velocity profile given by Eq. 2.6 to calculate the transverse distance between two y-locations where the velocity

parameter, u^* is equal to prescribed values. Mehta (1991), Bell and Mehta (1990) and others have used the distance between $u^* = 0.1$ and $u^* = 0.9$ to define the mixing-layer thickness, and this is the definition that is used in the present study. Based on this definition, the mixing-layer thickness can be derived by combining Eq. 2.6 and Eq. 2.7 to yield:

$$\delta_m = (y_{0.9} - y_{0.1}) \tag{2.8}$$

$$\delta_m = (\eta_{0.9} - \eta_{0.1})\frac{(x - x_o)}{\sigma} \tag{2.9}$$

$$\delta_m = (0.906 - (-0.906))\frac{(x - x_o)}{\sigma} \tag{2.10}$$

$$\delta_m = 1.812\frac{x - x_o}{\sigma} \tag{2.11}$$

2.2.2 Spread-Rate Parameter

The spread-rate parameter, σ, is most commonly defined using the Abramovich-Sabin (1963) rule given by:

$$\frac{\sigma_0}{\sigma} = \frac{1 - r}{1 + r} \tag{2.12}$$

where $r = u_2/u_1$ is the freestream velocity ratio and σ_0 is the spread-rate parameter in which one stream is at rest ($u_2 = 0$). σ_0 is typically in the range of $10 < \sigma_0 < 12$. Based on a review of experimental data, Birch and Eggers (1972) propose a nominal value of $\sigma_o = 11$. When the density ratio, $s = \rho_2/\rho_1$,

between streams is not at unity, Brown and Roshko (1974) and Papamoschou and Roshko (1988) have rewritten Eq. 2.12 as:

$$\frac{\sigma_0}{\sigma} = \frac{(1-r)(1+\sqrt{s})}{2(1+r\sqrt{s})} \tag{2.13}$$

Based on an assumed value of $\sigma_o = 11$, and an incompressible flow condition where $s = 1$, Eq. 2.11 and Eq. 2.13 can be combined to yield the mixing-layer growth rate given by:

$$\frac{d\delta_m}{dx} = 0.165\frac{\sigma_o}{\sigma} \tag{2.14}$$

As shown in Figure 2.8, Eq. 2.14 is in good agreement with published experimental data.

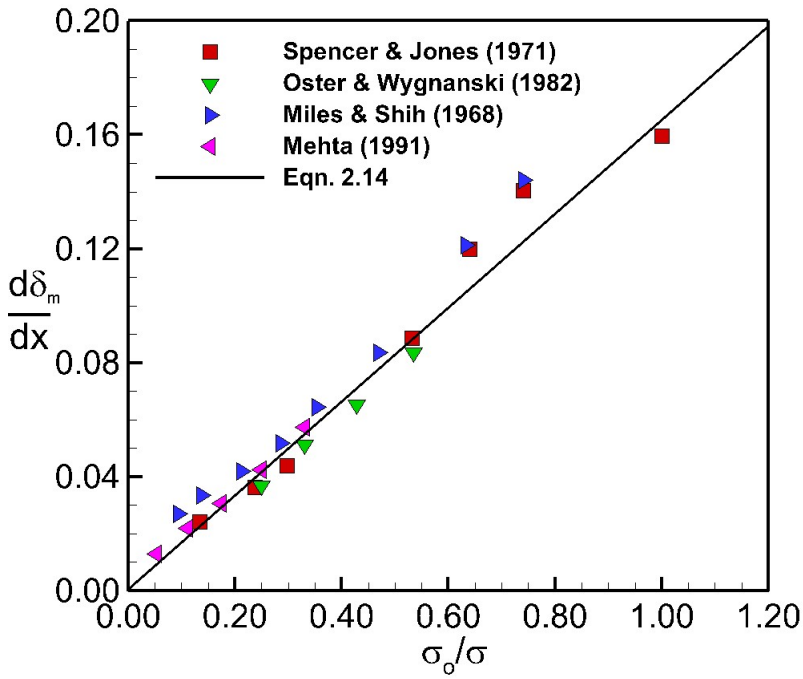

Figure 2.8: Incompressible mixing-layer growth rates for turbulent free-shear layers

Chapter 3

Computational Method

3.1 Governing Equations and Turbulence Modeling

Steady flow simulations were performed using ANSYS CFX, a commercial computational fluid dynamics (CFD) software. For the present study, the software solves the incompressible Reynolds-averaged Navier Stokes (RANS) equations given by:

$$\frac{\partial U_i}{\partial x_i} = 0 \tag{3.1}$$

$$\frac{\partial U_i}{\partial t} + \frac{\partial (U_i U_j + \overline{u_i' u_j'})}{\partial x_j} = -\frac{1}{\rho}\frac{\partial p}{\partial x_i} + \nu \frac{\partial}{\partial x_j}\left[\frac{\partial U_i}{\partial x_j} + \frac{\partial U_j}{\partial x_i}\right] \tag{3.2}$$

where U_i is the Reynolds-averaged-velocity in the x_i Cartesian coordinate direction, $u_i^{'}$ is the difference between the instantaneous and Reynolds-averaged values of U_i, ρ is the density, p is the Reynolds-averaged static pressure and ν is the molecular kinematic viscosity. The repeating index notation in any term denotes Einstein summation along indices 1, 2, 3 representing the Cartesian x, y, z directions, respectively. The presence of the time derivative in Eq. 3.2

is for efficient solution of the equations numerically, and does not conflict with the statement that steady flows were simulated. The term $\overline{u_i' u_j'}$ is referred to as Reynolds-stress because its diffusive effect on the Reynolds-averaged velocity field resembles the effect of viscous stresses. This term is non-zero unless u_i' and u_j' are uncorrelated, however coherence of the flow structures describing turbulence ensures u_i' and u_j' to be correlated. The overbar in the term $\overline{u_i' u_j'}$ denotes Reynolds averaging whereby time-averaging is performed over a period that is long relative to the time scale of turbulence but short in relation to non-turbulent flow unsteadiness. The Reynolds-stress tensor is quantified differently based on the turbulence model which are broadly classified into eddy viscosity models and Reynolds-stress models. Eddy viscosity models invoke Boussinesq's hypothesis which assumes that the Reynolds-stresses are proportional to the local strain rate, with the eddy viscosity, μ_t, serving as the scaling factor. Eddy viscosity models are further categorized into zero, one and two-equation models. Zero equation turbulence models compute the eddy viscosity using an algebraic expression. The name "zero-equation" refers to the model not making use of a differential equation to model the transport of the relevant turbulence parameters (ANSYS, 2006). One-equation turbulence models use one turbulence transport partial-differential equation, typically the governing turbulence kinetic energy, k, or the eddy viscosity. Two-equation turbulence models use two relevant turbulence transport partial differential equations, typically k to represent the time/velocity scale of turbulence and the turbulence dissipation rate, ϵ, or the specific turbulence dissipation rate, ω, to represent the length scale of turbulence. Reynolds-stress turbulence models, however, do not invoke Boussinesq's hypothesis. Instead, they involve separate partial differential equations for the transport of each of the components of the Reynolds-stress tensor plus a transport equation for the dissipation rate.

Algebraic Reynolds-stress models model the transport of the Reynolds stresses through algebraic rather than differential equations. The present study focuses on a differential Reynolds-stress model, of which there exist several variants including the Baseline (BSL); Launder, Reece, Rodi (LRR); and Speziale, Sarkar, Gatski (SSG) models (Launder et al., 1975; Speziale et al., 1991). The RANS-based BSL Reynolds-stress model was chosen for the present study specifically because it can accommodate low-Reynolds number flows in the near wall region without the use of scalable wall functions (ANSYS, 2006). Supplementing Eq. 3.1 and 3.2, the RANS-based BSL Reynolds-stress model uses seven partial differential transport equations: one for the specific turbulence dissipation rate, ω, and six equations corresponding to each of the six components of the Reynolds-stress tensor. The ω transport equation is given by:

$$\begin{aligned}\frac{\partial \omega}{\partial t} + \frac{\partial}{\partial x_k}(U_k\,\omega) = \alpha_3\,\frac{\omega}{k}P_k - \beta_3\,\omega^2 + \frac{\partial}{\partial x_k}\left[\left(\nu + \frac{\nu_t}{\sigma_{\omega 3}}\right)\frac{\partial \omega}{\partial x_k}\right] \\ +2(1-F_1)\frac{1}{\sigma_{\omega 2}\,\omega}\frac{\partial k}{\partial x_k}\frac{\partial \omega}{\partial x_k}\end{aligned} \tag{3.3}$$

where k is the turbulence kinetic energy and ν_t is the turbulence kinematic viscosity given by:

$$\nu_t = \frac{k}{\omega} \tag{3.4}$$

P_k is the rate of turbulence production given by:

$$P_k = \nu_t\left[\frac{\partial U_i}{\partial x_j} + \frac{\partial U_j}{\partial x_i}\right]\frac{\partial U_i}{\partial x_j} \tag{3.5}$$

and F_1 is a blending function given by:

$$F_1 = tanh\left(min\left[max\left(\frac{\sqrt{k}}{\beta'\,\omega\,x_2}, \frac{500\nu}{x_2^2\,\omega}\right), \frac{4\rho k}{CD_{k\omega}\,\sigma_{\omega 2}\,x_2^2}\right]\right)^4 \tag{3.6}$$

$$CD_{k\omega} = max\left[2\,\rho\,\frac{1}{\sigma_{\omega 2}\,\omega}\,\frac{\partial k}{\partial x_j}\,\frac{\partial \omega}{\partial x_j}, 10^{-10}\right] \tag{3.7}$$

where $\beta' = 0.09$ and $\sigma_{\omega 2} = 1.168$. The coefficients α_3, β_3 and $\sigma_{\omega 3}$ are calculated using:

$$\psi_3 = F_1\psi_1 + (1 - F_1)\psi_2 \tag{3.8}$$

where the subscripts 1 and 2 for the general scalar, ψ, denote the constants listed in Table 3.1 which correspond to the $k - \omega$ and $k - \epsilon$ two-equation turbulence models, respectively.

Table 3.1: Constants used in the BSL RANS model

$k - \omega$	$k - \epsilon$
$\alpha_1 = 0.553$	$\alpha_2 = 0.44$
$\beta_1 = 0.075$	$\beta_2 = 0.0828$
$\sigma_{k1} = 2$	$\sigma_{k2} = 1.0$
$\sigma_{\omega 1} = 2$	$\sigma_{\omega 2} = 1.168$

The $k-\omega$ constants were calibrated using free-shear flows (round/planar jets, mixing-layers), wall-bounded flows (channel and pipe flow) and backward-facing steps and separated flows (Wilcox, 1998). The $k-\epsilon$ constants were calibrated using free-shear flows including planar/round jets in stagnant surroundings, planar mixing-layers between two constant streams and planar/round wakes (Rodi, 1972).

The transport equation for the components of the Reynolds-stress tensor in the RANS-based BSL Reynolds-stress model is given by Eq. 3.9 in an inertial frame of reference and in the absence of body forces.

$$\frac{\partial \overline{u_i' u_j'}}{\partial t} + \frac{\partial}{\partial x_k}(U_k \overline{u_i' u_j'}) = P_{ij} + \epsilon_{ij} + D^{\mu}{}_{ij} + D^{\tau}{}_{ij} + \Phi_{ij} \tag{3.9}$$

where the left-hand-side terms represent the substantial (material) derivative of the Reynolds-stress. P_{ij} represents the Reynolds-stress production tensor due to velocity gradients transferring energy from the mean flow to the turbulence velocity fluctuations (Wilcox, 1998) and is given by:

$$P_{ij} = -\overline{u_i' u_k'}\,\frac{\partial U_j}{\partial x_k} - \overline{u_j' u_k'}\,\frac{\partial U_i}{\partial x_k} \tag{3.10}$$

ϵ_{ij} represents the Reynolds-stress dissipation tensor which is characterized by the transfer of turbulence kinetic energy of the smallest eddies to internal (thermal) energy by viscous action (Leschziner, 2015), and is given by:

$$\epsilon_{ij} = -\frac{2}{3}\,\beta'\,\omega\,k\,\delta_{ij} \tag{3.11}$$

where δ_{ij} is the Kronecker delta.

$D^{\mu}{}_{ij}$ represents the viscous diffusion tensor of the Reynolds-stresses due to molecular motion and is given by:

$$D^{\mu}{}_{ij} = \frac{\partial}{\partial x_k}\left[\nu\,\frac{\partial \overline{u_i' u_j'}}{\partial x_k}\right] \tag{3.12}$$

$D^{\tau}{}_{ij}$ represents the turbulent diffusion tensor of the Reynolds-stresses due to turbulent mixing and is given by:

$$D^{\tau}{}_{ij} = \frac{\partial}{\partial x_k}\left[\frac{\nu_t}{\sigma_{k3}}\frac{\partial \overline{u_i' u_j'}}{\partial x_k}\right] \tag{3.13}$$

where σ_{k3} is calculated using Eq. 3.8 and the constants listed in Table 3.1.

Φ_{ij} represents the tensor of pressure-strain-rate interaction which is responsible for forcing the normal Reynolds-stresses towards isotropy by distributing the turbulence kinetic energy between directions (Hanjalic and Launder, 2011). For the RANS-based BSL Reynolds-stress model, it is represented by a linear equation given by:

$$\begin{aligned}\Phi_{ij} = \beta'\,C_1\,\omega\Big(-\overline{u_i' u_j'} + \frac{2}{3}\,k\,\delta_{ij}\Big) - ((8+C_2)/11)\Big(P_{ij} - \frac{2}{3}\,0.5P_{kk}\,\delta_{ij}\Big) - \\ ((8C_2-2)/11)\Big(D_{ij} - \frac{2}{3}\,0.5P_{kk}\,\delta_{ij}\Big) - ((60C_2-4)/55)k\Big(S_{ij} - \frac{1}{3}S_{kk}\,\delta_{ij}\Big)\end{aligned} \tag{3.14}$$

where $C_1 = 1.8$ and $C_2 = 0.52$ and

$$S_{ij} = \frac{1}{2}\left(\frac{\partial U_i}{\partial x_j} + \frac{\partial U_j}{\partial x_i}\right) \tag{3.15}$$

$$D_{ij} = -\overline{u_i' u_k'} \frac{\partial U_k}{\partial x_j} - \overline{u_j' u_k'} \frac{\partial U_k}{\partial x_i} \tag{3.16}$$

where S_{ij} is the local strain rate tensor.

3.2 Discretization

The ANSYS CFX solution algorithm uses a modified form of the mass conversation equation given by Eq. 3.1 by expressing the velocity in terms of pressure via the momentum conversation equation given by Eq. 3.2, thereby yielding a flow field pressure distribution governed by Poisson's equation. ANSYS CFX uses a vertex centered finite volume approach to discretize the spatial domain into a collocated grid where the solutions to the governing equations given by Eq. 3.1, 3.2, 3.3 and 3.9 are stored at the grid nodes. To solve the flow field, control volumes are created around each node defined by the lines connecting the surrounding element face centroids (ANSYS, 2006). Coupling of the pressure field to the velocity field is accomplished using the Rhie and Chow (1983) scheme, in which the velocities at the integration points located on the faces of the control volume are represented as an average of the surrounding nodal values, and adjusted by the redistribution of pressure gradients at the faces of the finite volume. The non-linear convection term in the momentum equations are linearized using Picard iteration which involves successive approximations of the momentum components using the velocity from the current iteration and the mass flux from the previous iteration (Ferziger and Peric, 2002). The spatial derivatives of the flow properties stored at the nodes are spatially interpolated to the integration points in a manner equivalent to second-order centered differencing except for the flow properties in

the convection term in the momentum equations which use an interpolation process equivalent to a hybrid of first-order upwind and second-order centered differencing.

3.3 Solution Methodology

ANSYS CFX uses a multigrid-accelerated Incomplete Lower-Upper (ILU) factorization method (ANSYS, 2006) to iteratively solve the linearized system of discretized versions of the differential governing equations (Eq. 3.1, 3.2, 3.3 and 3.9) which can be expressed in general matrix form as:

$$[A][\phi] = [b] \tag{3.17}$$

where $[A]$ is the coefficient matrix of the linearized equations, ϕ is the solution vector and $[b]$ is the source-term vector. The iterative process consists of an initial approximation to ϕ, expressed as $[\phi^n]$, that is corrected over n iterations by a correction term, $[\phi^{'}]$, to yield a corrected solution, $[\phi^{n+1}]$, given by:

$$[\phi^{n+1}] = [\phi^n] + [\phi^{'}] \tag{3.18}$$

Substituting Eq. 3.17 into Eq. 3.18 yields:

$$[A][\phi^{'}] = [b] - [A][\phi^n] \tag{3.19}$$

As the solution to the system of equations converges, the value of $[\phi^{'}]$, also referred to as the residual, tends towards zero. The residuals are normal-

ized by reference parameters that are defined by ANSYS CFX as a function of the control volume and range of key variables in the domain that are not listed in the ANSYS documentation for proprietary reasons. The convergence of the solution is accelerated using a W-type Algebraic-Multigrid technique conventionally referred to as Additive Correction, which efficiently removes longer-wavelength errors in the domain by solving the equations on a series of successively coarser grids. This technique consists of a restriction operation in which a single solution sweep is performed at each grid level up to the coarsest grid, followed by a prolongation operation in which the coarse grid solution or a correction to the flow field variables is interpolated through the range of finer grids back on to the finest (original) grid. This restriction and prolongation process constitutes a single inner-loop iteration in which the coefficient matrix, $[A]$ is fixed. For each inner-loop iteration, there is an outer-loop iteration where $[A]$ is updated and the simulation is advanced forward in pseudo-time. For steady-state flows, this pseudo-time marching under-relaxes the solution process and promotes diagonal dominance of the $[A]$ matrix, with both of the effects promoting robustness of the iterative solution. For the present simulations, a spatially and temporally fixed pseudo-time step is defined for each domain as listed in Table 3.2 based on a conservative calculation done by the CFX solver as a function of the computational domain boundary conditions and geometry. The pseudo-time step size varies inversely with the number of outer loop iterations required to achieve convergence of the numerical solution such that a smaller step size provides more robustness at the expense of computational efficiency. For the present simulations the pseudo-time step in Table 3.2 does not vary between each outer loop.

Table 3.2: Psuedo-time step

Computational domain	Psuedo-time step (s)
Guide-vane row	8.66×10^{-4}
Single strut (diffusing/non-diffusing)	2.84×10^{-4}
Strut and a row of guide-vanes in tandem configuration	2.23×10^{-4}
Zero-pressure-gradient turbulent boundary layer	7.13×10^{-3}
Plane turbulent free-shear layer	5.31×10^{-3}

The solution for the present simulations is declared converged when the following criteria are met: (1) at least 100 outer iterations have passed, (2) the mass-averaged pressure loss between the domain inlet and outlet plane, calculated over an interval of 50 iterations, remains unchanged within a tolerance of 1×10^{-5} and (3) the root-mean-square of the residuals of the governing equations are reduced to less than 1×10^{-6}.

Chapter 4

Computational Models and Results

This chapter presents all of the computational models used in the current study beginning with a description of the guide-vane and strut airfoil geometries typical of those located in the gas-turbine ITD and the isolated performance of each in the presence of flow conditions found in the ITD. This is followed by a validation of the RANS-based BSL Reynolds-stress model for a strut and a row of guide-vanes in tandem configuration against low-speed wind-tunnel data and a further analysis of the RANS-based BSL Reynolds-stress model for two simpler flow scenarios: a zero-pressure-gradient turbulent boundary layer over a flat-plate and a planar turbulent free-shear layer. The numerical results for each is compared against published data obtained through Direct numerical simulation (DNS) and low-speed wind-tunnel data, respectively.

4.1 Guide Vane Row in Two-Dimensional Flow

4.1.1 Guide Vane Geometry

The LPT guide-vane geometry was generated using the eleven parameter method of Pritchard (1985) as summarized in Appendix A. This method uses

eleven independent parameters listed in Table 4.1 to fully define an airfoil profile. The parameters are translated into five points shown in Figure 4.1 and then connected by five mathematical functions: a leading edge circle (No.3 to No.4) a trailing edge circle (No.1 to No.5), a circular arc for the aft suction surface (No.2 to No.1), and a third order polynomial function for the pressure and (No.4 to No.5) suction (No.3 to No.2) surfaces. The parameters used to define the geometry were partially derived from the published data of Zhang et al. (2013).

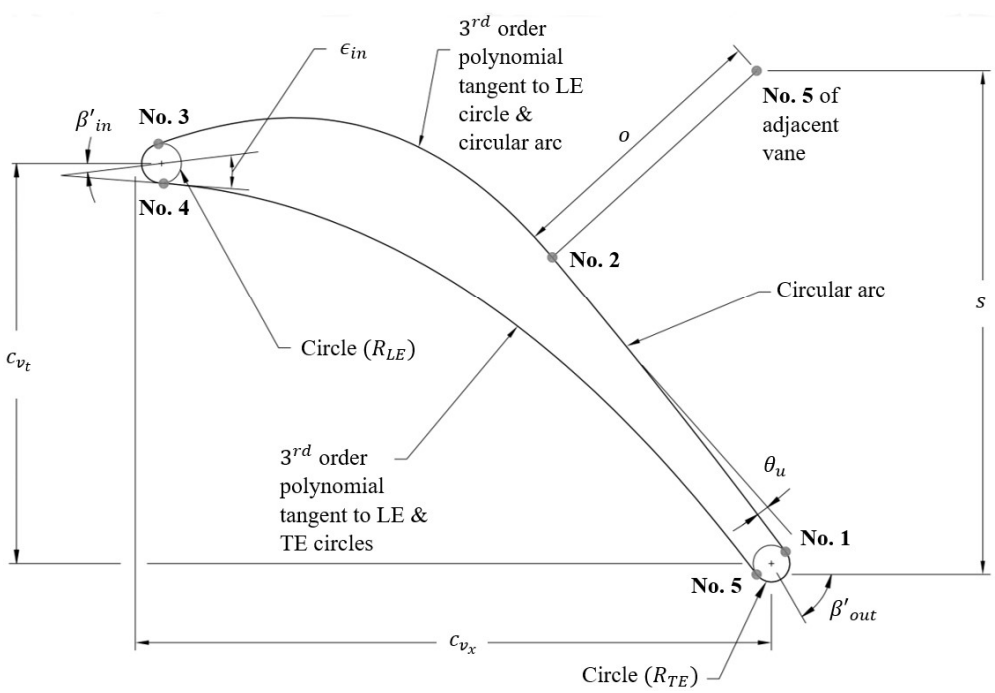

Figure 4.1: Eleven-parameter airfoil design method (adapted from Pritchard, 1985)

Table 4.1: Eleven parameters used to define guide-vane geometry

Symbol	Parameter	VG-1	VG-2	VG-3
β'_{in}	Inlet metal angle	0°	5°	8°
β'_{out}	Exit metal angle	60°	63°	63°
c_{v_x}	Axial chord length	1	1	1
s	Pitch	0.88	0.75	0.75
ϵ_{in}	Leading-edge half wedge angle	8.0°	10.5°	12.0°
θ_u	Unguided turning angle	23°	23°	23°
c_{v_t}	Tangential chord length	0.65	0.64	0.62
R_{LE}	Leading edge radius	0.04	0.03	0.03
R_{TE}	Trailing edge radius	0.03	0.03	0.03
o	Throat width	0.50	0.41	0.41
N_b	Number of guide-vanes in the row	56	56	56

All lengths normalized by the axial chord length (c_{v_x})
VG = Vane Geometry

As shown in Figure 4.2 and Table 4.1, three different guide-vane geometries, each with notable variations in inlet metal angle, β'_{in} were derived. Based on these three geometries, incompressible flow simulations were performed using ANSYS CFX to determine the most suitable guide-vane geometry for the ensuing study.

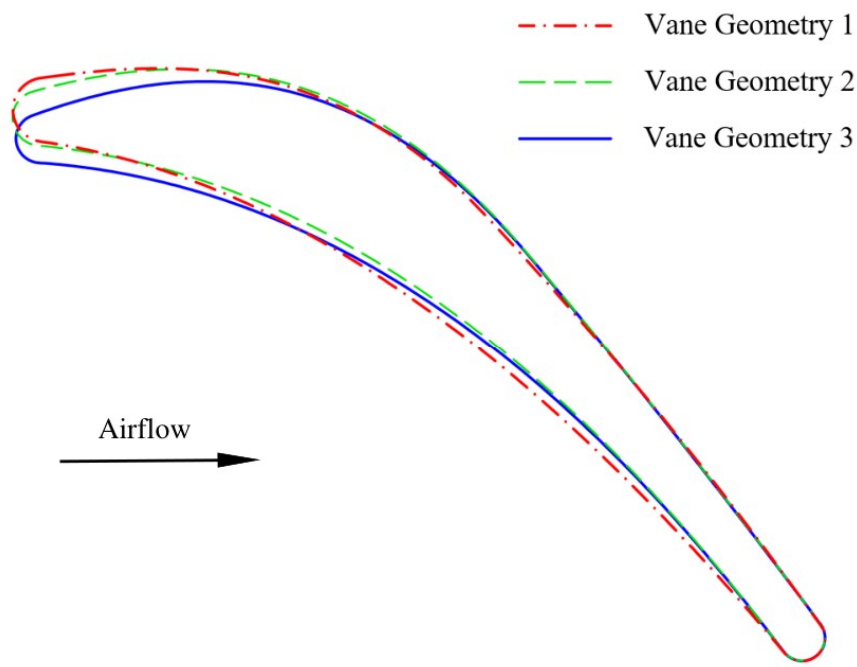

Figure 4.2: Guide-vane geometry

4.1.2 Computational Domain and Boundary Conditions for Simulating the Guide-Vane Aerodynamics

The computational domain for the guide-vane is presented in Figure 4.3. The inflow boundary conditions consisted of a uniform flow velocity yielding a Reynolds number of $200,000$ based on the guide-vane axial chord length, c_{v_x}. The turbulence kinetic energy and specific turbulence dissipation rate specified at the inflow boundary correspond to a turbulence intensity, Tu of 2.3% at the guide-vane inlet which is within the typical range for a gas-turbine ITD installation (Zhang et al., 2013). This high level of freestream turbulence promotes early (bypass) transition on the airfoil surface which justifies the assumption adopted in the present simulations of a fully-turbulent boundary

layer on the guide-vane surface starting at the leading edge. The boundaries terminating the domain in the pitchwise direction were spaced apart one guide-vane pitch, $s = 1.04c_{v_x}$, to enable the imposition of periodic flow conditions at these boundaries. The outflow boundary is defined by a fixed area-averaged static pressure at a conservative distance of $7c_{v_x}$ downstream of the guide-vane trailing-edge plane to allow for the natural development of the wake. The guide-vane surface is defined by smooth, no-slip walls. The domain is set to a spanwise thickness of $0.095c_{v_x}$ to simulate two-dimensional flow with the three-dimensional flow solver of ANSYS CFX. Symmetry boundaries are applied at the domain terminations in the spanwise direction, which impose a zero normal gradient for all computed parameters along the spanwise boundaries.

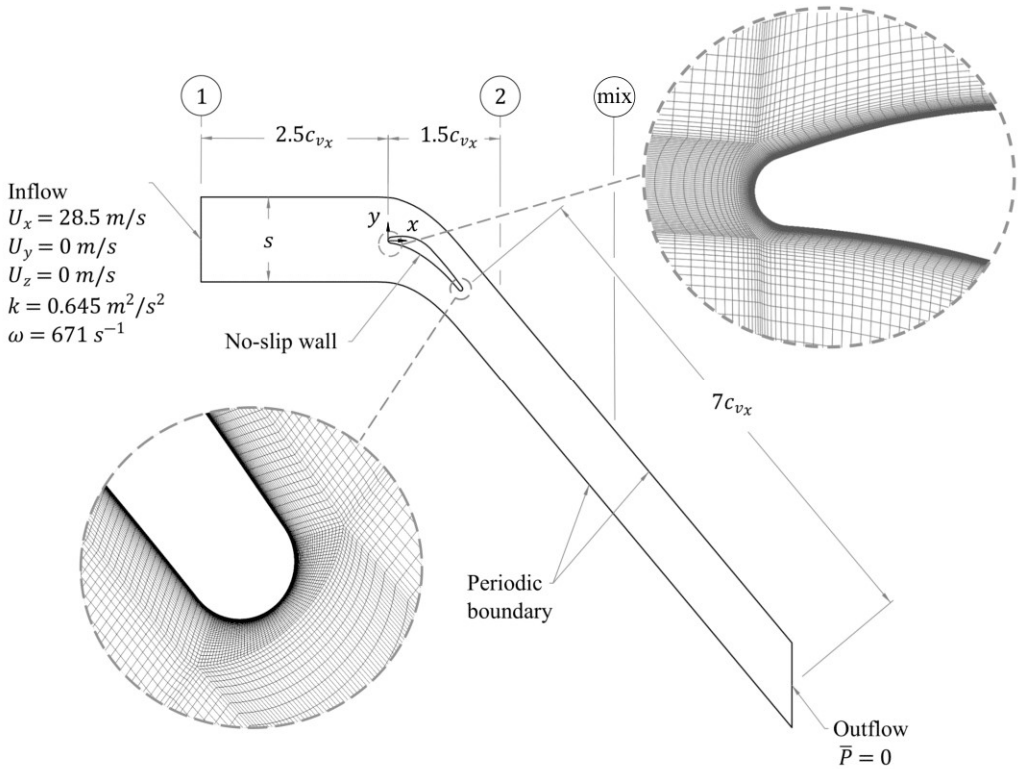

Figure 4.3: Guide-vane row computational domain

4.1.3 Computational Grid for Guide-Vane Row

The computational grid shown in Figure 4.3 was generated using the ICEM software and is based on an H-grid topology, consisting of hexahedral grid cells formed by 8 grid nodes at the cell vertices. The grid cells were clustered towards the solid boundaries of the domain to resolve the boundary layers and the wake regions where free-shear layers were expected. The grid-node spacing at the solid walls was chosen to yield a first-node wall-normal grid-node distance of $y^+_{n_1} < 1$, where the + superscript denotes normalization with

the viscous length scale, ν/u_τ, where $u_\tau = \sqrt{\tau_w/\rho}$ is the friction velocity and τ_w is the local wall shear stress. The rate of change in grid-node spacing in the wall-normal direction in close vicinity to the wall was set to 10% following a grid sensitivity analysis whereby the wall-normal grid-node spacing growth rate was progressively reduced until a negligible change in the skin friction distribution, C_f, given by:

$$C_f = \frac{\tau_w}{P_{o,1} - P_1} \tag{4.1}$$

was observed along the guide-vane surface. Similarly, a grid-node count of 60 nodes in the direction of maximum velocity gradient in the guide-vane wake was determined following a grid sensitivity analysis whereby the grid-node count was progressively doubled until the momentum deficit and peak minimum flow velocity converged to within 1% at a streamwise location of $0.5c_{vx}$ downstream from the guide-vane trailing edge. In the streamwise direction, a grid-node count of 60 nodes each was used along the leading and trailing edges and a grid-node count of approximately 150 nodes each was used along the suction and pressure surfaces. Table 4.2 provides a summary of the relevant grid parameters. The aspect ratio, skewness and spatial rate-of-change of grid-node spacing were kept as low as possible to minimize discretization errors in the converged solution and to promote numerical stability. The ranges given for these parameters in Table 4.2 are consistent with the best practises presented in published literature (e.g., Biswas and Strawn, 1998; Katz and Sankaran, 2011).

Table 4.2: Grid specifications for the guide-vane row domain

Parameter	
$y^+_{n_1}$	<1
Maximum aspect ratio of grid cells	8568
Skewness range of grid cells	0-0.55
Maximum rate of change of grid-node spacing	20%
Total number of grid cells in the x-y plane	0.20×10^6
Total number of grid cells in the z-direction	3

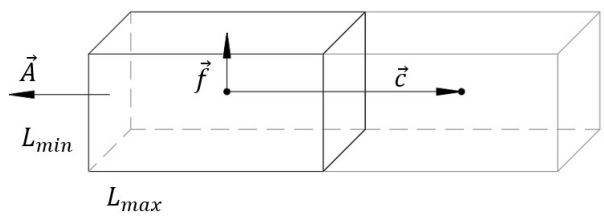

$$\text{Cell Aspect Ratio} = \frac{L_{max}}{L_{min}}$$

$$\text{Cell Size} = (\text{Cell Volume})^{1/3}$$

$$\text{Orthogonal Skew} = \max\left(1 - \frac{\vec{A}_i \cdot \vec{f}_i}{|\vec{A}_i|\,|\vec{f}_i|}, 1 - \frac{\vec{A}_i \cdot \vec{c}_i}{|\vec{A}_i|\,|\vec{c}_i|}\right)$$

$\vec{A}$ = face normal vector

$\vec{f}$ = vector from cell centroid to face centroid

$\vec{c}$ = vector from cell centroid to centroid of adjacent cell

i = face index

4.1.4 Computational Results for the Aerodynamics of the Guide-vane

This section summarizes the numerical simulation results for all three guide-vane geometries using the RANS-based BSL Reynolds-stress model. Figures 4.4 and 4.5 present the variation of mass-averaged profile loss, $\widetilde{C}_{P_{o,mix}}$,

and tangential force coefficient, C_t, with inflow incidence angle, i. The mass-averaged profile loss was calculated using Eq. 2.3 between the stations denoted by 1 and "mix" in Figure 4.3. The latter station represents a hypothetical plane far downstream where the flow has returned to a fully-uniform state. The mixed-out pressure and velocity was calculated based on a mass and momentum balance between plane 2 and this downstream plane as presented in Appendix D. The tangential force coefficient was calculated using:

$$C_t = \frac{F_t}{(P_{o,1} - P_1)c_v h_v} \tag{4.2}$$

where F_t is the tangential force component which is parallel to the leading and trailing edge planes, c_v is the guide-vane chord length and h_v is the guide-vane span which is equal to the spanwise thickness of the computational domain. As shown in Figure 4.4, the minimum profile loss for all three guide-vanes is concentrated near the design incidence angle, with Vane Geometry 3 being the most favourable at both design and off-design conditions. Figure 4.6 and 4.7 present the surface pressure and skin friction distribution for all three guide-vanes at an inflow incidence angle of $i = 0$ deg. Based on Figure 4.6, Vane Geometry 1 and 2 have a noticeably more favourable pressure gradient along the first half of their suction surfaces when compared to Vane Geometry 3, which produces a higher flow acceleration, and larger skin friction magnitude over the first half of their respective suction surfaces and higher adverse pressure gradients that increase the momentum thickness of their boundary layers over the second half, as shown in Figure 4.7. Based on these simulations and supplemental low-speed wind-tunnel testing, Vane Geometry 3 was deemed to have an acceptable baseline performance and was selected for the ensuing

study of the wake interaction between a strut and guide-vane row located in the ITD. The guide-vane geometry does not represent a fully optimized low-pressure guide-vane geometry as further improvements in performance can be made. For identifying the nature of interaction of the strut and guide-vane wakes, which is the objective of the present study, highly optimized geometries for the strut and guide-vane are not required.

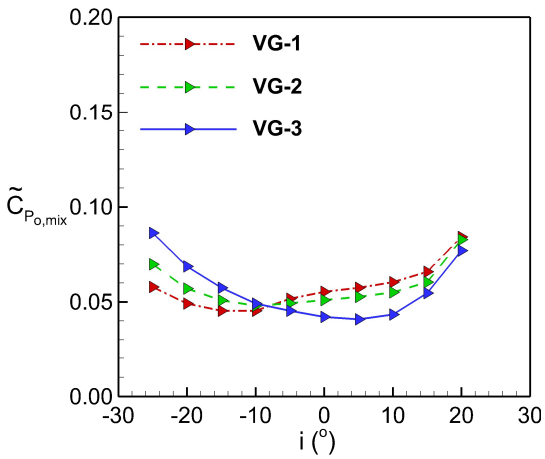

Figure 4.4: Variation of mass-averaged profile loss with incidence angle

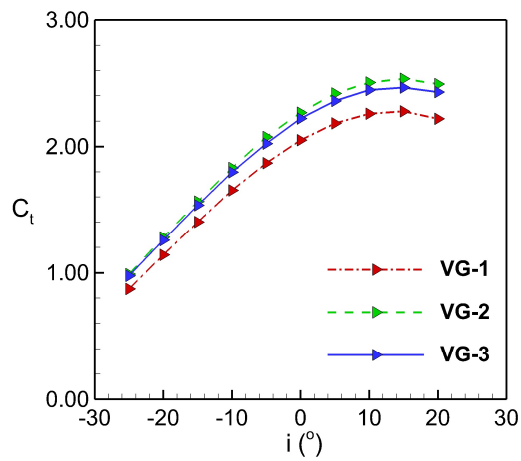

Figure 4.5: Variation of tangential force coefficient with incidence angle

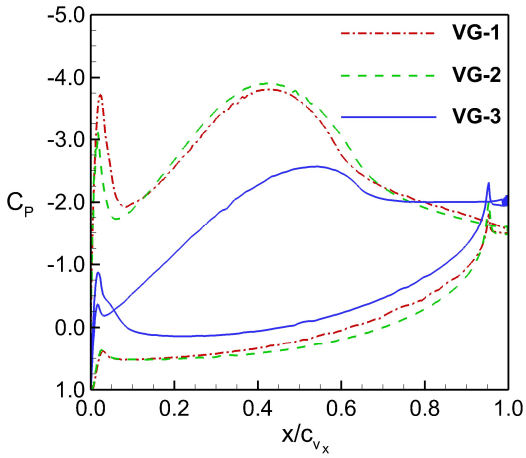

Figure 4.6: Guide-vane surface pressure distribution

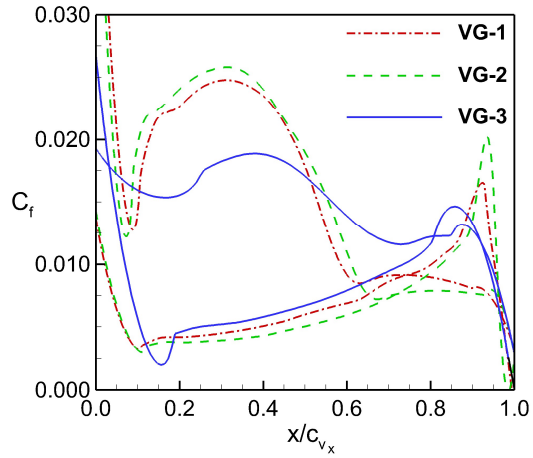

Figure 4.7: Guide-vane surface skin friction distribution

4.2 Single Strut in Two-Dimensional Flow

This section presents the numerical simulation results of an ITD strut using the RANS-based BSL Reynolds-stress model. The strut geometry (shown in red colour) was modelled after the strut of Zhang et al. (2013) which has a chord-to-maximum-thickness ratio of 3.85, as shown in Figure 4.8. The geometry was generated using multipoint Bezier curves via a built-in drawing tool in SketchUp modeling software using a magnified image of the strut acquired from the publication of Zhang et al. (2013).

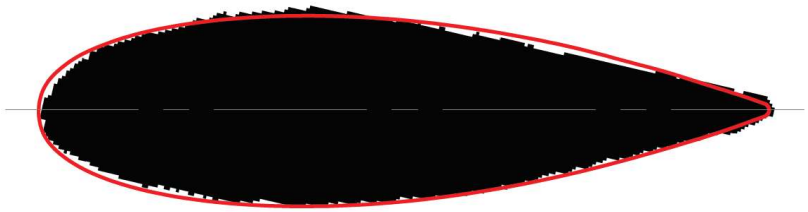

Figure 4.8: Strut geometry (shown in red colour) derived from the strut geometry of Zhang et al. (2013)

Incompressible flow simulations were performed using ANSYS CFX for the strut in a freestream with (1) a uniform, nominally zero streamwise pressure gradient and (2) a streamwise adverse pressure gradient corresponding to the streamwise diffusion rate the strut would experience when installed in the ITD. The study of freestream diffusion on the strut performance was done due to its central streamwise location in the ITD where the diffusion rate is relatively high. Two cases were simulated for the strut: a rectilinear domain with parallel spanwise boundaries where no freestream diffusion was present and a domain with streamwise diverging spanwise boundaries shaped to recreate the streamwise diffusion rate in the ITD.

4.2.1 Computational Domain and Boundary Conditions for Simulating the Strut Aerodynamics

The computational domains for the non-diffusing and diffusing cases are presented in Figure 4.9 and 4.10, respectively. The boundary conditions for both domains are identical with the exception of the spanwise boundaries which are defined by symmetry for the non-diffusing case and free-slip walls for the diffusing case. The location of the domain termination in the upstream direction was established using potential flow theory via the source

panel method, to yield less than 1% and 1° deviation from the far (undisturbed) field value of the velocity magnitude and direction, respectively.

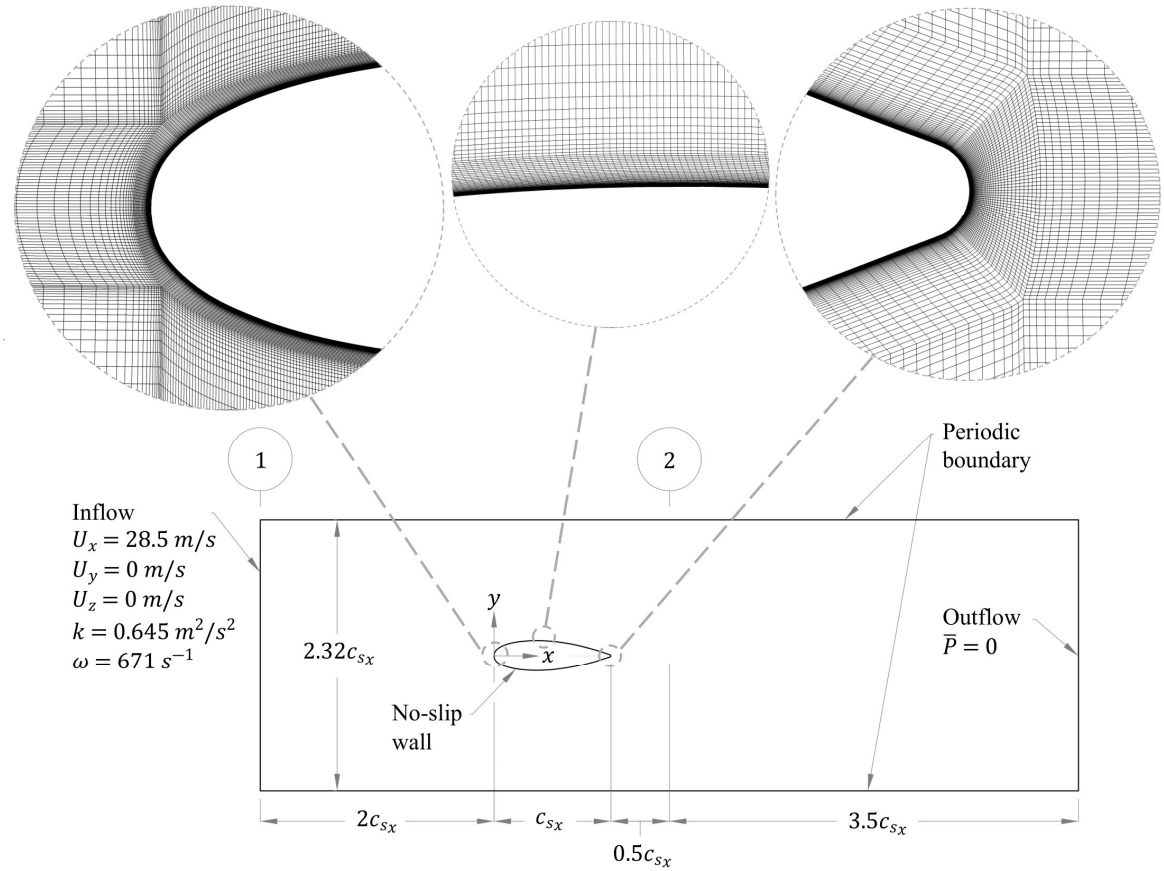

Figure 4.9: Computational domain for strut with non-diffusing freestream (nominally zero streamwise pressure-gradient case)

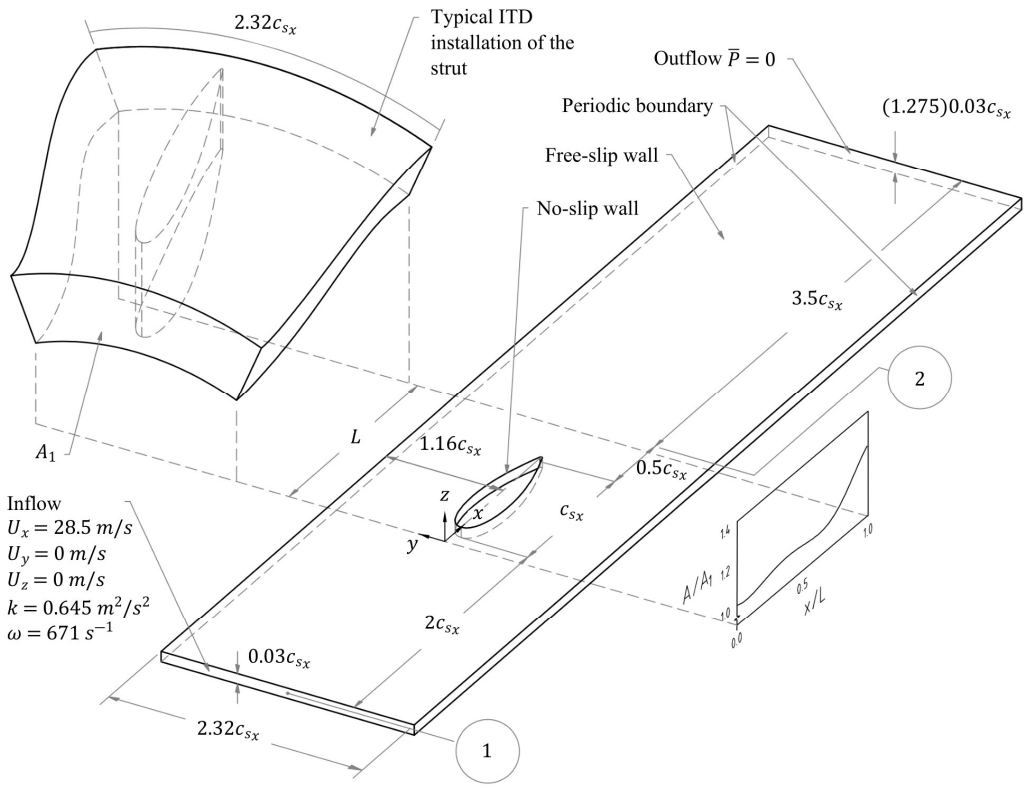

Figure 4.10: Computational domain for strut with diffusing freestream (nominally adverse streamwise pressure-gradient case)

The inflow boundary conditions for both the non-diffusing and diffusing case are identical to the guide-vane row domain described in Section 4.1.2. The boundaries terminating the domain in the pitchwise direction are spaced apart by $2.32c_{s_x}$, which is equal to seven guide-vane pitches ($7s$) and correspond to a guide-vane-to-strut ratio of 8 for a total guide-vane count of $N_b = 56$ as used in Zhang et al. (2013) and as depicted in Figure 1.1. This spacing enables the imposition of periodic flow conditions at the pitchwise boundaries. The outflow boundary is placed $4c_{s_x}$ downstream of the strut trailing-edge plane. The strut surface is defined by smooth, no-slip walls. The domain for the

rectilinear case is set to a constant spanwise thickness of $0.03c_{s_x}$. For the diffusing case, the domain spanwise thickness varies at a rate equal to the streamwise variation of flow area of the baseline ITD geometry of Zhang et al. (2013). The axial extent of varying spanwise thickness is defined by the axial ITD length, $L = 1.59c_{s_x}$ as illustrated in the area graph embedded in Figure 4.10.

4.2.2 Computational Grid for Diffusing and Non-Diffusing Computational Domains

The computational grid for the strut was generated using the same H-grid topology of hexahedral grid cells as the guide-vane row in Section 4.1.3. The grid cells were clustered towards the solid boundaries of the domain to resolve the boundary layers and the wake regions where free-shear layers were expected. The grid-node height at the solid walls was chosen to yield a wall-normal grid-node distance of $y^+_{n_1} < 1$. The rate of change in grid-node spacing in the wall-normal direction in close vicinity to the wall was set to 10% following a grid sensitivity analysis whereby the wall-normal grid-node spacing growth rate was progressively reduced until a negligible change in the skin friction distribution was observed along the strut surface. Similarly, a grid-node count of 60 nodes in the direction of maximum velocity gradient in the strut wake was determined following a grid sensitivity analysis whereby the grid-node count was progressively doubled until the momentum thickness and peak minimum flow velocity converged to within 1% at a streamwise location of $0.5c_{sx}$ downstream from the strut trailing edge. Figure 4.9 illustrates the grid in the immediate vicinity of the strut and Table 4.3 provides a summary of the relevant grid parameters for the strut domain.

Table 4.3: Grid specifications for the non-diffusing and diffusing strut domains

Parameter	
$y_{n_1}^+$	<1
Maximum aspect ratio of grid cells	8568
Skewness range of grid cells	0-0.55
Maximum rate of change of grid-node spacing	20%
Total number of grid cells in the x-y plane	0.20×10^6
Total number of grid cells in the z-direction	3

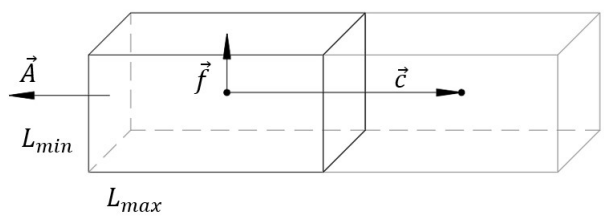

$$\text{Cell Aspect Ratio} = \frac{L_{max}}{L_{min}}$$

$$\text{Cell Size} = (\text{Cell Volume})^{1/3}$$

$$\text{Orthogonal Skew} = \max\left(1 - \frac{\vec{A}_i \cdot \vec{f}_i}{|\vec{A}_i|\,|\vec{f}_i|}, 1 - \frac{\vec{A}_i \cdot \vec{c}_i}{|\vec{A}_i|\,|\vec{c}_i|}\right)$$

$\vec{A}$ = face normal vector

$\vec{f}$ = vector from cell centroid to face centroid

$\vec{c}$ = vector from cell centroid to centroid of adjacent cell

i = face index

4.2.3 Computational Results for the Aerodynamics of the Strut

Figure 4.11 presents the streamwise diffusion rate in the ITD in the absence of any strut or guide-vanes versus the streamwise diffusion rate for the diffusing domain in Figure 4.10. The streamwise diffusion rate for the diffusing domain

was calculated 10% away from the pitchwise boundary where the presence of the strut has a negligible effect on the freestream flow. The comparable diffusion rates between the diffusing domain and the ITD serves to validate the method used for recreating the freestream diffusion present in the ITD for the two-dimensional domain.

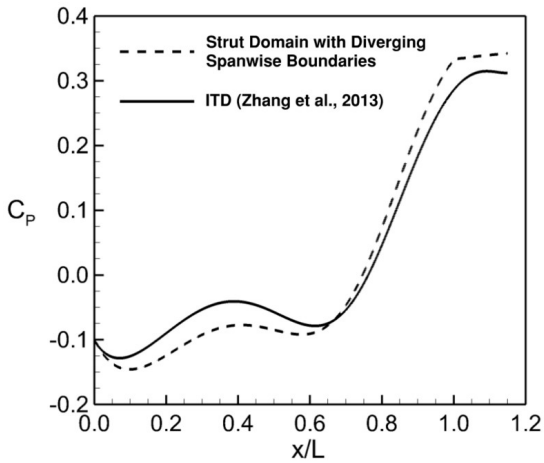

Figure 4.11: Streamwise diffusion for diffusing computational domain vs streamwise diffusion rate in the baseline ITD of Zhang et al. (2013)

Figure 4.12 and Figure 4.13 present the surface pressure and skin friction distribution, respectively, for the non-diffusing and diffusing cases and illustrate the relatively minor effect of the ITD undisturbed freestream deceleration on the strut performance. As shown in Figure 4.13, there is a slight downstream shift of approximately $0.05c_{s_x}$ in the axial location of the maximum wall-shear stress along the strut surface for the diffusing case. As shown in Figure 4.14, the effect of freestream deceleration on the strut wake is very minor as evidenced by a less than 2.5% difference in the wake momentum thickness between the non-diffusing and diffusing cases at a streamwise location of $0.5c_{v_x}$ downstream from the trailing edge plane. Similarly, the mass-averaged profile loss

calculated at a hypothetical downstream plane where the flow is fully mixed (Appendix D), differs by less than 1.5% for the diffusing and non-diffusing cases. Based on these observations, it is determined that the freestream deceleration caused by the ITD geometry is not of primary importance to the strut aerodynamics at midspan and will therefore not be considered in the ensuing numerical and experimental study of aerodynamic interaction of the strut and the guide-vane row.

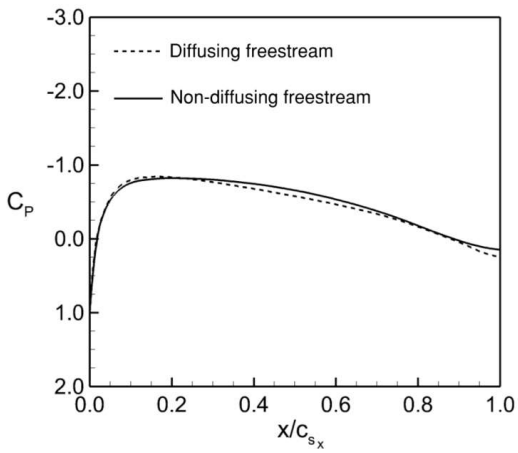

Figure 4.12: Strut surface pressure distribution

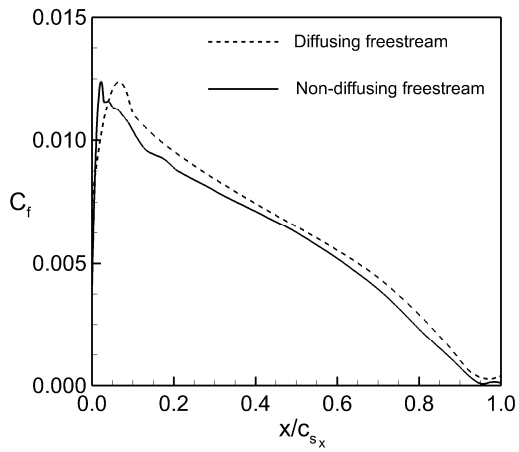

Figure 4.13: Strut surface skin friction distribution

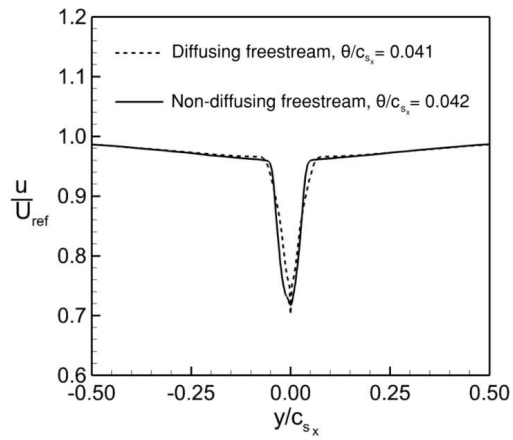

Figure 4.14: Strut wake at $0.5c_{s_x}$ downstream from trailing edge plane

4.3 Experimental and Numerical Study of a Strut and a Row of Guide Vanes in Tandem Configuration

This section presents a study of the RANS-based BSL Reynolds-stress model for a tandem strut and guide-vane row configuration at incompressible flow conditions against experimental data obtained at the Carleton University low-speed wind-tunnel. Upon achieving sufficient agreement between the numerical and experimental benchmark results, the intent is to use the BSL Reynolds-stress model to determine the sensitivity of axial and pitchwise strut positioning on the total profile loss associated with the strut and guide-vane row. From this, a focused test matrix of promising strut positions can be identified and studied further using wind-tunnel tests. The computational domain used to benchmark the RANS-based BSL Reynolds-stress model is therefore modelled after the rectilinear low-speed wind-tunnel at Carleton University.

4.3.1 Low-Speed Cascade Wind-Tunnel

The Carleton University low-speed wind-tunnel is an open circuit, blow-thru design that uses a timing-belt driven centrifugal fan with a variable frequency drive (VFD) to control the AC-motor speed and hence airflow. As shown in Figure 4.15, ambient air is drawn into the fan through a bell-mouth inlet and discharges into a honeycomb section to eliminate swirl followed by a wide-angle diffuser to decrease the flow velocity. The diffuser section contains four equally spaced screens to help improve flow uniformity and reduce the potential for boundary layer separation. This is followed by a settling chamber containing a series of screens and a 14:1 contraction section that accelerates the flow into the test section while transitioning from square to rectangular cross-section. Two static pressure taps are respectively instrumented at the contraction inlet and exit, and are connected to a differential-type pressure transducer that is used to reference the flow field measurements. The test section shown in Figure 4.15 was originally designed by Goobie (1989) and has since been repurposed from past studies of turbine blade rows. For the present study, it consists of a cascade of five guide-vanes and a single strut, constructed from 3D printed ABS plastic, that are mounted on a rotatable turntable to allow for varying inlet flow angles. The turntable is set to produce a 0 deg. incidence angle for the present study. Measurements of the flow field are done using a Pitot pressure probe that enters through a slot in the turntable endwall. The wall opposite to the turntable is made of clear plexiglass mounted on a steel frame with casters that can be easily removed to permit access to the test section. The flow upstream of the test section is uniform and has a turbulence intensity of 0.5%. The endwall boundary layers are bled through slots a short distance downstream of the contraction exit. The

flow downstream of the guide-vane row is confirmed to be periodic through a pitchwise traverse spanning all four guide-vane passages. Periodicity was achieved through a suitable setting of the side-boards and tail-boards and flow uniformity was achieved by adjusting the sideboards shown in Figure 4.15. The flow field is measured along the pitchwise direction at midspan using a 0.64mm-diameter Pitot probe located $0.16c_{v_x}$ downstream of the guide-vane trailing edge plane. The measurements consist of 225 points spaced 0.5mm apart to suitably resolve the strut and middle guide-vane wake. The Pitot pressure is measured relative to the upstream static pressure at tap 2 using a differential pressure transducer. Both the contraction pressure difference and the Pitot probe pressure are sampled at a rate of 50 Hz over a period of 26 seconds. This combination of sampling rate and sampling time was confirmed to yield repeatable long-term averages for the measurements. Upon traverse of the Pitot probe to each sequential measurement location along the pitchwise traverse, the start of data sampling was delayed by a period of 10 seconds to allow for settling of the pressure levels in the tubing connecting the probe to the pressure transducer.

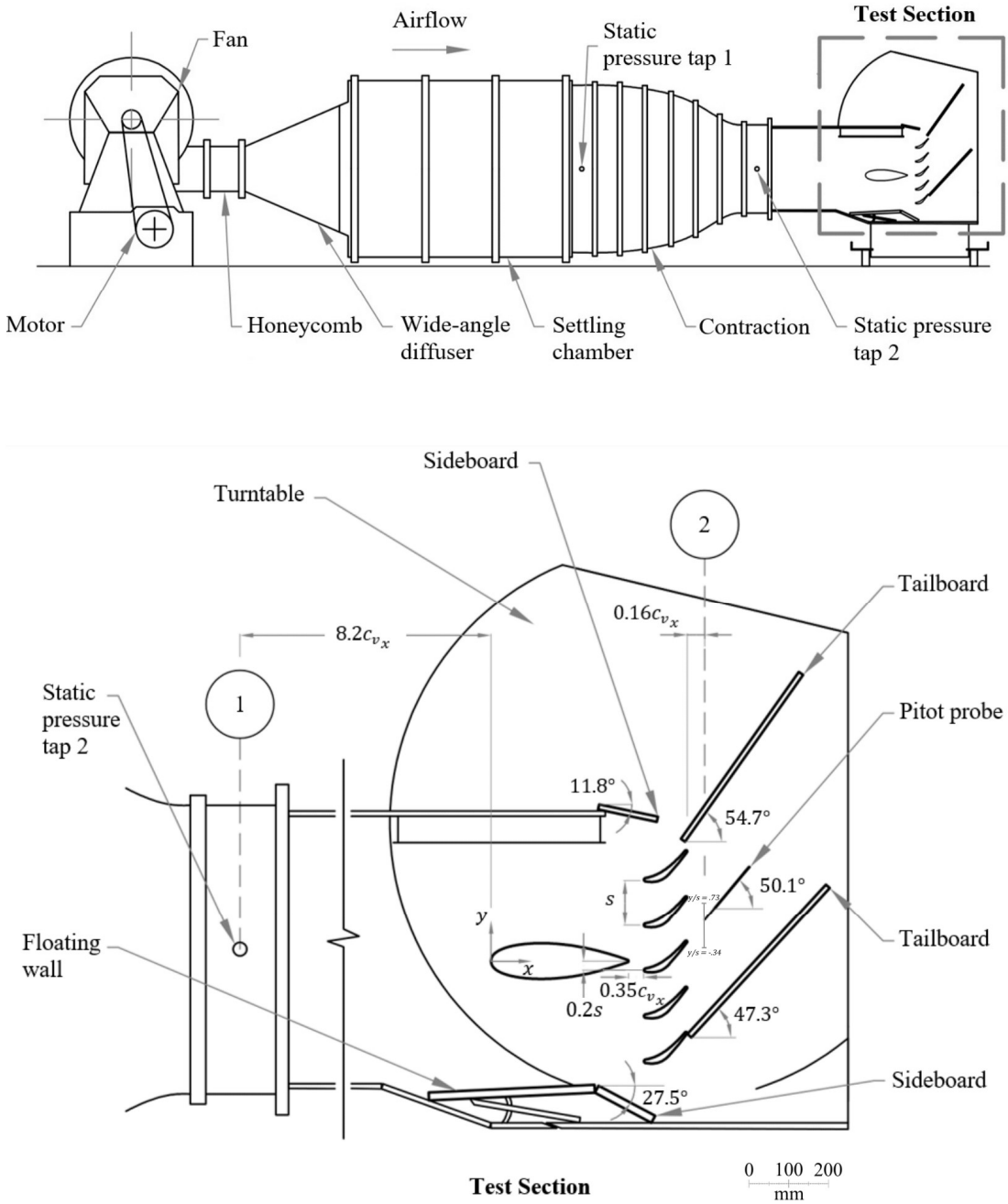

Figure 4.15: Carleton University low-speed cascade wind-tunnel

4.3.2 Computational Domain and Boundary Conditions for a Strut and a Row of Guide-Vanes in Tandem Configuration

The computational domain for the strut and a row of guide-vanes in tandem configuration presented in Figure 4.16 is modelled after the low-speed wind-tunnel cascade test section described in the preceding section. An inflow velocity of 24.2 m/s is used in the computational domain to match the experimentally measured value and an inflow turbulence intensity value of 0.9% is used in the computational domain that decays with streamwise distance to a value of 0.5% at the strut leading edge plane to match the experimentally measured value. At such low levels of freestream turbulence and flow Reynolds number, the boundary layer on the surfaces of the strut and the guide vanes will actually be laminar over a notable portion of the airfoil chord length. The simulation, however, assumes a turbulent boundary layer starting to develop at the airfoil leading edge. This difference will have to be kept in mind in the interpretation of the comparison of the experimental and numerical results. The boundaries terminating the domain in the pitchwise direction are spaced apart by five guide-vane pitches (5s), and are defined by periodic flow conditions. The outflow boundary is defined by a fixed area-averaged static pressure at a location of $5.7c_{v_x}$ downstream of the guide-vane trailing-edge plane to allow for natural development of the wake over a sufficient streamwise distance to facilitate comparison with the experimental results. The guide-vane and strut surfaces are defined by smooth, no slip walls. The strut trailing edge is positioned at an axial distance of $0.35c_{v_x}$ and a pitcwhise distance of $0.2s$ from the middle guide-vane leading edge. The domain is set to a spanwise thickness of $0.095c_{v_x}$ and symmetry boundaries are applied at the domain terminations in the spanwise direction.

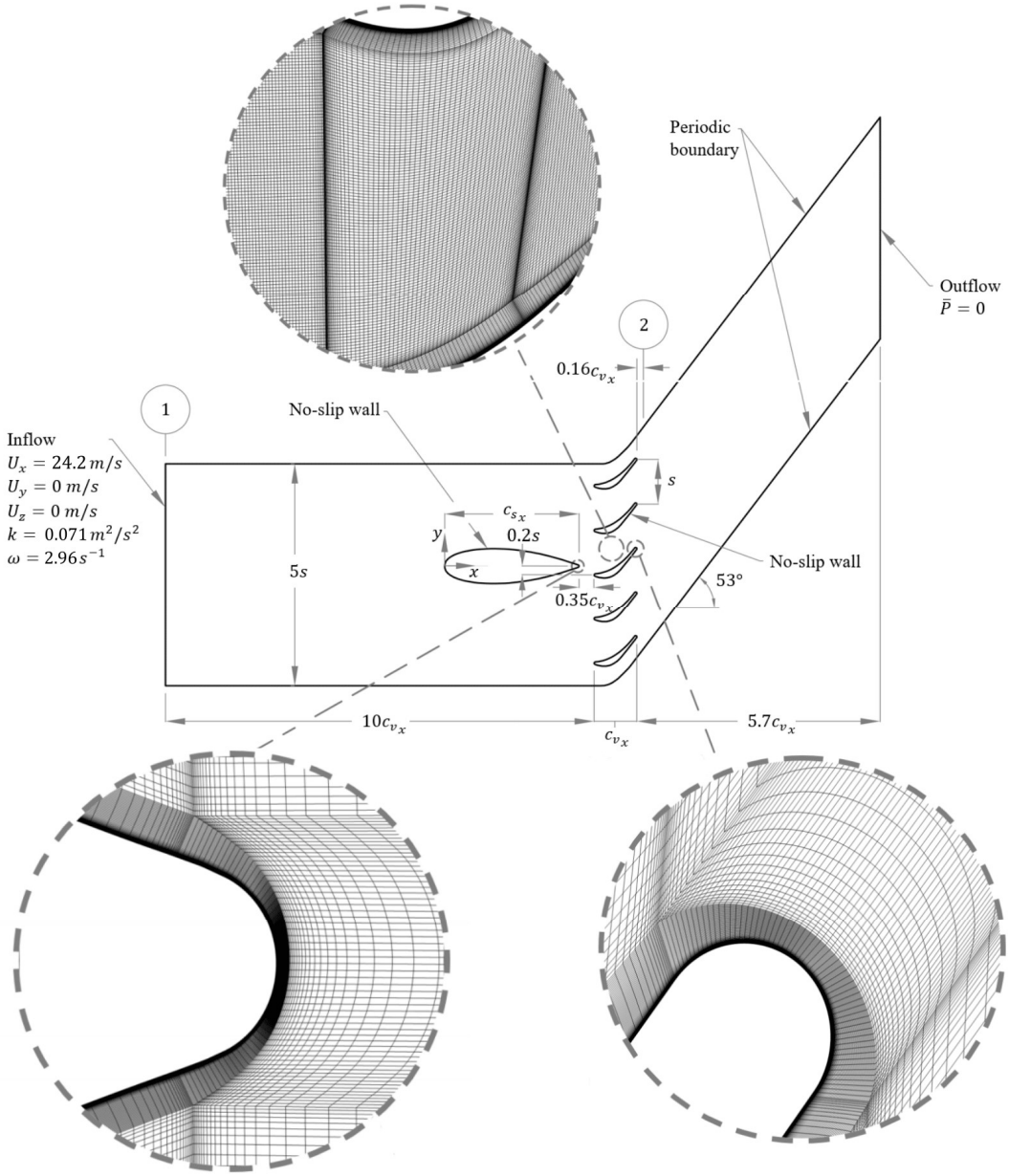

Figure 4.16: Computational domain and grid for a strut and a row of guide-vanes in tandem configuration

4.3.3 Computational Grid for a Strut and a Row of Guide-Vanes in Tandem Configuration

The computational grid for the tandem configuration was generated using the same H-grid topology of hexahedral grid cells, as previously discussed for the strut and all five guide-vanes. The grid cells were clustered towards the solid boundaries of the domain to resolve the boundary layers and the wake regions where free-shear layers were expected. The grid-node height at the solid walls was chosen to yield a wall-normal grid-node distance of $y^+_{n_1} < 1$, The rate of change in grid-node spacing in the wall-normal direction in close vicinity to the wall was set to 10% following a grid sensitivity analysis whereby the wall-normal grid-node spacing growth rate was progressively reduced until a negligible change in the skin friction, C_f, distribution was observed along the middle guide-vane surface. Similarly, a grid-node count of 60 nodes in the direction of maximum velocity gradient in the middle guide-vane wake was determined following a grid sensitivity analysis whereby the grid-node count was progressively doubled until the momentum thickness and peak minimum flow velocity converged to within 1%. Appendix E presents the results of the grid sensitivity study in the middle guide-vane wake and the wall-normal and streamwise grid-node count for the entire domain. Table 4.4 provides a summary of the relevant grid parameters for the tandem domain.

Table 4.4: Grid specifications for strut and a row of guide-vanes in tandem configuration

Parameter	
$y_{n_1}^+$	<1
Maximum aspect ratio of grid cells	9870
Skewness range of grid cells	0.25 - 1
Maximum rate of change of grid-node spacing	20%
Total number of grid cells in the x-y plane	2.61×10^6
Total number of grid cells in the z-direction	3

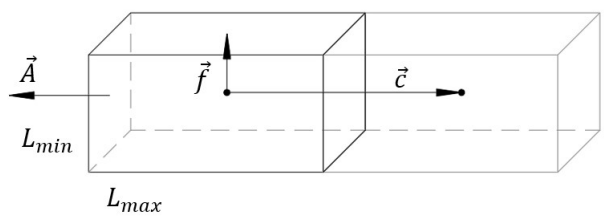

Cell Aspect Ratio $= \frac{L_{max}}{L_{min}}$

Cell Size = (Cell Volume) $^{1/3}$

Orthogonal Skew $= \max\left(1 - \frac{\vec{A}_i \cdot \vec{f}_i}{|\vec{A}_i|\,|\vec{f}_i|}, 1 - \frac{\vec{A}_i \cdot \vec{c}_i}{|\vec{A}_i|\,|\vec{c}_i|}\right)$

$\vec{A}$ = face normal vector

$\vec{f}$ = vector from cell centroid to face centroid

$\vec{c}$ = vector from cell centroid to centroid of adjacent cell

i = face index

4.3.4 Experimental and Numerical Results for a Strut and a Row of Guide-Vanes in Tandem Configuration

As shown in Figure 4.17, notable differences are observed in the pitchwise distribution of the total pressure loss coefficient, $C_{P_{o,2}}$ given by:

$$C_{P_{o,2}} = \frac{P_{o,2} - P_1}{P_{o,1} - P_1} \tag{4.3}$$

between the simulation based on the RANS-based BSL Reynold-stress model and the low-speed wind-tunnel measurements. The subscripts 1 and 2 in Eq. 4.3 correspond to the axial locations denoted in Figure 4.15 and 4.16. In the computed results, the guide-vane and strut wakes are considerably steeper and exhibit a lower rate of pitchwise diffusion when compared to the experimental data, where the strut wake has diffused almost entirely with the adjacent guide-vane wake. Despite this, the momentum thickness in the wake for the computed and experimental data differs by less than 2% as noted in Figure 4.17. In the numerical model, the boundary layers on the strut and guide-vane surfaces are assumed to be fully turbulent over the entire airfoil surface. The actual boundary-layer development on the strut and guide-vane surfaces under low freestream turbulence involves a laminar start of the boundary layer at the leading edge and an eventual natural-mode transition to turbulence at a streamwise location on the airfoil surface that is dictated by the boundary-layer Reynolds number and the prevailing streamwise pressure gradients. This modelling discrepancy is expected to yield a thicker computed boundary layer at the airfoil trailing edge and a more diffused wake state. The results in Figure 4.17 suggest the opposite, which implies that the observed difference between the numerical and experimental wake profiles is not the result of modeling

the boundary layers as turbulent starting at the airfoil leading edge. Instead, the accuracy of the BSL turbulence closure may provide an explanation for the noted difference between the experimental and numerical results. The discrepancy between the numerical and experimental wake profiles motivates a more thorough examination of the RANS-based BSL Reynolds-stress model, which begins with a benchmarking exercise against published direct numerical simulation (DNS) data for a zero-pressure-gradient turbulent flow over a flat-plate. As this is the most fundamental of turbulent flows, it constitutes a good starting point for further scrutiny of the RANS-based BSL turbulence model.

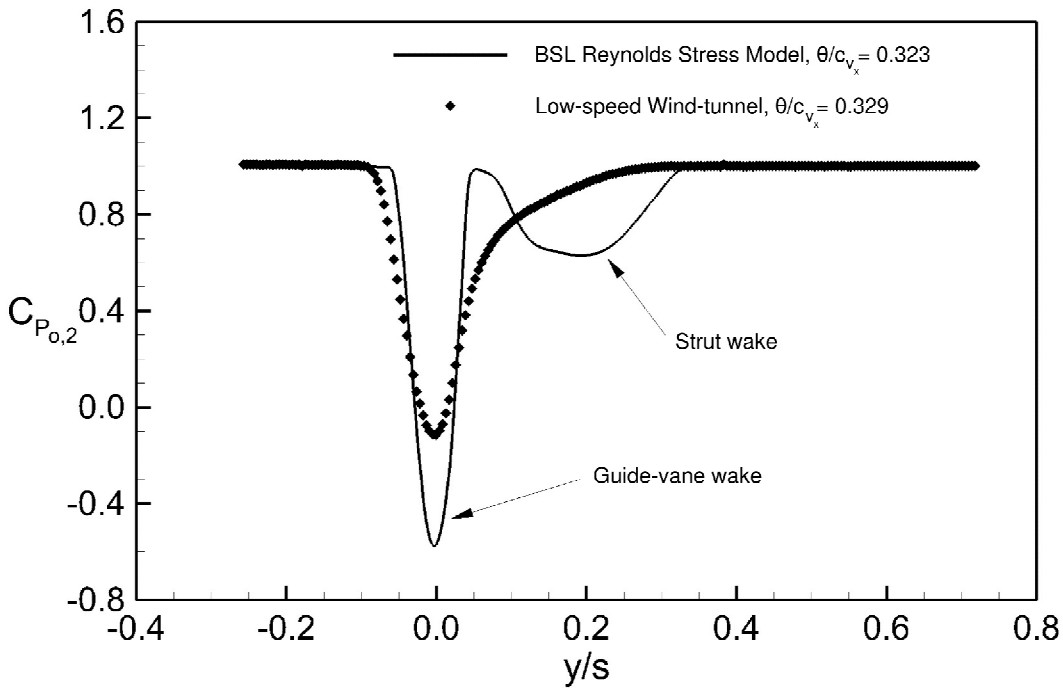

Figure 4.17: Experimental and numerical total pressure loss at an axial location of $0.16c_{v_x}$ downstream of the guide-vane row trailing edge plane

4.4 Zero-Pressure-Gradient Turbulent Boundary Layer

This section presents the numerical study of the development of a zero-pressure-gradient turbulent boundary layer on a flat-plate using the RANS-based BSL Reynolds-stress model. The purpose of this study is to determine whether the individual terms of the Reynolds-stress transport equations in the RANS-based BSL Reynolds-stress model accurately represent the physics when compared against published DNS data. Although this type flow is different from the wall-jet-like boundary layer flow present in the tandem strut and guide-vane row results presented in Section 4.3.4, this benchmark serves to demonstrate the best prediction accuracy that can be expected for the RANS-based BSL Reynolds-stress model given that a zero-pressure-gradient turbulent boundary layer is the most simple turbulent shear flow that is used in the calibration of turbulence models.

4.4.1 Computational Domain and Boundary Conditions for a Zero-Pressure-Gradient Turbulent Boundary Layer

The computational domain for the zero-pressure-gradient turbulent boundary layer is shown in Figure 4.18. The inflow boundary condition consists of a uniform velocity of 10 m/s, a turbulence intensity of 0.1% and a turbulence length scale, l_t of 0.001m. The turbulence intensity was kept very low to match the DNS simulation of Spalart (1988) which has a fully laminar freestream flow, i.e. a turbulence intensity of zero which is not an acceptable boundary condition for the BSL turbulence model. Hence, a minimal value of 0.1% at the inflow boundary allows for the streamwise decay in turbulence intensity to a negligible value at a streamwise location where the momentum thickness Reynolds number, Re_θ equals 1410. This particular Reynolds num-

ber was chosen to match the DNS results of Spalart (1988) and corresponds to streamwise location of $0.635L_{fp}$ for the present domain, where L_{fp} is the domain length in the streamwise direction. The bottom streamwise boundary is modelled primarily as a smooth, no-slip wall to represent a flat-plate with a small upstream section of length $0.03L_{fp}$ modelled as a free-slip wall to prevent artificially influencing the velocity at the plate leading edge. The outflow boundary is placed sufficiently far downstream to allow for the natural development of the boundary layer up to the boundary layer Reynolds number of interest, and is constrained by an area-averaged static pressure. The top streamwise boundary is modelled as a free-slip wall. The domain height of $0.5L_{fp}$ is set to yield a negligible streamwise acceleration of the freestream as represented by a domain inflow-to-outflow velocity ratio of 1.005. The domain is set to an arbitrary spanwise thickness of $0.06L$ to simulate two-dimensional flow with the three-dimensional flow solver of ANSYS CFX and is terminated in the spanwise direction by symmetry boundaries.

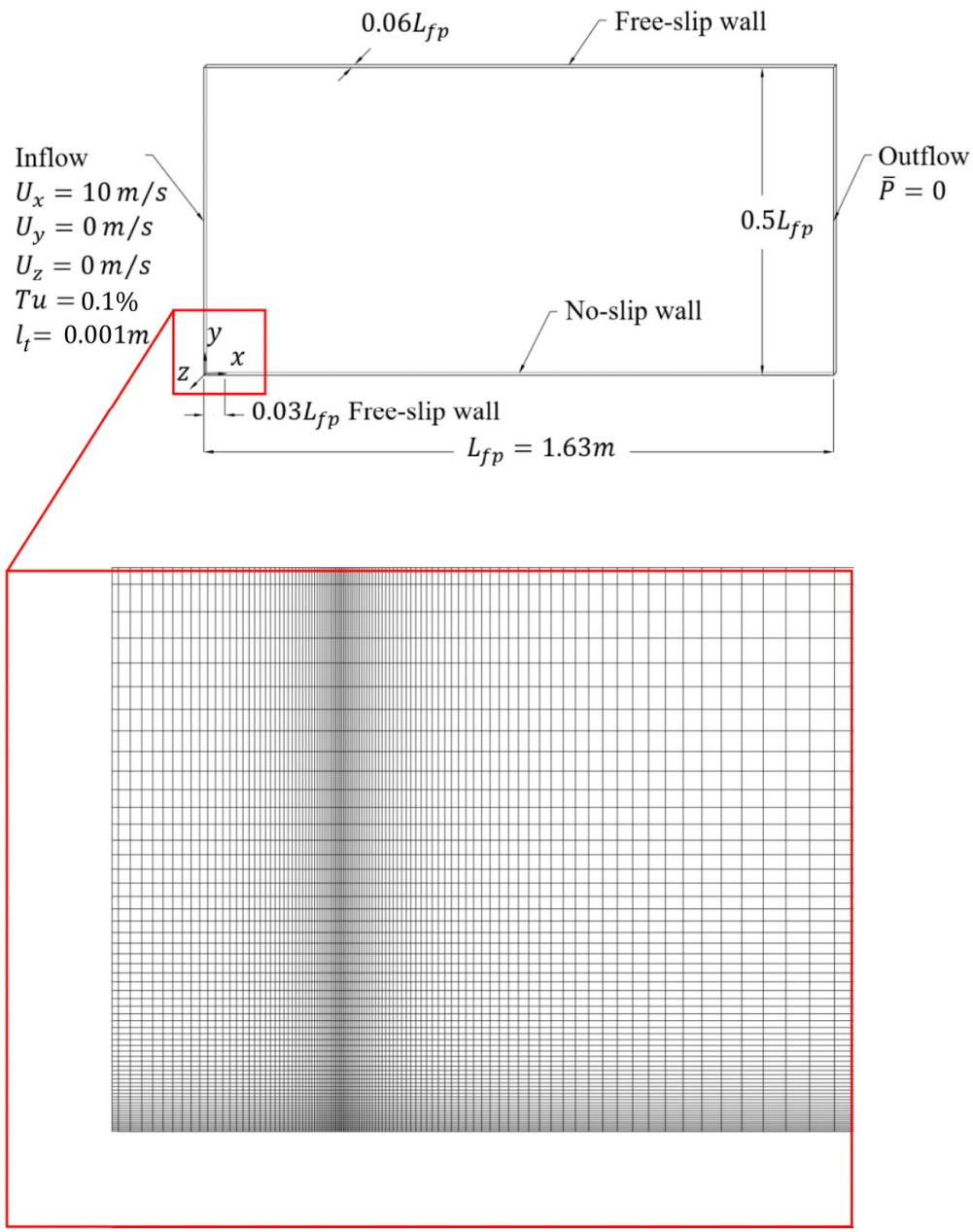

Figure 4.18: Zero-pressure-gradient turbulent boundary layer computational domain

4.4.2 Computational Grid for a Zero-Pressure-Gradient Turbulent Boundary Layer

The computational grid consists of structured hexahedral cells that were generated using the ICEM software. The grid cells were clustered towards the no-slip wall to resolve the velocity gradients in the boundary layer. The grid-node height at the solid wall was chosen to yield a first-node wall-normal grid-node distance of $y^+_{n_1} < 1$, which was determined through a sensitivity analysis of the momentum thickness Reynolds number at a streamwise location of $x = 0.635L_{fp}$. The rate of change in grid-node spacing in the wall-normal direction in close vicinity to the no-slip wall was set to 5% to achieve the desired resolution of the boundary layer. The boundary layer resolution was determined by progressively reducing the growth rate of the grid-node spacing in the wall-normal direction until the momentum thickness Reynolds number converged to within 1% at a streamwise location of $x = 0.635L_{fp}$. To resolve the streamwise growth of the boundary layer, the grid-node spacing and rate of change in grid-node spacing in the streamwise direction in close vicinity to the plate leading edge plane was identical to the grid-node spacing at the wall and growth rate in the wall-normal direction, respectively. The grid-node spacing in the streamwise and wall-normal directions are presented in Figure 4.19 and 4.20, respectively.

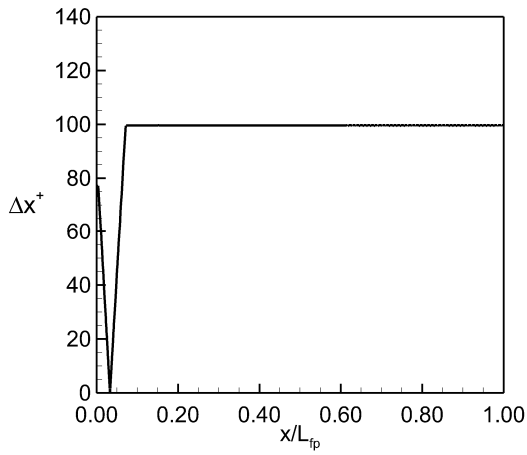

Figure 4.19: Streamwise grid-node spacing for zero-pressure-gradient turbulent boundary layer grid

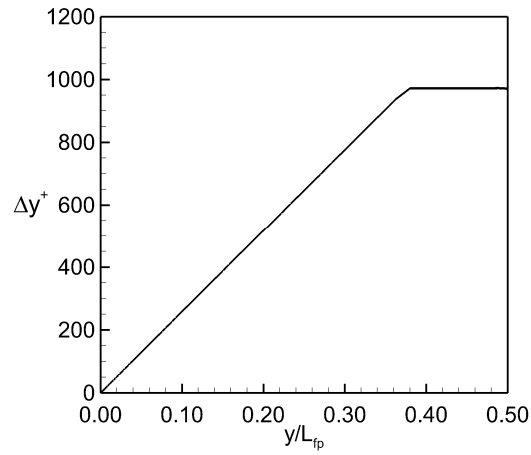

Figure 4.20: Wall-normal grid-node spacing for zero-pressure-gradient turbulent boundary layer grid

The normalized streamwise (Δx^+) and wall-normal (Δy^+) grid-node spacing shown in Figure 4.19 and 4.20, respectively, are normalized by the viscous length scale, $\delta_\nu = \nu/u_\tau$, where u_τ is the friction velocity as defined by the local wall shear stress at $x = 0.635L_{fp}$ which is estimated empirically using the skin friction coefficient, C_f, correlation for a turbulent boundary layer over a flat-plate given by:

$$C_f = \frac{0.074}{Re_{0.635L_{fp}}^{1/5}} \tag{4.4}$$

where $Re_{0.635L_{fp}}$ is the Reynolds number based on the length corresponing to the streamwise location of $0.635L_{fp}$. The discretization error of the computational grid was calculated to be $7.39 \times 10^{-4}\%$ based on the Richardson extrapolation method (Richardson, 1910) for non-integer grid refinement ratios (Appendix F). Table 4.5 provides a summary of the relevant grid parameters used for the turbulent boundary layer.

Table 4.5: Grid specifications for the zero-pressure-gradient turbulent boundary layer domain

Parameter	
$y_{n_1}^+$	<0.5
Maximum aspect ratio of grid cells	278
Skewness range of grid cells	0
Maximum rate of change of grid-node spacing	5%
Total number of grid cells in the x-y plane	0.18×10^6
Total number of grid cells in the z-direction	3

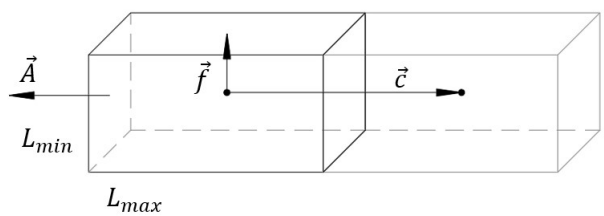

Cell Aspect Ratio $= \dfrac{L_{max}}{L_{min}}$

Cell Size $=$ (Cell Volume) $^{1/3}$

Orthogonal Skew $= \max\left(1 - \dfrac{\vec{A}_i \cdot \vec{f}_i}{|\vec{A}_i|\,|\vec{f}_i|}, 1 - \dfrac{\vec{A}_i \cdot \vec{c}_i}{|\vec{A}_i|\,|\vec{c}_i|}\right)$

$\vec{A}$ = face normal vector

$\vec{f}$ = vector from cell centroid to face centroid

$\vec{c}$ = vector from cell centroid to centroid of adjacent cell

i = face index

4.4.3 Computational Results for a Zero-Pressure-Gradient Turbulent Boundary Layer

This section presents the computational results based on the RANS-based BSL Reynolds-stress model for a zero-pressure-gradient turbulent boundary layer along a flat-plate against the DNS results of Spalart (1988). The computational results were found to be independent of the freestream turbulence intensity applied at the inflow computational boundary as discussed in Section 4.4.1. Figure 4.21 presents the wall-normal profile for the normalized streamwise velocity, $u^+ = u/u_\tau$, of the RANS-based BSL Reynolds-stress model and the DNS results of Spalart (1988) at a streamwise location corresponding to the momentum thickness Reynolds number of $Re_\theta = 1410$.

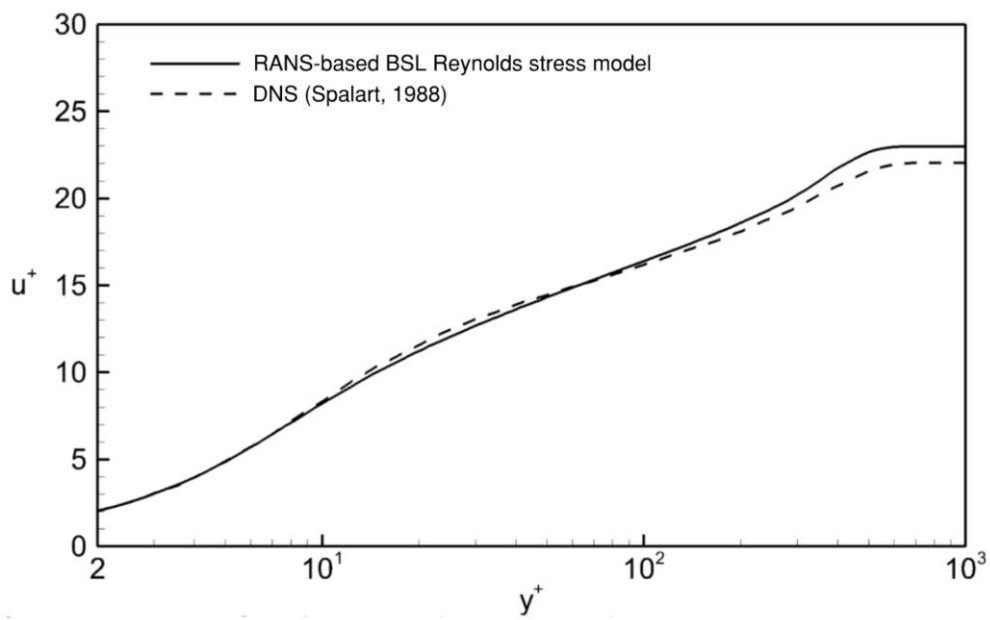

Figure 4.21: Normalized wall-normal profile of streamwise velocity at $Re_\theta = 1410$

Figure 4.22 presents the wall-normal profile of the production (P_{11}^{+}), pressure-strain rate (Φ_{11}^{+}), viscous diffusion ($D_{11}^{\mu+}$), turbulence diffusion ($D_{11}^{\tau+}$) and dissipation (ϵ_{11}^{+}) term appearing in the transport equation of the normal component of Reynolds-stress, $\overline{u_1'u_1'}$, in the RANS-based BSL Reynolds-stress model and the corresponding DNS results of Spalart (1988) at a streamwise location corresponding to $Re_\theta = 1410$. The wall-normal profiles for the remaining normal Reynolds-stress components of $\overline{u_2'u_2'}$ and $\overline{u_3'u_3'}$ are presented in Appendix G. All terms shown in Figure 4.22 are normalized by the kinematic viscosity, ν, and the friction velocity, u_τ. As shown in Figure 4.22, there is good agreement for the Reynolds-stress production, P_{11}^{+}, between the RANS-based BSL Reynolds-stress model and DNS data throughout the entire boundary layer. For a simple shear flow where the only significant gradient in time-mean velocity is in the wall-normal direction, the turbulence kinetic energy production is entirely in $\overline{u_1'u_1'}$ and reaches a maximum value near the wall (Pope, 2000). In the case of the Reynolds-stress dissipation, ϵ^{+}, there is a significant deviation near the wall ($y^{+} \leq 10$) between the RANS-based BSL data and DNS data. For the DNS data, the maximum value of dissipation occurs at the wall boundary, whereas in the RANS-based BSL model the dissipation is zero at the wall boundary. Furthermore, the RANS-based BSL data assumes isotropic dissipation everywhere in the flow as seen in Eq. 3.11 where the diagonal components representing the normal components of the dissipation-rate tensor are of equal value and the off-diagonal components are zero. This assumption is not valid in the near-wall region where the dissipation is actually anisotropic (Saddoughi and Veeravalli, 1994). It appears that the lack of dissipation in $\overline{u_1'u_1'}$ produced by ϵ^{+} and the viscous and turbulent diffusion terms ($D^{\mu+}$ and $D^{\tau+}$, respectively) in the RANS-based BSL Reynolds-stress model is compensated by the greater contribution of the pressure-strain rate term, Φ^{+}, which

forces isotropic turbulence by redistributing turbulence kinetic energy from the largest normal Reynolds-stress, $\overline{u_1'u_1'}$, to the lesser normal stresses, $\overline{u_2'u_2'}$ and $\overline{u_3'u_3'}$. Contrary to the DNS results, the pressure-strain-rate term in the RANS-based BSL Reynolds-stress model is the dominant term that is responsible for removing turbulence kinetic energy from $\overline{u_1'u_1'}$. As such, the influence of the viscous and turbulent diffusion terms in the RANS-based BSL Reynolds-stress model is relatively minor, particularly the turbulent diffusion term which is almost negligible, when compared to the DNS results.

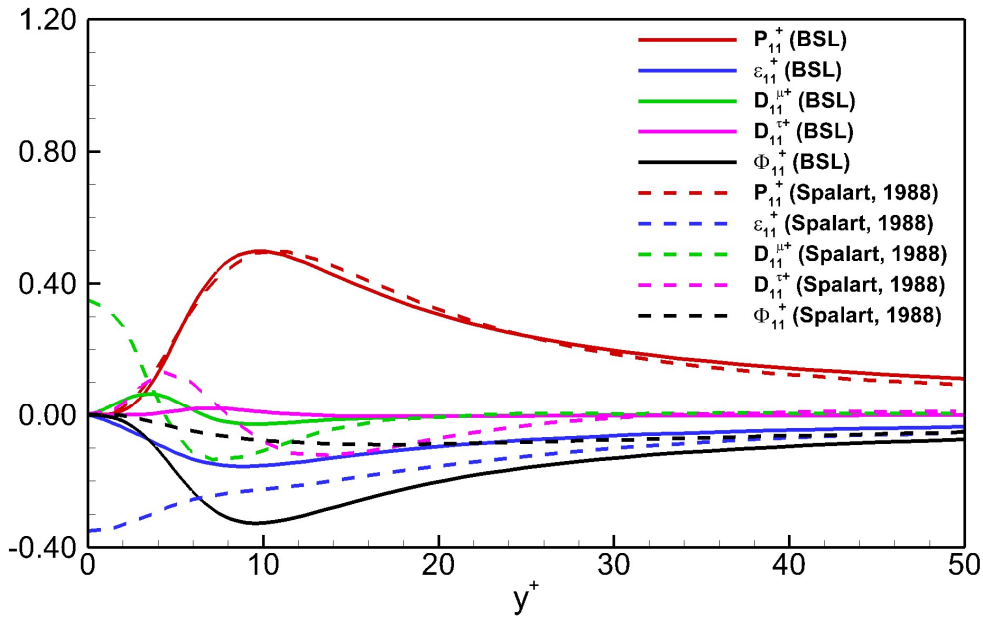

Figure 4.22: Wall-normal variation of the terms in the $\overline{u_1'u_1'}$ Reynolds-stress transport equation at $Re_\theta = 1410$

4.5 Planar Turbulent Free-Shear Layer

This section presents the numerical study of the flow development of a planar turbulent free-shear layer using the RANS-based BSL Reynolds-stress model against the experimental splitter-plate wake data of Mehta (1991). The purpose of this study is to determine the ability of the RANS-based BSL Reynolds-stress model to accurately simulate the most basic free-shear layer and to provide insight into the discrepancy between the experimental and numerical results for the tandem strut and guide-vane row presented in Section 4.3.4.

4.5.1 Computational Domain and Boundary Conditions for a Planar Turbulent Free-Shear Layer

As shown in Figure 4.23, the computational domain and boundary conditions of the planar turbulent free-shear layer are modelled after the experimental setup of Mehta (1991). The inflow boundary condition consists of two separate zero-pressure-gradient turbulent boundary layers defined by a high-speed and low-speed freestream velocity of $U_{1_x} = 21$ m/s and $U_{2_x} = 19$ m/s, respectively, on either side of the splitter-plate. The high-speed and low-speed velocity profiles were selected from the DNS boundary layer profile library of Pirozolli et al. (2010) to match the shape factor, H, momentum thickness, θ, and boundary layer thickness, δ_{99} (subscript 99 denotes the wall-normal location where the viscous flow velocity is 99% of the freestream velocity), used in the experimental setup of Mehta (1991) and are denoted by a subscript of 1 and 2 for the high-speed and low-speed streams, respectively. A turbulence integral length scale of 0.75×10^{-3}m and 1.0×10^{-3}m is defined at the inflow boundary for the high-speed and low-speed freestreams, respectively,

and a turbulence intensity of 0.15% is defined for both freestreams to match the inflow conditions used by Mehta (1991). The splitter-plate trailing edge thickness is $t_{sp} = 8.0 \times 10^{-5} L_{sp}$, where the splitter-plate length is $L_{sp} = 3.13$m to match the experimental conditions of Mehta (1991). The boundaries terminating the domain in the pitchwise direction are spaced apart by $0.19L_{sp}$ to match the experimental conditions of Mehta (1991) and are modelled as free-slip walls. The outflow boundary is constrained by a fixed area-averaged static pressure at a location $1.17L_{sp}$ downstream of the splitter-plate trailing edge to represent the open wind-tunnel termination to atmosphere used in the experimental setup of Mehta (1991). As the flow simulation is performed for incompressible conditions, the value of this static pressure is arbitrarily set to zero. The domain is set to an arbitrary spanwise thickness of $0.01L_{sp}$ and symmetry boundaries are applied at the domain terminations in the spanwise directions.

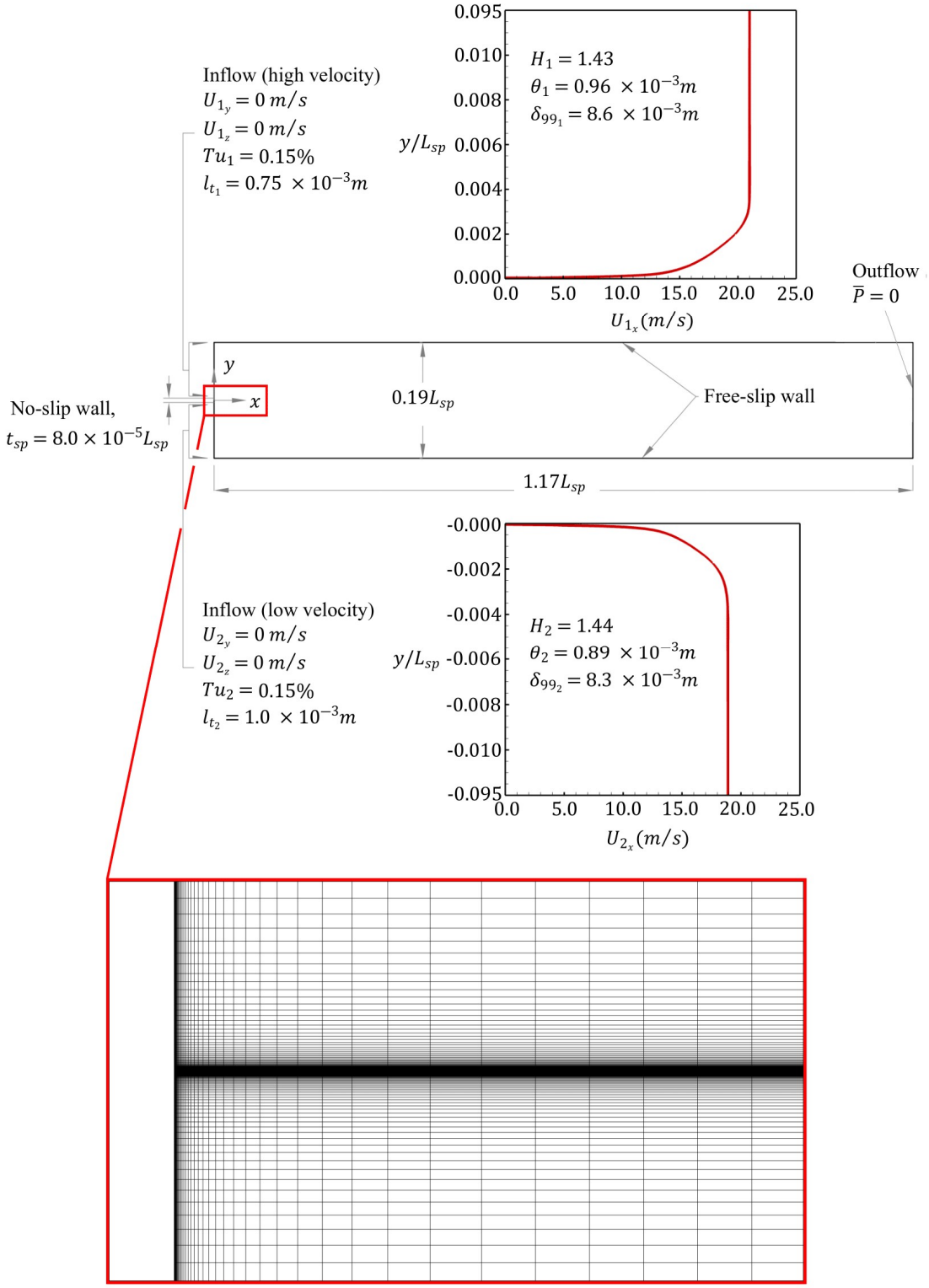

Figure 4.23: Splitter-plate computational domain

4.5.2 Computational Grid for a Planar Turbulent Free-Shear Layer

The grid-node spacing in the streamwise (Δx^+) and pitchwise (Δy^+) directions are presented in Figure 4.24 and 4.25, respectively. The streamwise and pitchwise grid-node spacings are normalized by the viscous length scale, $\delta_\nu = \nu/u_\tau$, where $u_\tau = \sqrt{\tau_w/\rho}$ and τ_w is the local wall shear stress on the high-speed side of the splitter-plate trailing edge ($x = 0$). τ_w is calculated from the empirical skin friction correlation given by Eq. 4.4, where the characteristic length scale used for the Reynolds number is based on L_{sp} instead of $0.635L_{fp}$. The minimum grid-node spacing in the pitchwise direction was chosen to be $1.0 \times 10^{-3} t_{sp}$ and was located at a pitchwise location of $y/L_{sp} = 0$. The rate of change in grid-node spacing in the pitchwise direction towards the pitchwise boundaries of the domain was set to 5% following a grid sensitivity analysis whereby the pitchwise grid-node-spacing growth rate was progressively reduced until a negligible a change in the mixing-layer growth rate was observed. Similarly, the rate of change in grid-node spacing in the streamwise direction was set to 15% following a grid sensitivity analysis whereby the streamwise grid-node spacing growth rate was progressively reduced until a negligible a change in the mixing-layer growth rate was observed. Table 4.6 provides a summary of the relevant grid parameters used for the planar turbulent free-shear layer domain.

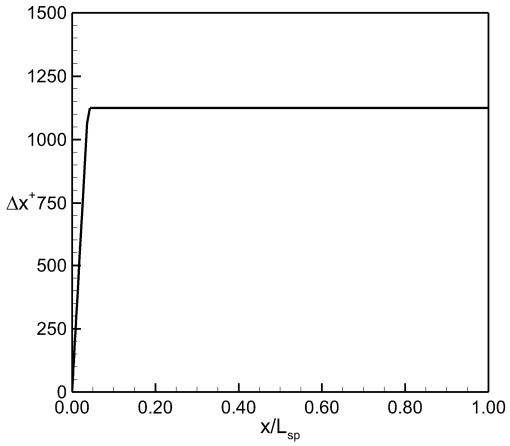

Figure 4.24: Streamwise grid-node distribution for the planar turbulent free-shear layer

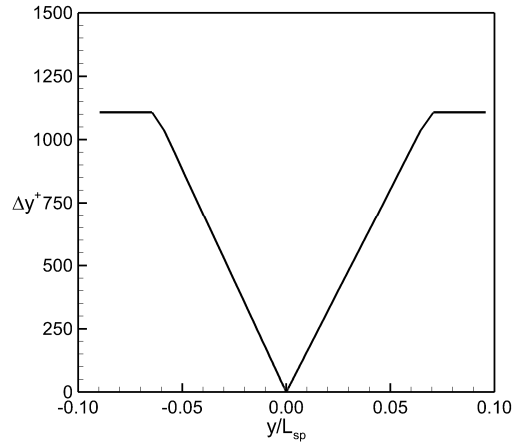

Figure 4.25: Pitchwise grid-node distribution for the planar turbulent free-shear layer

Table 4.6: Grid specifications for the planar turbulent free-shear layer domain

Parameter	Value
$y_{n_1}^+$	<0.5
Maximum aspect ratio of grid cells	237
Skewness range of grid cells	0
Maximum rate of change of grid-node spacing	15%
Total number of grid cells in the x-y plane	0.15×10^6
Total number of grid cells in the z-direction	3

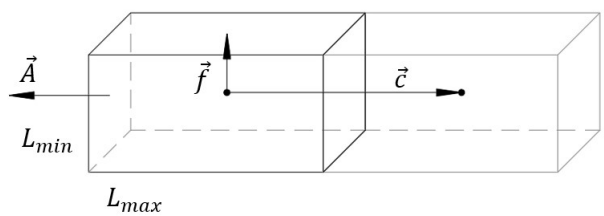

Cell Aspect Ratio $= \dfrac{L_{max}}{L_{min}}$

Cell Size $=$ (Cell Volume) $^{1/3}$

Orthogonal Skew $= \max\left(1 - \dfrac{\vec{A}_i \cdot \vec{f}_i}{|\vec{A}_i|\,|\vec{f}_i|}, 1 - \dfrac{\vec{A}_i \cdot \vec{c}_i}{|\vec{A}_i|\,|\vec{c}_i|}\right)$

$\vec{A}$ = face normal vector

$\vec{f}$ = vector from cell centroid to face centroid

$\vec{c}$ = vector from cell centroid to centroid of adjacent cell

i = face index

4.5.3 Computational Results for a Planar Turbulent Free-Shear Layer

Similar to the tandem strut and guide-vane row results presented in Section 4.3.4, the RANS-based BSL Reynolds-stress model produced a velocity profile downstream of the splitter-plate that is much steeper and exhibits less diffusion between the high and low velocity streams than the experimental data. In an effort to better match the experimental velocity profile, the calibration procedure of Yoder (2005) was employed, which involved incremental adjustments to coefficients, C_1 and C_2 associated with the slow and fast subterms, respectively, in the pressure-strain rate term, Φ_{ij}, given in Eq. 3.14. The complete results of the calibration procedure are presented in Appendix H. As shown in Figure 4.26, adjustments to C_1 and C_2, resulted in only a slight reduction in the velocity peak magnitude, at the expense of an increased and less accurate mixing-layer growth rate measured downstream of the splitter-plate. As shown in Figure 4.27, the default values for coefficient C_1 and C_2 produce a mixing-layer growth rate that resembles the experimental data of Mehta (1991) to within 11% as opposed to the modified values of $C_1 = 0.81$ and $C_2 = 0.23$ which produce an error of approximately 130%. Design optimization of the aerodynamic interaction of the strut and the guide-vane row demands that the shear profiles of the wakes be predicted accurately and not just their streamwise growth rates. The results of the present benchmark appear to suggest that RANS turbulence models may not be sufficiently accurate for this. Alternative approaches to this aerodynamic design optimization problem are large-eddy-simulation, direct-numerical simulation or experimentation.

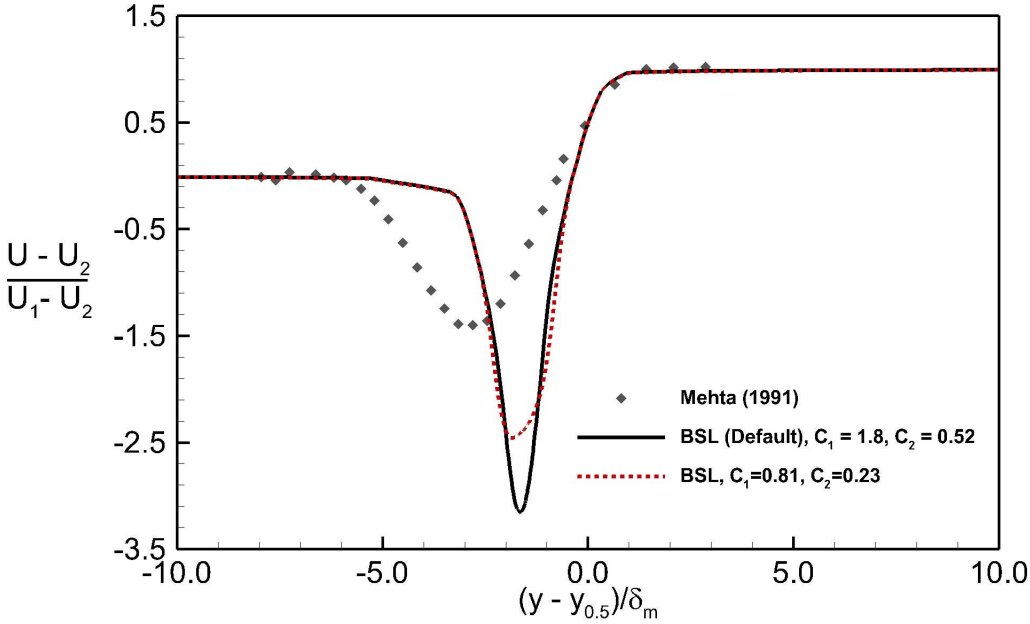

Figure 4.26: Splitter-plate wake at $x = 0.038L_{sp}$

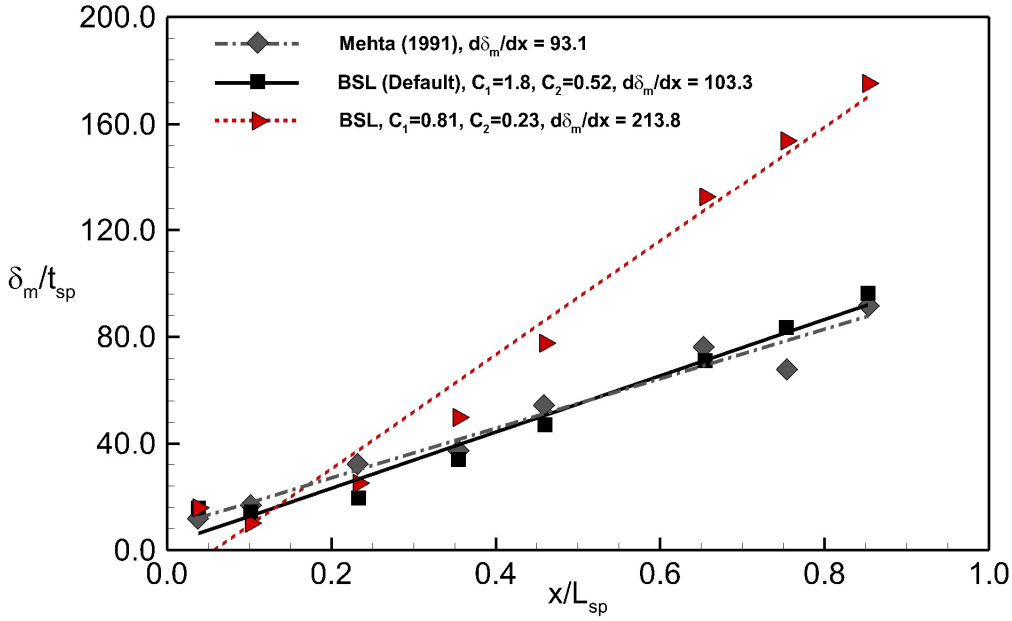

Figure 4.27: Splitter-plate mixing-layer thickness

Accordingly, a cascade test section was designed and manufactured for the high-speed wind-tunnel at Carleton University to study the strut and guide-vane-row interaction. This work was completed in parallel with the low-speed work of the preceding chapters, which sought to develop a test matrix of promising strut positions that could be studied experimentally at relevant subsonic Mach numbers. Experimentation with this setup could not be included in the timeline of the present thesis. The next chapter discusses the Pratt and Whitney Canada High-Speed Wind-Tunnel at Carleton University and the design and manufacturing of the cascade test section.

Chapter 5

Design of a Rectilinear Test Section for Compressible-Flow Testing of a Strut and a Row of Guide Vanes in Tandem Configuration

5.1 Introduction

This chapter outlines the design and manufacturing of a new rectilinear test-section assembly for the existing High-Speed Blow-Down Wind Tunnel at Carleton University. This new test section is intended to investigate any effects of compressibility on the strut/guide-vane aerodynamic interaction in the tandem configuration at high subsonic Mach numbers.

5.2 High-Speed Blow-Down Wind Tunnel

The Pratt and Whitney Canada High-Speed Blow-Down Wind Tunnel at Carleton University is illustrated in Figure 5.1. The facility consists of four interconnected compressed-air storage tanks of 26 m^3 total internal volume, a flow control valve, and an air-supply duct.

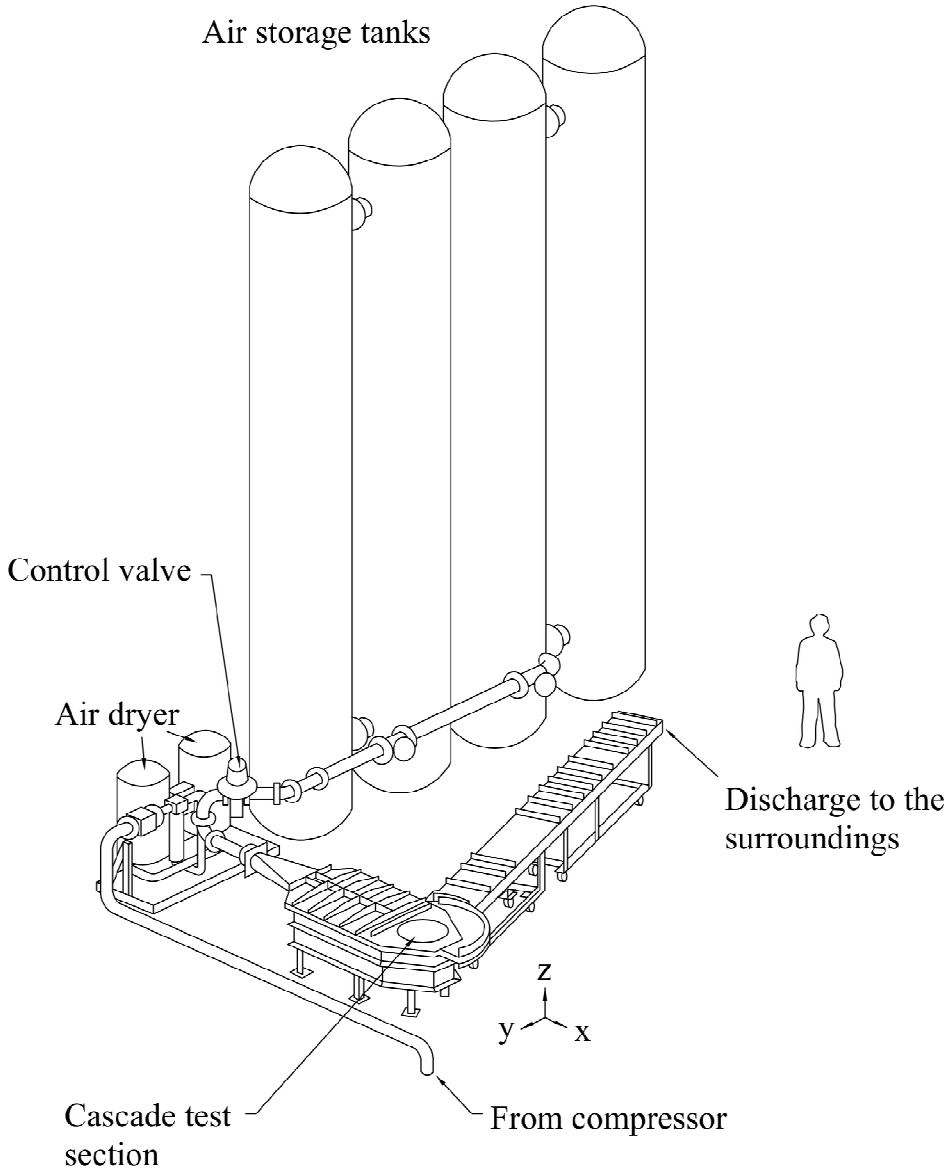

Figure 5.1: Carleton's Pratt and Whitney Canada high-speed wind tunnel (adapted from Kibsey, 2015)

The air-supply duct feeds airflow discharging from the storage tanks to a test section through the flow-control valve that regulates the mass flow rate through the system with the goal of maintaining a constant Mach number at the inlet to the test section over a finite duration. The test section (Fig. 5.2) is designed specifically for a rectilinear cascade of airfoils for an incoming flow with a Mach number range of 0.3 to 0.5 (Corriveau, 2005; Jouini, 2000). A metal turbulence screen is installed upstream of the test-section inlet to enhance flow uniformity and turbulence characteristics. The sidewalls of the flow-path leading up to the cascade are adjustable to accommodate cascades of different pitchwise widths and testing different incidence angles while maintaining constant stagger angle. The sidewalls are intended to be aligned with the inlet flow direction and butt up against the two ends of the cascade to ensure all of the airflow passes through the cascade. The cascade is mounted on a steel baseplate that resides in a recess on a rotatable turntable that allows for varying incidence angles. The test section has a steel top cover with a round opening for a removeable plexiglass window that allows access to the cascade.

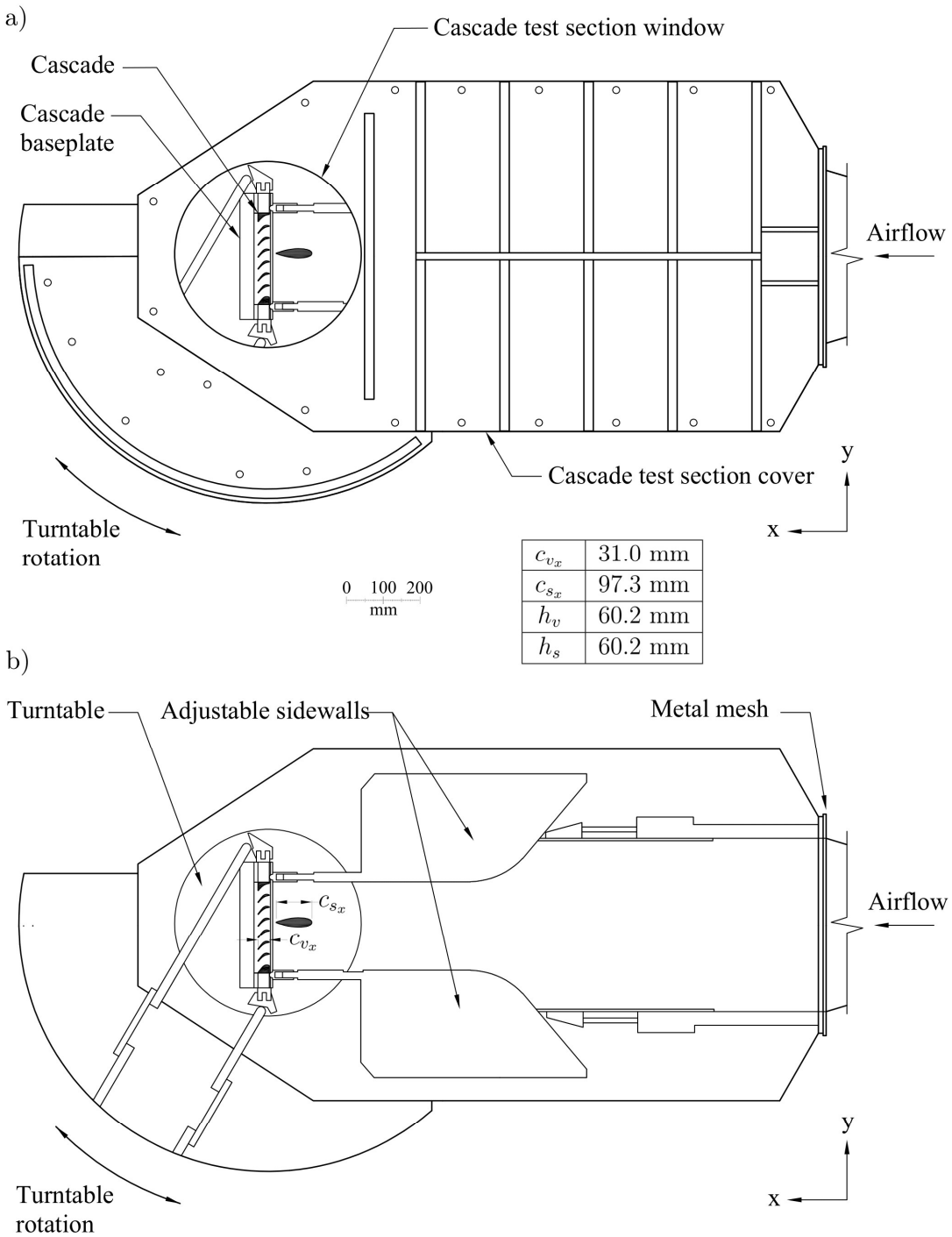

Figure 5.2: Cascade test section a) with top cover and b) without top cover

5.3 Cascade Test Section for a Strut and a Row of Guide-Vanes in Tandem Configuration

A test-section assembly was designed and manufactured to allow for the positioning of a strut upstream of the existing cascade location. The design intent was to allow for adjustable positioning of the strut in the pitchwise and streamwise directions and for the setup to be easily accessible to minimize reconfiguration times between wind-tunnel runs. The original test-section design did not permit quick access to the cascade as it required unbolting and removing the entire top cover plate with a shop crane. The new test-section assembly as shown in Figure 5.3, aimed to address this by permitting direct access to the cascade (Tag 12) and strut (Tag 13) through openings in the plexiglass window (Tag 10). During wind-tunnel operation, these openings are sealed with two flanged aluminum inserts referred to as the cascade cover (Tag 7) and strut endwall (Tag 8), which are bolted directly to the plexiglass window. For added safety, two aluminum angles (Tag 2) span across the cascade cover and strut endwall to constrain their vertical movement during pressurization of the test-section.

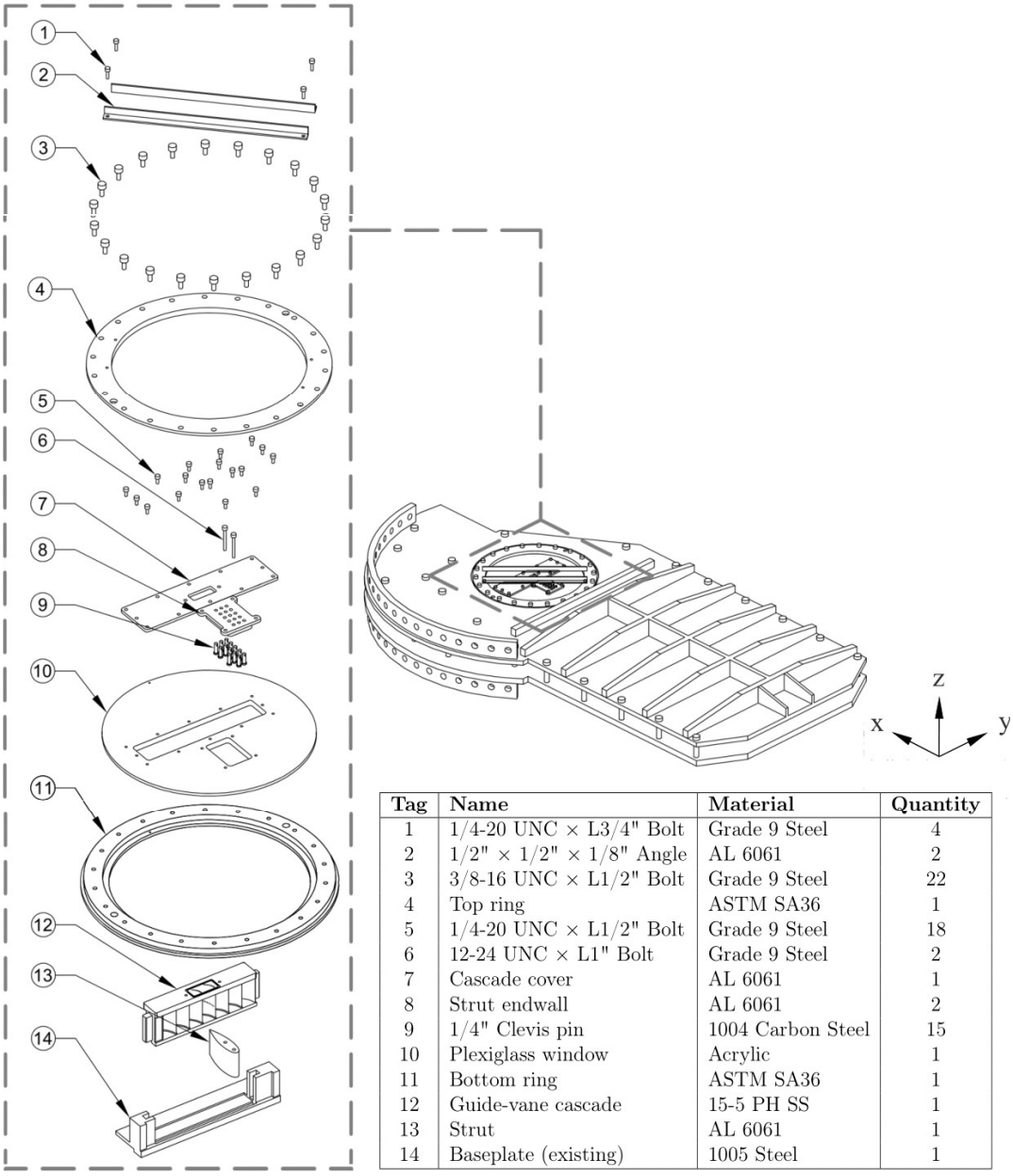

Tag	Name	Material	Quantity
1	1/4-20 UNC × L3/4" Bolt	Grade 9 Steel	4
2	1/2" × 1/2" × 1/8" Angle	AL 6061	2
3	3/8-16 UNC × L1/2" Bolt	Grade 9 Steel	22
4	Top ring	ASTM SA36	1
5	1/4-20 UNC × L1/2" Bolt	Grade 9 Steel	18
6	12-24 UNC × L1" Bolt	Grade 9 Steel	2
7	Cascade cover	AL 6061	1
8	Strut endwall	AL 6061	2
9	1/4" Clevis pin	1004 Carbon Steel	15
10	Plexiglass window	Acrylic	1
11	Bottom ring	ASTM SA36	1
12	Guide-vane cascade	15-5 PH SS	1
13	Strut	AL 6061	1
14	Baseplate (existing)	1005 Steel	1

Figure 5.3: High-speed wind-tunnel cascade test-section assembly

As shown in Figure 5.4, the strut is bolted to the strut endwall, of which there are two variations with different hole patterns to allow for fifty unique strut positions: ten axial positions in increments of $c_{v_x}/4$ and five pitchwise positions in increments of $s/5$. During wind-tunnel operation, the unused holes in the strut endwall are plugged with clevis pins. The cascade cover is positioned over the cascade and has a recessed underside that houses the cascade endwall. As shown in Figure 5.4, the cascade cover possesses a rectangular opening that allows direct access to the ×8 ports located on the cascade endwall that each serve a specific static pressure tap located on either the suction or pressure surface of the two middle guide-vanes. The tap locations are positioned along the streamwise direction at midspan and are staggered one tap diameter in the spanwise direction.

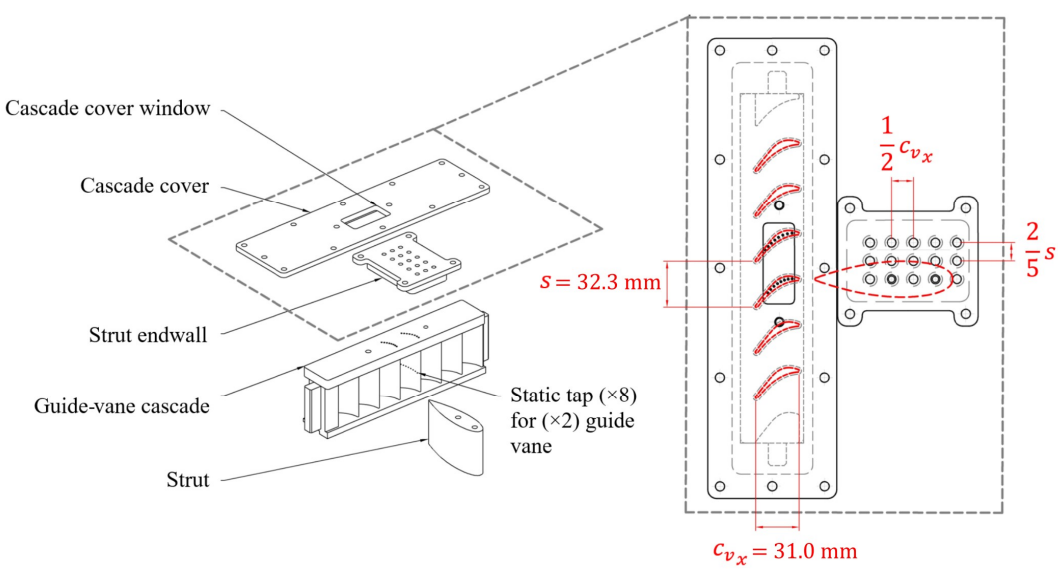

Figure 5.4: High-speed cascade configuration and instrumentation details

Previous cascade designs for this facility consisted of manufacturing each individual blade and a portion of its accompanying endwall in one segment using conventional milling, drilling, cutting methods and then mounting each blade onto a baseplate. This type of design is labour intensive especially when static taps are required on the blade surfaces. To minimize the manufacturing effort, a new cascade consisting of a row of six airfoils modelled after Vane Geometry 3 (see Section 4.1.1) was manufactured out of 15-5 PH Stainless Steel using an additive manufacturing process. A summary of the additive manufacturing process and the material selection for the present cascade are presented in Appendix K.

5.4 Structural Analysis

To verify the structural integrity of the new test section, particularly the plexiglass window and guide-vane cascade, a static structural finite element analysis (FEA) was performed using ANSYS Mechanical APDL (version 19.2) based on a conservative estimate of the aerodynamic and static loads anticipated during wind-tunnel operation. Figures 5.5 and 5.6 present the applied loads and constraints, respectively, for the computational model used in the structural analysis. Table 5.1 presents the mechanical properties of the materials used in the structural analysis and Table 5.2 presents the specifics of the computational grid for each component. The grid consists of approximately 1.1×10^6 tetrahedral elements and 5.0×10^4 hexahedral elements, the latter of which were applied only to the guide-vane cascade. Based on a grid sensitivity analysis of the maximum Von Mises stress and deformation, a global element size of 2mm was selected for all components with refinement applied to the trailing edges of the guide-vanes and strut as well as all bolt hole openings

in the plexiglass window, strut endwall, cascade cover, strut and guide-vane cascade. As shown in Figure 5.5, the red regions denote the surfaces which are exposed to the high-pressure air stream. The pressure magnitude acting on these surfaces is set to a stagnation pressure of 293,850 Pa which is produced by the shock wave that forms when the fully pressurized tanks in the high-speed wind-tunnel begin to discharge. The top face of the plexiglass window is subjected to ambient pressure of 101,000 Pa as denoted by the green region, and the blue region corresponds to a total vane loading, F_{total}, of 752 N. The stagnation pressure and vane loading calculations are presented in Appendix J. As shown in Figure 5.6, the plexiglass window is constrained along its perimeter faces only in the z-direction, which allows these faces to pull inwards as the plexiglass window deflects upwards from the pressurization of the test section. The strut is supported by the wind-tunnel floor as a frictionless support, which allows lifting of the strut from the steel turntable base due to the upward deflection of the plexiglass window. The existing baseplate shown in magenta colour is fully recessed into the wind-tunnel floor and is modelled as a rigid body that is constrained in all directions. The cascade cover and strut endwall are partially constrained in the z-direction by the aluminum angles which are modelled as elastic supports shown in orange colour. The contact surface pairs between the various components are illustrated in Figure 5.7 and are treated as a combination of frictional contacts with a friction coefficient of $\mu = 0.2$ and bonded contacts meant to represent all bolted connections between components.

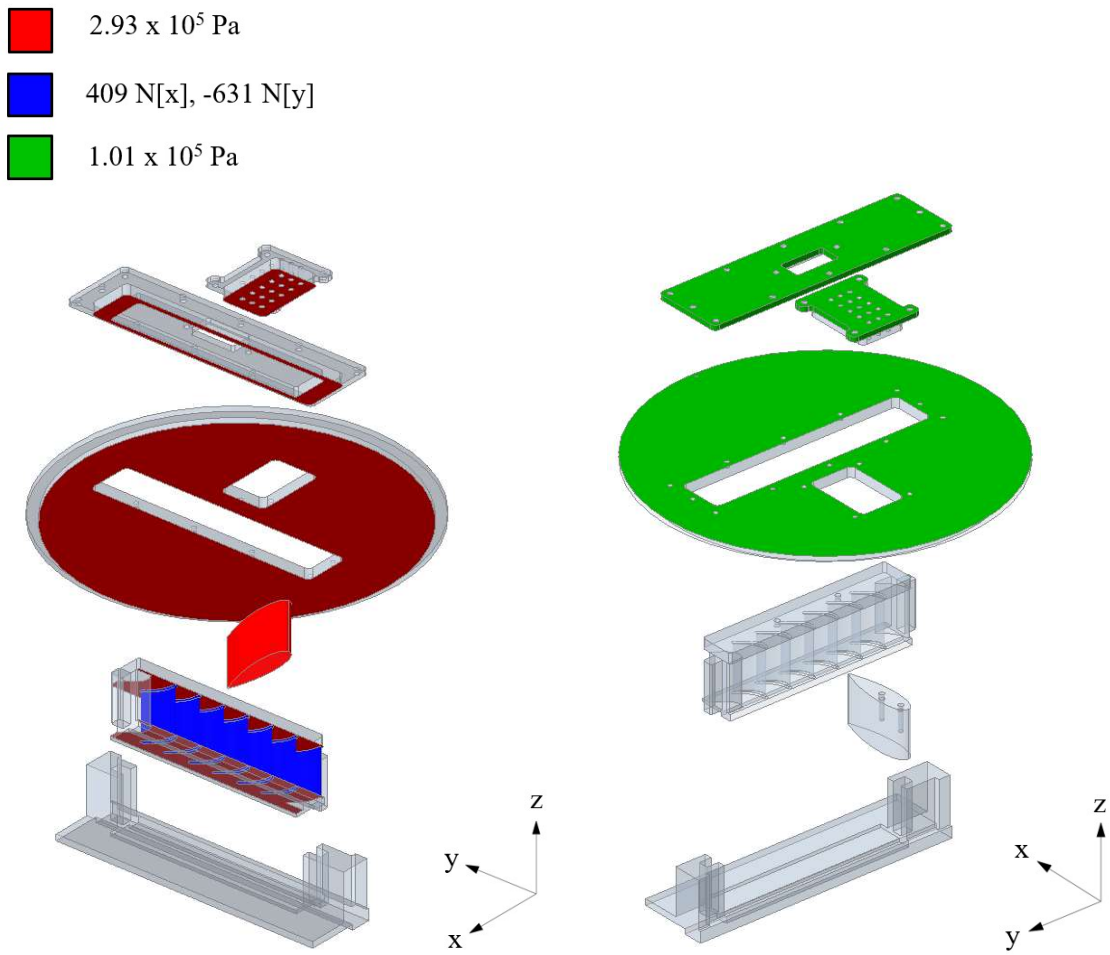

(a) Looking Up (b) Looking Down

Figure 5.5: Applied loads for the FEA computational model of the test-section assembly

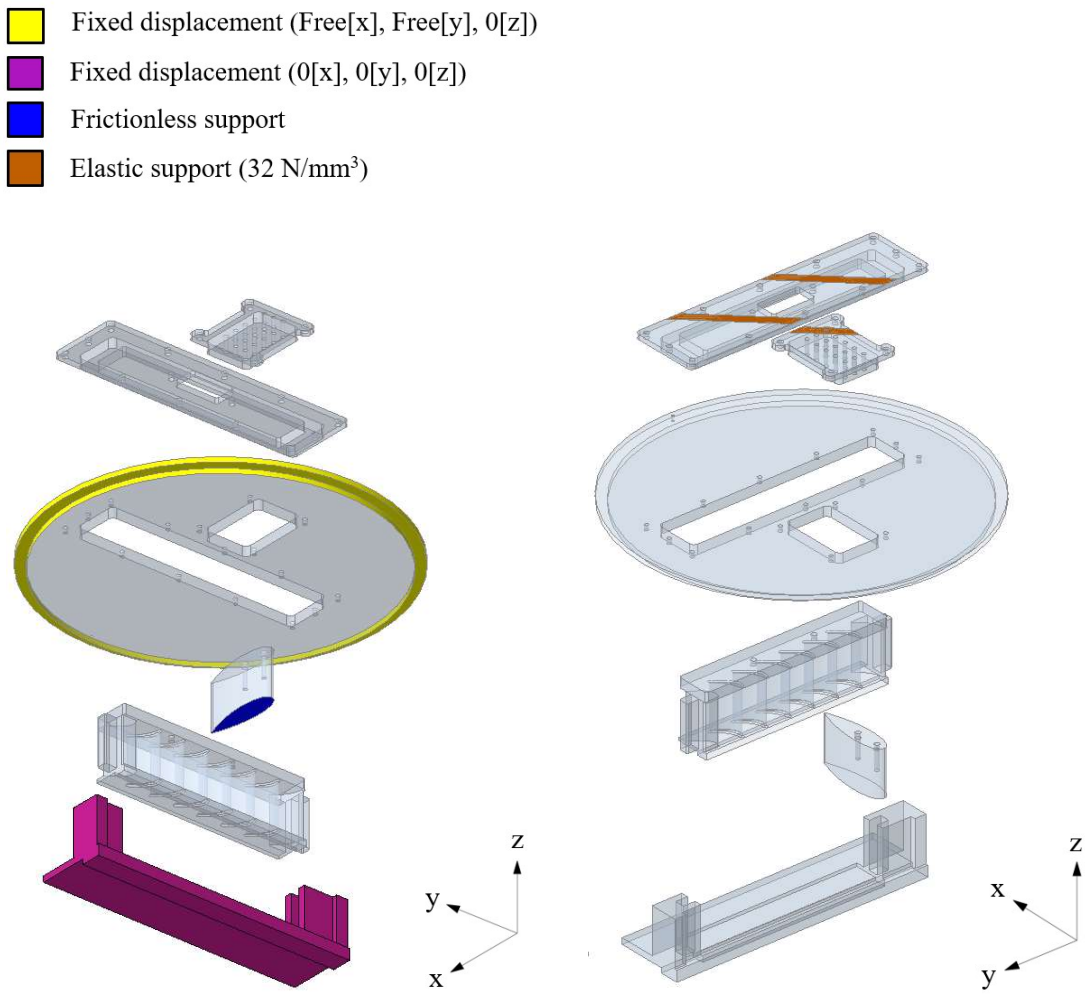

(a) Looking up

(b) Looking down

Figure 5.6: Boundary displacement constraints for the FEA computational model of the test-section assembly

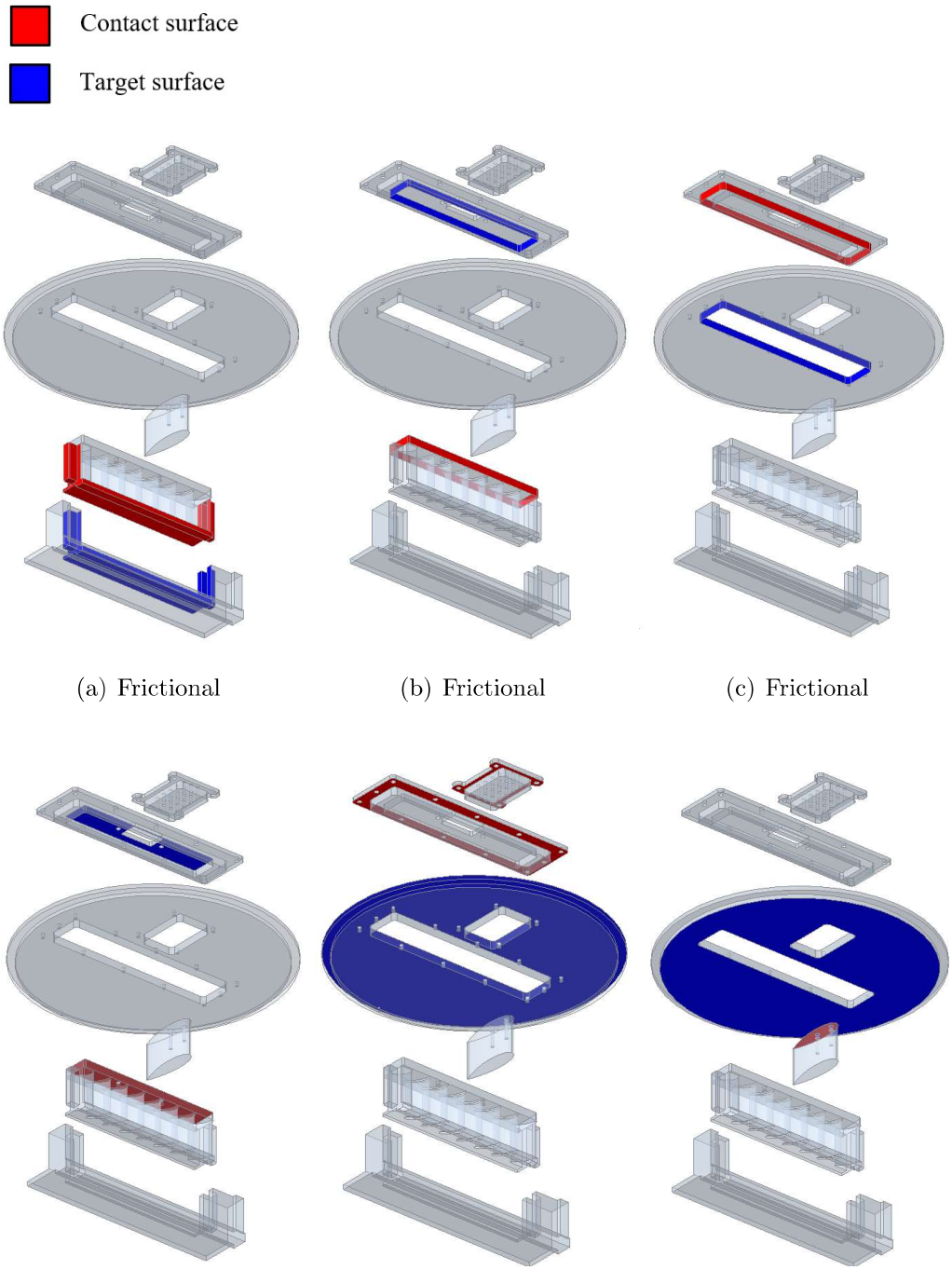

(a) Frictional (b) Frictional (c) Frictional

(d) Bonded (e) Bonded (f) Bonded

Figure 5.7: Contact surface pairs for the FEA computational model of the test-section assembly

Table 5.1: Mechanical properties of the materials in the test-section assembly

	15-5PH S.S.	Mild Steel	AL 6061	PMMA
Density (kg/m^3)	7800	7850	2700	1180
Tensile Yield Strength (MPa)	950	350.0	276	62.4
Compressive Yield Strength (MPa)	950	350.0	276	62.4
Young's Modulus (GPa)	196	200.0	68.9	2.7
Poisson's Ratio	0.30	0.30	0.33	0.40

Table 5.2: Parameters of the computational grid

	Element size (mm) min/max	Spatial growth rate (%) min/max
Cascade	0.2/2.8	0/15
Strut	0.7/5.0	0/15
Cascade Cover	0.7/5.0	0/15
Strut Endwall	0.7/4.5	0/15
Plexiglass Window	0.7/4.7	0/15

5.5 Computational Results

Figures 5.8, 5.9, 5.10 and 5.11 present the Von Mises stress distribution of the guide-vane cascade, strut, cascade cover/strut endwall and plexiglass window, respectively. Table 5.3 presents a summary of the structural analysis results, which demonstrate the design to be structurally sound, with stress levels well within safety limits, and with elastic deformation levels that do not adversely affect the intended geometry of the assembly. The medium carbon steel fasteners and surrounding Mild Steel components not included in the FEA computational model are not presented as these components are subjected to stress levels that are well within their elastic limits.

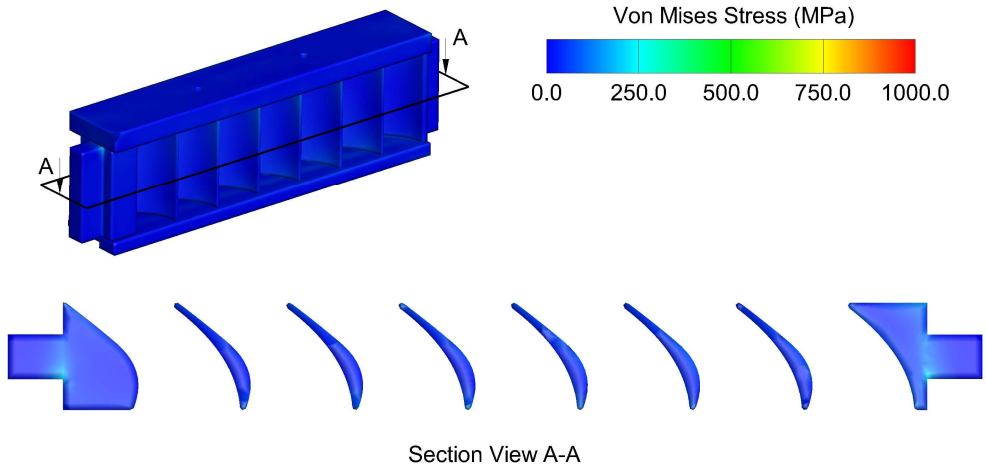

Figure 5.8: Von Mises stress distribution in 15-5PH S.S. guide-vane cascade

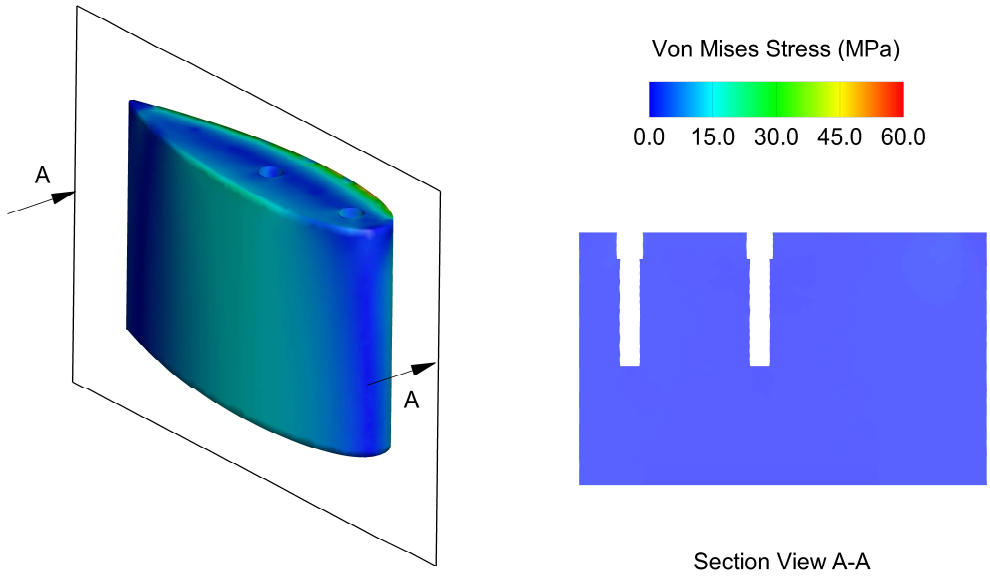

Figure 5.9: Von Mises stress distribution in Aluminum 6061 strut

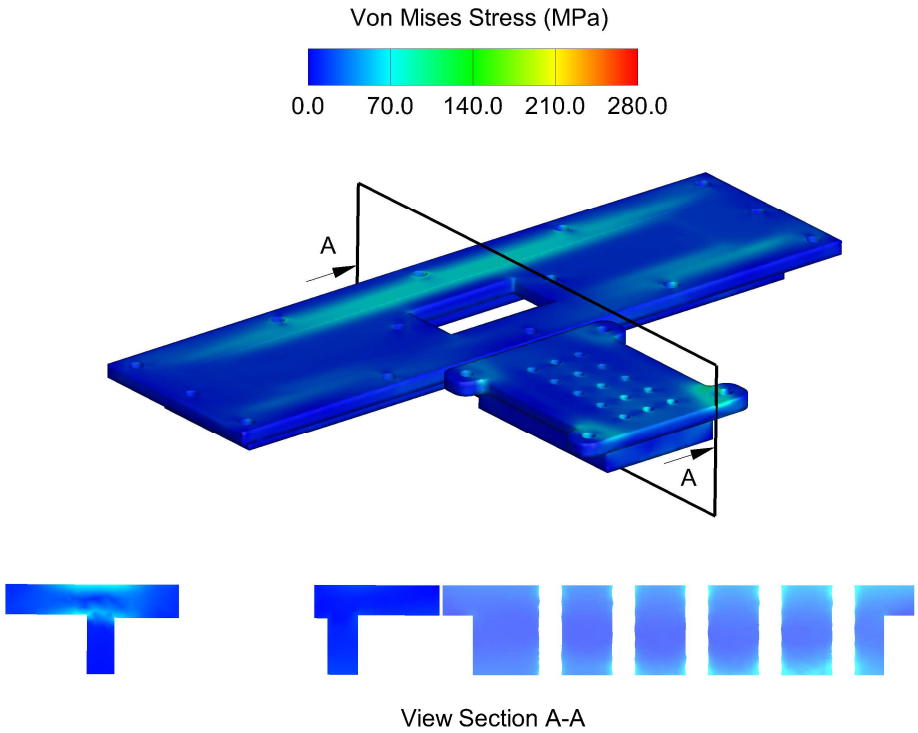

Figure 5.10: Von Mises stress distribution in Aluminum 6061 cascade cover and strut endwall

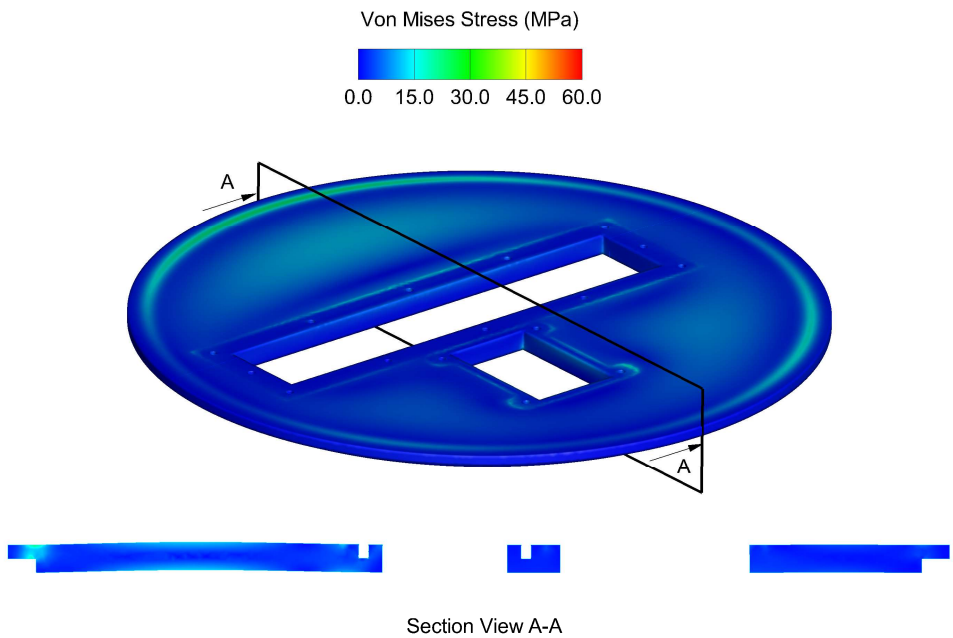

Figure 5.11: Von Mises distribution in the plexiglass window

Table 5.3: Summary of structural analysis results for cascade

Component	Max Deformation (mm)	Max Deformation (% of c_{v_x})	Max. Stress (MPa)	Min. Safety Factor
Cascade	0.3	0.97	193.8	4.9
Strut	5.5×10^{-5}	0.00	52.0	5.4
Cascade Cover	0.4	1.30	73.4	3.8
Strut Endwall	0.2	0.65	83.6	3.4
Plexiglass Window	1.4	4.52	19.7	3.2

Chapter 6

Conclusions and Recommendations for Future Work

The present study investigated the aerodynamics of the strut and guide-vane interaction in the ITD by first studying the mass-averaged profile loss and momentum thickness within the wakes of the guide-vanes and strut, respectively, in isolation using numerical solutions of the governing RANS equations with the BSL Reynolds-stress model. The RANS-based BSL Reynolds-stress model was chosen specifically because of its ability to simulate flow near the wall without the use of scalable wall functions. Based on a numerical study that determined the lowest achievable mass-averaged profile loss distribution across a range of incidence angles, a baseline guide-vane geometry was selected out of three guide-vane profiles. A baseline strut geometry was also generated and its aerodynamic performance was analyzed numerically for a freestream with (1) a uniform zero-pressure gradient and (2) a streamwise adverse pressure gradient associated with the diffusion rate in the ITD. It was determined that the presence of an adverse pressure gradient in the freestream had a minimal effect on the strut aerodynamic performance and resulted in less than a 2.5% difference in the momentum thickness of the strut wake when compared to a uniform zero-pressure gradient in the freestream. These results served to justify the ensuing numerical simulations of the strut and guide-vane row

in tandem configuration in the presence of a nominally zero-pressure gradient flow.

The strut and guide-vane row in tandem configuration was numerically simulated with the intent of studying the wake interaction in the context of minimizing the profile losses by positioning the strut at combinations of axial and pitchwise positions relative to the guide-vane row. Through benchmarking the numerical results against experimental data obtained at the low-speed wind-tunnel at Carleton University, it was determined that although the momentum thickness in the wake differed by less than 2%, the RANS-based BSL Reynolds-stress model produced a considerably steeper wake velocity profile for both the strut and nearest guide-vane, and possessed less pitchwise diffusion when compared to the experimental data. This discrepancy motivated a more fundamental study of the RANS-based BSL Reynolds-stress model that involved two benchmarking exercises against published experimental data: (1) a zero-pressure-gradient turbulent boundary layer and (2) a planar turbulent free-shear layer.

In the case of the zero-pressure-gradient turbulent boundary layer, the wall-normal variation of the terms of the Reynolds-stress transport equation were compared against published DNS data, and discrepancies were observed in the terms responsible for dissipating or redistributing turbulence kinetic energy in the near-wall region. This included the inability of the RANS-based BSL Reynolds-stress model to recreate the anisotropic dissipation near the wall and the greater influence of the pressure-strain rate term in the RANS-based BSL Reynolds-stress model that compensated for the lack of turbulence kinetic energy dissipation produced by the dissipation, viscous diffusion and turbulence diffusion terms when compared to the DNS data. The RANS-based BSL Reynolds-stress model, however, was able to accurately reproduce

the turbulence kinetic production throughout the boundary layer.

In the case of the turbulent free-shear layer, the RANS-based BSL Reynolds-stress model exhibited the same shortcomings as the tandem strut and guide-vane row simulation, specifically, a steeper wake velocity profile and less viscous diffusion in the pitchwise direction. However, the mixing-layer growth rate downstream of the splitter-plate was accurate to within 11% of the experimental data of Mehta (1991). It was determined that although the RANS-based BSL Reynolds-stress model in its present form can be used to approximate certain parameters such as the momentum thickness in the wake or the mixing-layer growth rate, its prediction accuracy is insufficient for capturing the particular flow physics in the turbulent free-shear layer and thus is limited in its ability to optimize the relative axial and pitchwise positioning of the strut and guide-vane row to achieve the best aerodynamic performance.

As a follow-up to the present study, a more thorough calibration process of the RANS-based BSL Reynolds-stress model can be undertaken to try to reduce these shortcomings. In the meantime, a heavier reliance on wind-tunnel experiments is necessary which motivated the design and manufacturing of a new rectilinear test section to study the aerodynamic performance on the relative positioning of a strut and guide-vane row at high subsonic Mach flows. The test section was designed to be compatible with the existing high-speed wind-tunnel facility at Carleton University. The structural integrity of the test section under the anticipated aerodynamic loads were confirmed through a structural analysis and the test section has since been manufactured and in-stalled in the facility. Commissioning of the installation followed by experiments on the strut-guide-vane aerodynamic interactions in compressible flow regimes constitute the near-future work that can readily build upon the present study.

References

Abramovich, G.N. (1963) “The Theory of Turbulent Jets,” *M.I.T.* Press, 1963.

Abu-Ghannam, B.J., Shaw, R. (1980) “Natural Transition of Boundary Layers - The Effects of Turbulence, Pressure Gradient and Flow History,” *J. Mech. Eng. Sci.,* 22, pp. 213-228.

Afkhami S., Dabiri, M., Alavi, S.H., Bjork, T., Salminen A. (2019), "Fatigue characteristics of Steels Manufactured by Selective Laser Melting," *International Journal of Fatigue 122(2019),* pp. 72-83.

Ali, H., Ma, L., Ghadbeigi, H., Mumtaz, K. (2017), "In situ Residual Stress Reduction, Martensitic Decompisition and Mechanical Properties Enhancement Through High Temperature Powder Bed Pre-Heating of Selective Laser Melted Ti6Al4V," *Material Science Engineering A 2017, 695.* pp 211-220.

Axelsson L.U., Arroyo Osso, C., Cadrecha, D., Johansson, T.G. (2007) “Design, Performance Evaluation and Endwall Flow Structure Investigation of an S-shaped Intermediate Turbine Duct,” *ASME GT2007-27650.*

ANSYS, (2006) “ANSYS CFX-Solver Theory Guide,” *ANSYS, Inc.,* 275 Technology Drive, Canonsburg, PA.

Azih, C., Brinkerhoff, J. and Yaras, M. (2012) “Direct Numerical Simulation of Convective Heat Transfer in a Zero-Pressure-Gradient Boundary Layer with Supercritical Water,” *Journal of Thermal Science,* Vol. 21, no. 1, pp. 49–59.

Bell, J.H., Mehta, R.D. (1990) “Development of a Two-Stream Mixing-layer from Tripped and Untripped Boundary Layers,” *AIAA Journal,* Vol. 28, pp. 2034-2042.

Benner (2003) “The Influence of Leading-Edge Geometry on Profile and Secondary Losses in Turbine Cascades,” *PhD thesis*, Carleton University. Ottawa, Canada

Birch, S.F., Eggers, J.M. (1972) “A Critical Review of the Experimental Data for Developed Free Turbulent Shear Layers,” *Free Turbulent Shear Flows,* Vol. I., NASA SP-321, pp. 11-40.

Biswas, R. and Strawn, R.C. (1998) “Tetrahedral and Hexahedral Mesh Adaption for CFX Problems,” *Applied Numerical Mathematics,* 26(1-2), pp. 135-151.

Blinn, B., Klein, M., Glabner, C., Smaga, M., Aurich, J.C., Beck, T. (2018), "An Investigation of the Microstructure and Fatigue Behaviour of Additively Manufactured AISI 316L Stainless Steel with Regard to the Influence of Heat Treatment," *Metals 2018, 8, 220* pp. 1-23.

Bons, J.P. (2010), "A Review of Surface Roughness Effects in Gas Turbines," *Journal of Turbomachinery, Vol 132, 021004,* pp 1-16.

Brookfield, J.M., Waitz, L.A., Sell, J. (1996) “Wake Decay: Effect of Freestream Swirl,” *ASME Paper 96-GT-495, V001T03A097,* pp 1-13.

Brown, G., Roshko, A. (1974) “On Density Effects and Large Structure in Turbulent Mixing-layers,” *Journal of Fluid Mechanics,* Vol. 64, pp. 775-816.

Carter, L.N., Attallah, M.M., Reed, R.C. (2012)," Laser Powder Bed Fabrication of Nickel-Base Superalloys: Influence of Parameters; Characterisation, Quantification and Mitigation of Cracking," *Superalloys 2012, ed: John Wiley and Sons, Inc., 2012,* pp. 577-586.

Chan, K.S., Koike, M., Mason, R.L., Okabe, T. (2013), "Fatigue Life of Titanium Alloys Fabricated by Additive Layer Manufacturing Techniques for Dental Implants," *Metallurgical and Materials Transactions A, Volume 44A,* pp. 1010-1022.

Corriveau, D. (2005) “Influence of Loading Distribution on the Performance of High Pressure Turbine Blades,” *PhD thesis*, Carleton University. Ottawa, Canada

Croccolo, D., De Agostinis, M., Fini, S., Olmi, G., Bogojevic, N., Ciric-Kostic, S. (2017), "Effects of Build Orientation and Thickness of Allowance on the Fatigue Behaviour of 15-5 PH Stainless Steel Manufactured by DMLS," *Fatigue Fract Eng Mater Struct.,* pp. 900-916.

Denton, J.D. (1993) “Loss Mechanisms in Turbomachines,” *ASME Journal of Turbomachinery,* 115, pp. 621-656.

Denton, J.D., Xu, L. (1990) “The Trailing Edge Loss of Transonic Turbine-blades,” *ASME Journal of Turbomachinery,* 112, pp. 277-285.

Dominy, R.G., Kirkham, D.A. (1996) “The Influence of Blade Wakes on the Performance of Inter-turbine Diffusers,” *ASME J Turbomach,* 118, pp. 347-352.

Dominy, R.G., Kirkham, D.A., Smith, A.D. (1998) “Flow Development Through Inter-turbine Diffusers,” *ASME J Turbomach,* 120, pp. 298-304.

Edwards, P., O’Conner, A., Ramulu, M. (2013), "Electron Beam Additive Manufacturing of Titanium Components: Properties and Performance," *Journal of Manufacturing Science and Engineering, Vol. 135, 061016,* pp. 1-7.

Edwards, P., Ramulu, M. (2014), "Fatigue Performance Evaluation of Selective Laser Melted Ti-6Al-4V," *Materials Science and Engineering A 598,* pp. 327-337.

Emmons, H.W. (1951) “The Laminar-Turbulent Transition in a Boundary Layer - Part I,” *J. Aero, Sci.,* Vol. 18, pp. 490-498.

Fayazfar, H., Salarian, M., Rogalsky, A., Sarker, D., Russo, P., Paserin, V., Toyserkani, E. (2018), "A Critical Review of Powder-Based Additive Manufacturing of Ferrous Alloys: Process Parameters, Microstructure and Mechanical Properties," *Materials and Design 144,* pp. 98-128.

Ferziger, J.H., Peric, M. (2002) “Computational Methods for Fluid Dynamics,” *Springer-Verlag Berlin Heidelberg.*

Gaster, M. (1969) “The Structure and Behaviour of Laminar Separation Bubbles,” *ARC RM 3595.*

Gibson, I., Rosen, D., Stucker, B. (2015) "Additive Manufacturing Technologies: 3D Printing, Rapid Prototyping, and Direct Digital Manufacturing," *2nd Edition. New York: Springer.*

Gokuldoss, P.K., Kolla, S., Eckert, J. (2017) "Additive Manufacturing Processes: Selective Laser Melting, Electron Beam Melting and Binder Jetting - Selection Guidelines," *Materials 3017, 10, 672,* pp. 1-12.

Gong, H., Rafi, H.K., Nadimpalli, K. (2013) "Defect Morphology of Ti-6Al-4V Parts Fabricated by Selective Laser Melting and Electron Beam Melting," pp. 440-453.

Gong, H., Rafi, H.K., Gu, H., Janaki Ram, G.D., Starr, T., Stucker, B. (2015) "Influence of defects on Mechanical Properties of Ti-6Al-4V Components Produced by Selective Laser Melting and Electron Beam Melting," *Mater. Des.* pp. 545-554.

Gortler, H. (1942) “Calculation of Free Turbulence Tasks Based on a New Approach,” *Journal of Applied Mathematics and Mechanics,* Vol 22, No. 5, pp. 244-254.

Gottlich, E., Marn, A., Malzacher, F.J., Schennach, O., Heitmeir, F. (2007) “Experimental Investigation of the Flow Through an Aggressive Intermediate Turbine Duct Downstream of a Transonic Turbine Stage,” *7th European Conference on Turbomachinery Fluid Dynamics and Thermodynamics,* pp. 383-394.

Gottlich, E. (2011) “Research on the Aerodynamics of Intermediate Turbine Diffusers,” *Progress in Aerospace Sciences,* pp. 249-279.

Goobie, S. M. (1989) “A Test Section for Investigating the Off-Design Performance of Planar Cascades,” MASc thesis, Carleton University, Ottawa, Canada.

Gunther, J., Krewerth, D., Lippmann, T., Leuders, S., Troster, T., Weidner, A., Biermann, H., Niendorf, T. (2017), "Fatigue Life of Additively Manufactured Ti-6Al-4V in the Very High Cycle Fatigue Regime," *International Journal of Fatigue 94,* pp. 236-245.

Gu, D. (2015), "Laser Additive Manufacturing of High-Performance Materials," *Springer,* pp. 1-311.

Gu, H., Gong, H., Pal, D., Rafi, K, Starr, T., Stucker, B. (2013), "Influences of Energy Density on Porosity and Microstructure of Selective Laser Melted 17-4PH Stainless Steel," *24th Annual International Solid Freeform Fabrication Symposium,* pp. 475-489.

Hanjalic, K., Launder, B. (2011) "Modelling Turbulence in Engineering and the Environment: Second-Moment Routes to Closure," Cambridge University Press.

Herzog, D., Seyda, V., Wycisk, E., Emmelmann, C. (2016), "Additive Manufacturing of Metals," *Acta Materialia 117,* pp. 371-392.

Hourmouziadis, J. (1989) "Aerodynamic Design of Low Pressure Turbines," *AGARD-LS-167.*

Hrabe, T., Gnaupel-Herold, T., Quinn, T. (2017), "Fatigue Properties of a Titanium Alloy (Ti-6Al-4V) Fabricated via Electron Beam Melting (EBM): Effects of Internal Defects and Residual Stress," *International Journal of Fatigue 94,* pp. 202-210.

Jouini, D.B.M. (2000) "Experimental Investigation of Two Transonic Linear Turbine Cascades at Off-Design Conditions," *PhD thesis*, Carleton University. Ottawa, Canada.

Kacker, S.C., Okapuu, U. (1982) "A Mean Line Prediction Method for Axial Flow Turbine Efficiency," *ASME Journal of Engineering for Gas Turbines and Power*, Vol. 104, pp. 111-119.

Kasperovich, G., Hausmann, J. (2015) "Improvement of Fatigue Resistance and Ductility of Ti-6Al-4V Processed by Selective Laser Melting," *Journal of Materials Processing Technology, vol. 220,* pp. 202-214.

Katz, A. and Sankaran, V. (2011) "Mesh Quality Effects on the Accuracy of CFD Solutions on Unstructured Meshes," *J. Comp. Phys.,* 230(20), pp. 7670-7686.

Kelley Jr., P.F. (2016) "Fatigue Behaviour of Direct Metal Sintered (DMLS) Inconel 718," PhD thesis, Tufts University, pp. 1-125.

Kibsey, M. (2015) “Influence of Mach Number on Profile Loss,” *Master of Applied Science thesis*, Carleton University. Ottawa, Canada.

Kobryn, P.A., Moore, E.H., Semiatin, S.L. (2000), "The Effect of Laser and Traverse Speed on Microstructure, Porosity and Build Height in Laser Deposited Ti-6Al-4V," *Scripta Materialia, vol. 43,* pp. 299-305.

Kruth, J.P., Levy, G., Klocke, F., Childs, T.H.C. (2007), "Consolidation Phenomena in Laser and Powder-Bed Based Layered Manufacturing," *CIRP Annals, vol. 56, Issue 2, 2007,* pp. 730-759.

Kumar, A.Y., Bai, Y., Eklund, A., Williams, C.B. (2018), "The Effects of Hot Isostatic Pressing on Parts Fabricated by Binder Jetting Additive Manufacturing," *Additive Manufacturing 24,* pp. 115-124.

Kumart, D.S., Kumart, K. L. (1980) “Effect of Swirl on Pressure Recovery in Annular Diffusers,” *Journal of Mechanical Engineering Science*, Vol 22, No. 6, pp. 305-313.

Launder, B.E., Reece, G.J., Rodi, W. (1975) "Progress in the Developments of a Reynolds-stress Turbulence Closure," *Journal of Fluid Mechanics,* 68, pp. 537-566.

Leuders, S., Thone, M., Riemer, A., Niendorf, T., Troster, T., Richard, H.A., Maier, H.J. (2013), "On the Mechanical Behaviour of Titanium Alloy TiAl6V4 Manufactured by Selective Laser Melting: Fatigue Resistance and Crack Growth Performance," *International Journal of Fatigue 48,* pp. 300-307.

Leschziner, M. (2015) "Statistical Turbulence Modelling for Fluid Dynamics-Demystified: An Introductory Text for Graduate Engineering Students," *World Scientific.*

Li, C., Liu, J.F., Guo, Y.B. (2016), "Fast Prediction and Validation of Part Distortion in Selective Laser Melting," *43rd Proceedings of the North American Manufacturing Research Institution of SME,* pp. 355-365.

Lohmann, R. P., Markowski, S. J., Brookman, E.T. (1979) "Swirling Flow Through Annular Diffusers with Conical Walls," *ASME Journal of Turbomachinery*, Vol 101, pp. 224-228.

Marn, A., Gottlich, E., Cadrecha, D., Pirker, H.P. (2009) "Shorten the Intermediate Turbine Duct Length by Applying an Integrated Concept," *ASME J Turbomach 131:041014*, pp. 10.

Mee, D.J., Baines, N.C., Oldfield, M.L.G., Dickens, T.E. (1992) "An Examination of the Contributions to a Loss on a Transonic Turbine Cascade," *ASME Journal of Turbomachinery*, Vo. 114, pp. 155-162.

Mehta, R.D. (1991) "Effect of Velocity Ratio on Plane mixing-layer Development: Influence of the Splitter Plate Wake," *Experiments in Fluids*, Vol 10, No. 4, pp. 194–204.

Mercelis, P., Kruth, J.P. (2006), "Residual Stresses in Selective Laser Sintering and Selective Laser Melting," *Rapid Prototyp. J. 12(5),* pp. 254-265.

Miller, R.J., Moss, R.W., Ainsworth, R.W., Harvey, N.W. (2003) “The Development of Turbine Exit Flow in a Swan-necked Inter-stage Diffuser,” *ASME GT2003-38174.*

Miles, J.B., Shih, J.S. (1968) “Similarity Parameter for Two-Stream Turbulent Jet-Mixing Region,” *AIAA Journal*, Vol 6, No. 7, pp. 1429-1430.

Mower, T.M., Long, M.J. (2016), "Mechanical Behaviour of Additive Manufactured, Powder-Bed Laser Fused Materials," *Materials Science and Engineering A651,* pp. 198-213.

Molaei, R., Fatemi, A. (2017), "Fatigue Design with Additive Manufactured Metals: Issues to Consider and Perspective for Future Research," *7th International Conference on Fatigue Design, Procedia Engineering 213,* pp. 5-16.

Mugwagwa, L., Dimitrov, D., Matope, S., Yadroitsev, I. (2018), "Influence of Process Parameters on Residual Stress Related Distortions in Selective Laser Melting," *15th Global Conference on Sustainable Manufacturing,* pp. 92-99.

Nikuradse, J. (1933), "Laws for Flows in Rough Pipes," *VDI-Forchungsheft 361, Series B, Vol 4 (English Translation NACA TM 1292, 1950).*

Norris, G., Dominy, R.G., Smith, A.D. (1998) “Strut Influences Within a Diffusing Annular S-shaped Duct,” *ASME 98-GT-425.*

Oster, D., Wygnanski, I. (1982) “The Forced Mixing-layer Between Parallel Streams,” *Journal of Fluid Mechanics*, Vol. 123, pp 91-130.

Papamoschou, D., Roshko, A. (1988) “The Compressible Turbulent Shear Layer: An Experimental Study,” *Journal of Fluid Mechanics,* Vol. 197, pp. 453-477.

Pirozzoli S., Bernardini, M., Grasso, F. (2010) “Direct Numerical Simulation of Transonic Shock/Boundary Layer Interaction Under Conditions of Incipient Separation,” *Journal of Fluid Mechanics,* Vol. 657, pp. 361-393.

Pope, S.B. (2000) “Turbulent Flows,” *Cambridge University Press.*

Pritchard, L.J. (1985), “An Eleven Parameter Axial Turbine Airfoil Geometry Model,” *ASME Paper,* 85-GT-219, pp. 1-10.

Riemer, A., Leuders, S., Thone, M., Richard, H.A., Troster, T., Niendorf, T. (2014), "On the Fatigue Crack Growth Behaviour in 316L Stainless Steel Manufactued by Selective Laser Melting," *Engineering Fracture Mechanics 120,* pp. 15-25.

Richardson, L.F. (1910), "The Approximate Arithmetical Solution by Finite Differences of Physical Problems Involving Differential Equations with an Application to the Stresses In a Masonry Dam," *Transactions of the Royal Society of London,* Ser. A, 210, pp. 307-357.

Roache, P.J. (1996), "Perspective: A Method for Uniform Reporting of Grid Refinement Studies," *ASME Journal of Fluids Engineering,* Vol. 116, pp. 405-413.

Rodi, W. (1972) "The Prediction of Free Turbulent Boundary Layers by Use of a Two-Equation Model of Turbulence," *PhD thesis,* University of London.

Rhie, C.M., Chow, W.L. (1983) “Numerical Study of the Turbulent Flow Past an Airfoil with Trailing Edge Seperation,” *AIAA Journal,* 21(11), pp. 1525-1532.

Sabin, C.M. (1965) “An Analytical and Experimental Study of the Plane, Incompressible, Turbulent Free-Shear Layer with Arbitrary Velocity Ratio and Pressure Gradient,” *Transactions of the ASME, Series D: Journal of Basic Engineering,* Vol. 87, pp. 421-428.

Saddoughi, S.G., Veervalli, S.V. (1994) “Local Isotropy in Turbulent Boundary Layers at High Reynolds Number,” *J. Fluid Mech.* Vol. 268, pp. 333-372.

Sames, W.J., List, F.A., Pannala, S., Dehoff, R.R., Babu, S.S. (2016) "The Metallurgy and Processing Science of Metal Additive Manufacturing," *International Materials Reviews, Volume 61,* pp. 1-78.

Samimy, M., Elliot, G. (1990) “Effects of Compressibility on the Characteristics of Free Shear Layers,” *AIAA Journal*, Vol 28, No.3, pp. 439-445.

Shrestha, R., Simsiriwong, J., Shamsaei, N. (2019) "Fatigue Behabiour of Additive Manufacturing 316L Stainless Steel Parts: Effects of Layer Orientation and Surface Roughness," *Additive Manufacturing 28,* pp. 23-38.

Slotwinski, J.A., Garboczi, E.J., Hebenstreit, K.M. (2014) "Porosity Measurements and Analysis for Metal Additive Manufacturing Process Control," *Journal of Research of the National Insitute of Standards and Technology, Volume 119* pp. 494-528.

Sooriyakumaran, C. (2014) “Experimental Study of Profile Losses in Three Transonic Turbine Cascades,” *Master of Applied Science thesis*, Carleton University.

Spalart, P.R. (1988) "Direct Numerical Simulation of a Turbulent Boundary Layer up to R=1410," *Journal of Fluid Mechanics*, Vol.187 pp.61-98.

Spencer, B.W., Jones, B.G. (1971) “Statistical Investigation of Pressure and Velocity Fields in the Turbulent Two-Stream mixing-layer,” *AIAA Paper*, 71-0613.

Speziale, C.G., Sarker, S., Gatski, T.B. (1991) “Modeling the Pressure-strain Correlation of Turbulence: An Invariant Dynamical Systems Approach,” *Journal of Fluid Mechanics*, 227, pp 245-273.

Spierings, A.B., Starr, T.L., Wegener, K. (2013), "Fatigue Performance of Additive Manufactured Metallic Parts," *Rapid Prototyping Journal, Vol. 19 Issue:2,* pp. 88-94.

Srivatsan, T.S. and Sudarshan, T.S. (2015), "Additive Manufacturing: Innovations, Advances, and Applications," *New York, New York, CRC Press.*

Stoffregen, H.A., Butterwick, K.A., Abele, E. (2014), "Fatigue Analysis in Selective Laser Melting: Review and Investigation of Thin-Walled Actuator Housings," *Proceedings of the 25th Solid Freeform Fabrication Symposium, Austin,* pp. 635-650.

Stecker S., Lachenberg, K.W, Wang, H., Salo, R.C. (2006), "Advanced Electron Beam Free Form Fabrication Methods and Technology," *Proceedings of the 25th Solid Freeform Fabrication Symposium, Austin,* pp. 635-650.

Svensson, M., Ackelid, U. (2010), "Titanium Alloys Manufactured with Electron Beam Melting Mechanical and Chemical Properties," *Proceedings from the Materials Processes for Medical Devices Conference,* pp. 189-194.

Thijs, L., Verhaeghe, F., Craeghs, T., Humbeeck, J.V., Kruth, J.P. (2010), "A Study of the Microstructural Evolution During Selective Laser Melting of Ti-6Al-4V," *Acta Materialia 58,* pp. 3303-3312.

Thompson, S.M, Bian, L., Shamsaei, N., Yadollahi, A. (2015), "An Overview of Direct Laser Deposition for Additive Manufacturing Part I Transport Phenomena Modeling and Diagnostics," *Additive Manufacturing 8,* pp. 36-62.

Uhlmann E., Fleck, C., Gerlitzky, G., Faltin, F. (2017), "Dynamical Fatigue Behaviour of Additive Manufactured Products for a Fundamental Life Cycle Approach," *The 24th CIRP Conference on Life Cycle Engineering, Procedia CIRP 61,* pp. 588-593.

Vastola, G., Pei, Q.X., Zhang, Y.W. (2018), "Predictive Model for Porosity in Powder Bed Fusion Additive Manufacturing at High Beam Energy Regime," *Additive Manufacturing 22,* pp. 817-822.

Wallin, F., Eriksson, L.E., Nilsson, M. (2006) “Intermediate Turbine Duct Design and Optimization,” *Proceedings of 25th International Congress of the Aeronautical Sciences.*

Walsh, P.P., Fletcher, P. (2004) “Gas Turbine Performance,” *Blackwell, Oxford*, 2nd Edition.

Wilcox, D.C. (1998) "Turbulence Modeling for CFD," *DCW Industries,* 2 ed.

Wycisk, E., Emmelmann, C., Siddique, S., Walther, F. (2013), "High Cycle Fatigue (HCF) Performance of Ti-6Al-4V Alloy Processed by Selective Laser Melting," *Advanced Materials Research Vols. 816-817,* pp. 134-139.

Wycisk, E., Solbach, A., Siddique, S., Herzog, D., Walther, F., Emmelmann, C. (2014), "Effects of Defects in Laser Additive Manufactured Ti-6Al-4V on Fatigue Properties," *8th International Conference on Photonic Technologies LANE, Physics Procedia 56,* pp. 371-378.

Yadollahi, A., Shamsaei N, Thompson S.M., Elwany A., Bian., L. (2016), "Effects of Building Orientation and Heat Treatment on Fatigue Behaviour of Selective Laser Melted 17-4 PH Stainless Steel," *International Journal of Fatigue 94,* pp. 218-235.

Yaras, M., Sjolander, S.A. (1990) “Development of the Tip Leakage Flow Downstream of a Planer Cascade of Turbine-blades: Vorticity Field,” *ASME Paper*, Vol 112, pp. 610-617.

Yaras, M. (2022), Personal communication via email on March 27, 2022 confirming that modern gas-turbine ITDs possess a notably higher inflow Mach number range of 0.6 to 0.9.

Yoder (2015) “Algebraic Reynolds-stress Modeling of Planar Mixing-layer Flows,” PhD thesis, University of Cincinnati, USA.

Zhang, M., Sun, C.N., Zhang, X., Goh, P.C., Wei, J., Hardacre, D., Li, H. (2017) "Fatigue and Fracture Behaviour of Laser Powder Bed Fusion Stainless Steel 316L: Influence of Processing Parameters," *Materials Science and Engineering A 703,* pp. 251-261.

Zhang, T., Zhang, X.F., Mahallati, A. and Vlasic, E. (2013), "Aerodynamic Design of Low Aspect Ratio of Structural Airfoils within and Inter-Turbine Duct," *American Institute of Aeronautics and Astronautics; International Symposium on Air Breathing Engines,* V.2 or V.3, ISABE-2013-1149, pp 304-311.

Zhang, X.F., Hu, S., Benner, M., Gostelow, P., Vlasic, E. (2010), "Experimental and Numerical Study on an Inter-turbine Duct," *ASME 2010 International Mechanical Engineering Congress and Exposition,* IMECE2010, pp 1-12.

Zhang, Y., Hu, S., Zhang, X.F., Vlasic, E. (2011), "Influence of Swirl Distributions on an Inter-turbine Duct Part II: Hub Swirl Variation," *ASME Turbo Expo,* GT2011, pp 1-11.

Zhang, Y., Wu, L., Guo, X., Kane, S., Deng, Y., Jung, Y.G., Lee, J.H., Zhang, J. (2018) "Additive Manufacturing Materials: A Review," *Journal of Materials Engineering and Performance, Volume 27,* pp. 1-13.

Zhao, X., Li, S., Zhang, M., Liu, Y., Sercombe, T.B., Wang, S., Hao, Y., Yang, R., Murr, L.E. (2016) "Comparison of the Microstructures and Mechanical Properties of Ti-6Al-4V Fabricated by Selective Laser Melting and Electron Beam Melting," *Mater. Des. 95,* pp. 21-31.

Ziolkowski, G., Chlebus, E., Szymczyk, P., Kurzac, J. (2014) "Application of X-ray CT Method for Discontinuity and Porosity Detection in 316L Stainless Steel Parts Produced with SLM Technology," *Archives of Civil and Mechanical Engineering 14,* pp. 608-614.

Appendix A

11 Parameter Method for Generating Guide-Vane Geometry

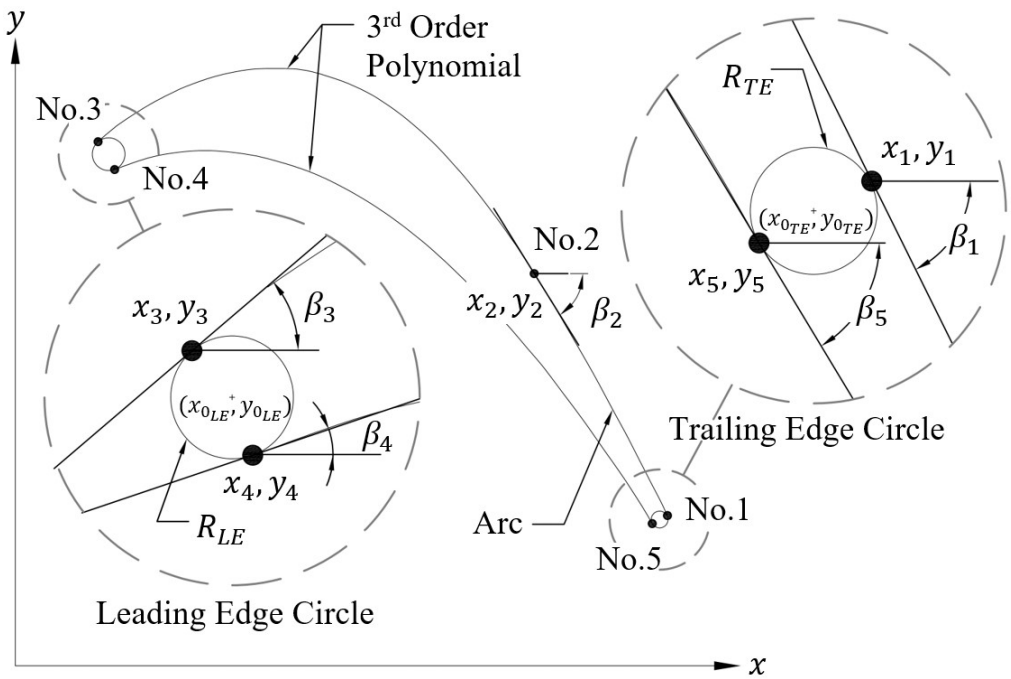

Figure A.1: Eleven parameter method (adapted from Pritchard, 1985)

Point No. 1

$$\beta_1 = \beta'_{out} - \epsilon_{out} \tag{A.1}$$

$$x_1 = c_{v_x} - R_{TE} \cdot (1 + sin\beta_1) \tag{A.2}$$

$$y_1 = R_{TE} \cdot cos\beta_1 \tag{A.3}$$

Point No. 2

$$\beta_2 = \beta'_{out} - \epsilon_{out} + \theta u \tag{A.4}$$

$$x_2 = c_{v_x} - R_{TE} + (o + R_{TE}) \cdot (1 + sin\beta_2) \tag{A.5}$$

$$y_2 = s - (o + R_{TE}) \cdot cos\beta_2 \tag{A.6}$$

Point No. 3

$$\beta_3 = \beta'_{in} + \epsilon_{in} \tag{A.7}$$

$$x_3 = R_{LE} \cdot (1 - sin\beta_3) \tag{A.8}$$

$$y_3 = c_{v_t} + R_{LE} \cdot cos\beta_3 \tag{A.9}$$

Point No. 4

$$\beta_4 = \beta'_{in} - \epsilon_{in} \tag{A.10}$$

$$x_4 = R_{LE} \cdot (1 + sin\beta_4) \tag{A.11}$$

$$y_4 = c_{v_t} - R_{LE} \cdot cos\beta_4 \tag{A.12}$$

Point No. 5

$$\beta_5 = \beta'_{out} + \epsilon_{out} \tag{A.13}$$

$$x_5 = c_{v_x} - R_{TE} \cdot (1 - sin\beta_5) \tag{A.14}$$

$$y_5 = -R_{TE} \cdot cos\beta_5 \tag{A.15}$$

Circular Arc

$$y = y_1 + \left(\frac{x_1 - x_2}{\beta_1 - \beta_2}\right) \cdot \frac{180}{\pi} \cdot \ln\left(\frac{cos\beta_1}{cos\left[\left(\frac{\beta_1-\beta_2}{x_1-x_2}\right)(x - x_2) + \beta_2\right]}\right) \tag{A.16}$$

for $x_2 \leq x \leq x_1$

Third Order Polynomial for Suction Surface

$$d_s = \frac{\tan\beta_3 + tan\beta_2}{(x_3 - x_2)^2} - \frac{2(y_3 - y_2)}{(x_3 - x_2)^3} \tag{A.17}$$

$$c_s = \frac{y_3 - y_2}{(x_3 - x_2)^2} - \frac{tan\beta_2}{(x_3 - x_2)} - d_s(x_3 + 2x_2) \tag{A.18}$$

$$b_s = tan\beta_2 - 2c_s x_2 - 3d_s x_2^2 \tag{A.19}$$

$$a_s = y_2 - b_s x_2 - c_s x_2^2 - d_s x_2^3 \tag{A.20}$$

$$y = a_s + b_s x + c_s x^2 + d_s x^3 \quad \text{for} \quad x_3 \leq x \leq x_2 \tag{A.21}$$

Third Order Polynomial for Pressure Surface

$$d_p = \frac{tan\beta_4 + tan\beta_5}{(x_4 - x_5)^2} - \frac{2(y_4 - y_5)}{(x_4 - x_5)^3} \tag{A.22}$$

$$c_p = \frac{y_4 - y_5}{(x_4 - x_5)^2} - \frac{tan\beta_5}{(x_4 - x_5)} - d_p(x_4 + 2x_5) \tag{A.23}$$

$$b_p = tan\beta_5 - 2c_p x_5 - 3d_p x_5^2 \tag{A.24}$$

$$a_p = y_5 - b_p x_5 - c_p x_5^2 - d_p x_5^3 \tag{A.25}$$

$$y = a_p + b_p x + c_p x^2 + d_p x^3 \quad \text{for} \quad x_4 \leq x \leq x_5 \tag{A.26}$$

Appendix B

Guide-Vane Geometry

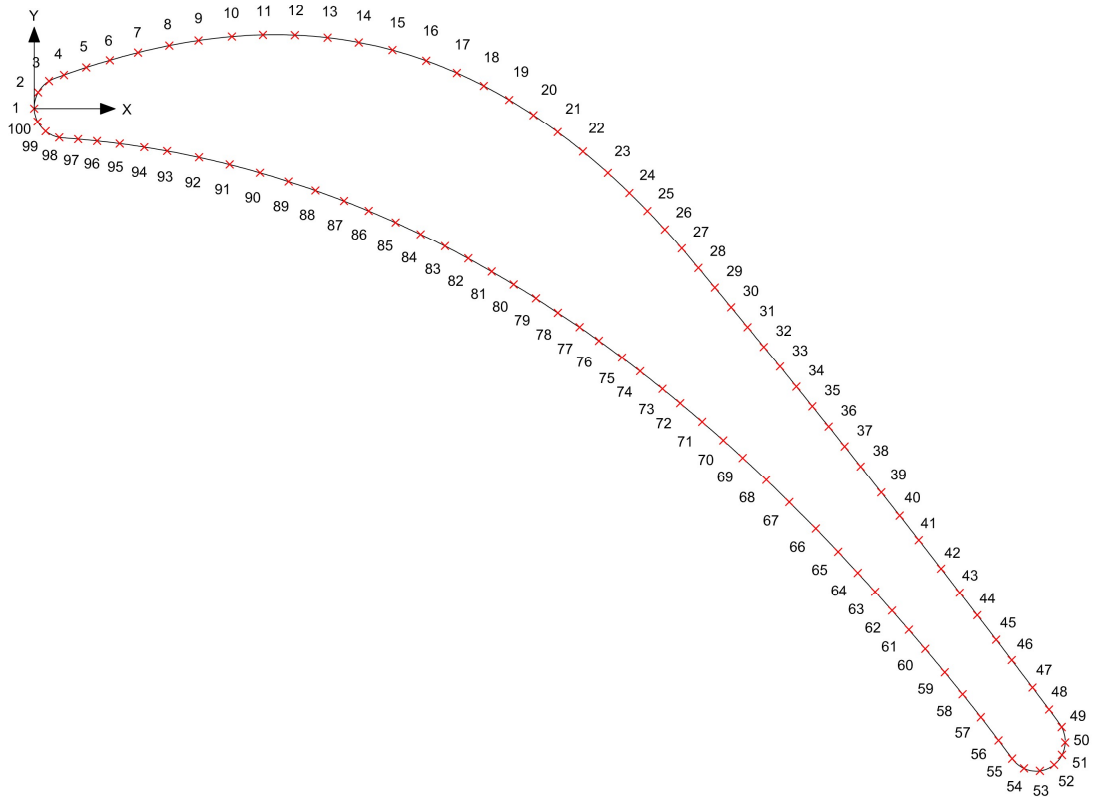

Figure B.1: Guide-vane profile coordinates

Table B.1: Vane geometry 3 coordinates normalized by c_{v_x}

Point	X	Y	Point	X	Y	Point	X	Y	Point	X	Y
1	0	0	26	0.6116	-0.1184	51	0.9968	-0.6285	76	0.5477	-0.2265
2	0.0038	0.0157	27	0.628	-0.1369	52	0.9891	-0.6379	77	0.5289	-0.2133
3	0.0144	0.0266	28	0.6441	-0.1559	53	0.9754	-0.6436	78	0.5079	-0.1994
4	0.0289	0.0324	29	0.6601	-0.1751	54	0.96	-0.6412	79	0.4866	-0.1854
5	0.0505	0.0398	30	0.6759	-0.1941	55	0.9484	-0.6319	80	0.465	-0.172
6	0.0734	0.0466	31	0.6918	-0.2134	56	0.9353	-0.6147	81	0.4437	-0.1595
7	0.1007	0.0541	32	0.7076	-0.2326	57	0.9181	-0.5926	82	0.421	-0.1467
8	0.131	0.0608	33	0.7233	-0.2517	58	0.9004	-0.5703	83	0.3984	-0.1347
9	0.1594	0.0657	34	0.7391	-0.2712	59	0.8831	-0.549	84	0.3747	-0.123
10	0.1918	0.0695	35	0.7546	-0.2903	60	0.8642	-0.5262	85	0.3505	-0.1115
11	0.2219	0.0712	36	0.7705	-0.31	61	0.8483	-0.5076	86	0.3244	-0.1001
12	0.2528	0.0709	37	0.786	-0.3293	62	0.832	-0.4888	87	0.3005	-0.0905
13	0.2845	0.0685	38	0.8015	-0.3487	63	0.8156	-0.4704	88	0.2727	-0.0801
14	0.3148	0.0638	39	0.8215	-0.374	64	0.7987	-0.4519	89	0.2468	-0.0715
15	0.3474	0.0565	40	0.8394	-0.3965	65	0.7797	-0.4315	90	0.2191	-0.0629
16	0.3802	0.0462	41	0.8579	-0.4203	66	0.7581	-0.409	91	0.1896	-0.0548
17	0.4099	0.0344	42	0.8795	-0.4479	67	0.7323	-0.3833	92	0.1599	-0.0478
18	0.4361	0.0219	43	0.8976	-0.4713	68	0.71	-0.3618	93	0.1289	-0.0417
19	0.4606	0.0083	44	0.9146	-0.4933	69	0.6871	-0.3403	94	0.1068	-0.0379
20	0.4842	-0.0066	45	0.9329	-0.5172	70	0.6682	-0.3233	95	0.083	-0.0345
21	0.5077	-0.0231	46	0.948	-0.5371	71	0.6478	-0.3053	96	0.061	-0.0319
22	0.5322	-0.0422	47	0.9681	-0.5638	72	0.6265	-0.2874	97	0.0426	-0.0301
23	0.5564	-0.063	48	0.9842	-0.5852	73	0.6093	-0.2734	98	0.0243	-0.0284
24	0.5772	-0.0827	49	0.9964	-0.6019	74	0.5876	-0.2562	99	0.0111	-0.0223
25	0.5947	-0.1003	50	0.9999	-0.6167	75	0.5701	-0.2429	100	0.0033	-0.0128

Table B.2: Vane geometry 2 coordinates normalized by c_{v_x}

Point	X	Y	Point	X	Y	Point	X	Y	Point	X	Y
1	0	0	26	0.5792	-0.1086	51	0.9999	-0.642	76	0.5751	-0.266
2	0.0051	0.0161	27	0.5973	-0.1272	52	0.9946	-0.6573	77	0.5546	-0.2503
3	0.015	0.0264	28	0.6147	-0.1462	53	0.9858	-0.6651	78	0.5336	-0.2352
4	0.034	0.0335	29	0.6317	-0.1658	54	0.9727	-0.6688	79	0.5125	-0.2202
5	0.0528	0.0383	30	0.6483	-0.1856	55	0.9586	-0.6655	80	0.4911	-0.2057
6	0.074	0.0431	31	0.6649	-0.2055	56	0.9462	-0.6536	81	0.4694	-0.1916
7	0.0959	0.0476	32	0.6814	-0.2254	57	0.9334	-0.6368	82	0.4474	-0.178
8	0.1149	0.0509	33	0.6979	-0.2453	58	0.9202	-0.6197	83	0.4251	-0.1649
9	0.1386	0.0542	34	0.7143	-0.2653	59	0.9067	-0.6025	84	0.4025	-0.1523
10	0.1611	0.0565	35	0.7306	-0.2854	60	0.8943	-0.587	85	0.3708	-0.1357
11	0.1853	0.0581	36	0.7469	-0.3055	61	0.8797	-0.5691	86	0.3399	-0.1209
12	0.2102	0.0586	37	0.7632	-0.3256	62	0.8665	-0.553	87	0.3087	-0.1072
13	0.2371	0.0577	38	0.7828	-0.3501	63	0.85	-0.5335	88	0.2799	-0.0952
14	0.2656	0.0553	39	0.8038	-0.3764	64	0.8327	-0.5133	89	0.249	-0.0839
15	0.2969	0.0506	40	0.8229	-0.4005	65	0.8157	-0.494	90	0.2219	-0.0747
16	0.3291	0.0434	41	0.8439	-0.4271	66	0.7967	-0.4729	91	0.1936	-0.0662
17	0.3593	0.0344	42	0.8631	-0.4516	67	0.7746	-0.449	92	0.1649	-0.0585
18	0.3925	0.0218	43	0.8826	-0.4767	68	0.7547	-0.4282	93	0.1385	-0.0523
19	0.423	0.0076	44	0.9023	-0.5023	69	0.7349	-0.4081	94	0.1112	-0.0467
20	0.4513	-0.0079	45	0.9219	-0.5279	70	0.7112	-0.3847	95	0.0901	-0.043
21	0.4799	-0.026	46	0.9395	-0.5509	71	0.6858	-0.3605	96	0.068	-0.0396
22	0.501	-0.041	47	0.9544	-0.5706	72	0.6618	-0.3385	97	0.0463	-0.0369
23	0.5216	-0.0567	48	0.9682	-0.5888	73	0.6352	-0.3152	98	0.0275	-0.0345
24	0.5414	-0.0733	49	0.9848	-0.611	74	0.6154	-0.2985	99	0.0126	-0.0278
25	0.5607	-0.0906	50	0.9952	-0.625	75	0.5954	-0.2821	100	0.0033	-0.0159

Table B.3: Vane geometry 1 coordinates normalized by c_{v_x}

Point	X	Y	Point	X	Y	Point	X	Y	Point	X	Y
1	0	0	26	0.5732	-0.1189	51	0.9998	-0.6512	76	0.5825	-0.2992
2	0.0037	0.018	27	0.591	-0.1376	52	0.9964	-0.6621	77	0.5575	-0.28
3	0.0134	0.031	28	0.6085	-0.1566	53	0.9895	-0.6703	78	0.532	-0.2605
4	0.0303	0.0397	29	0.626	-0.1757	54	0.9786	-0.6757	79	0.504	-0.2401
5	0.0517	0.0428	30	0.6433	-0.1948	55	0.9634	-0.6752	80	0.4799	-0.2232
6	0.0741	0.0456	31	0.6606	-0.2141	56	0.9511	-0.6672	81	0.4514	-0.2042
7	0.0975	0.0481	32	0.6777	-0.2334	57	0.9376	-0.6514	82	0.4217	-0.1855
8	0.1228	0.0502	33	0.6948	-0.2528	58	0.9262	-0.6379	83	0.3958	-0.1699
9	0.1487	0.0516	34	0.7164	-0.2778	59	0.9109	-0.6202	84	0.3698	-0.1551
10	0.1753	0.0522	35	0.7325	-0.2967	60	0.8929	-0.5996	85	0.3407	-0.1395
11	0.2019	0.0518	36	0.7523	-0.3199	61	0.8769	-0.5816	86	0.3125	-0.1254
12	0.2299	0.0502	37	0.7753	-0.3475	62	0.8584	-0.5614	87	0.2861	-0.1129
13	0.2597	0.047	38	0.7986	-0.3756	63	0.8413	-0.5427	88	0.2601	-0.1015
14	0.2878	0.0425	39	0.8206	-0.4029	64	0.8232	-0.5233	89	0.2361	-0.0918
15	0.3144	0.0367	40	0.838	-0.4244	65	0.8056	-0.5048	90	0.2116	-0.0825
16	0.3398	0.0297	41	0.8552	-0.4464	66	0.7887	-0.4871	91	0.1857	-0.0735
17	0.3648	0.0213	42	0.8726	-0.4685	67	0.7707	-0.4691	92	0.1599	-0.0654
18	0.3916	0.0106	43	0.892	-0.4936	68	0.7492	-0.4482	93	0.1378	-0.0591
19	0.4214	-0.0036	44	0.9083	-0.5148	69	0.7292	-0.429	94	0.1172	-0.0538
20	0.4476	-0.0182	45	0.9249	-0.5369	70	0.7079	-0.4086	95	0.0931	-0.0484
21	0.4747	-0.0355	46	0.9421	-0.5599	71	0.688	-0.3897	96	0.0721	-0.044
22	0.4958	-0.0506	47	0.9608	-0.5854	72	0.6685	-0.3721	97	0.0507	-0.0403
23	0.5161	-0.0665	48	0.9782	-0.6092	73	0.6459	-0.3521	98	0.0304	-0.0371
24	0.5358	-0.0833	49	0.9881	-0.6229	74	0.6262	-0.3354	99	0.0163	-0.0307
25	0.5548	-0.1007	50	0.998	-0.6382	75	0.6064	-0.3187	100	0.0053	-0.0184

Appendix C

Strut Geometry

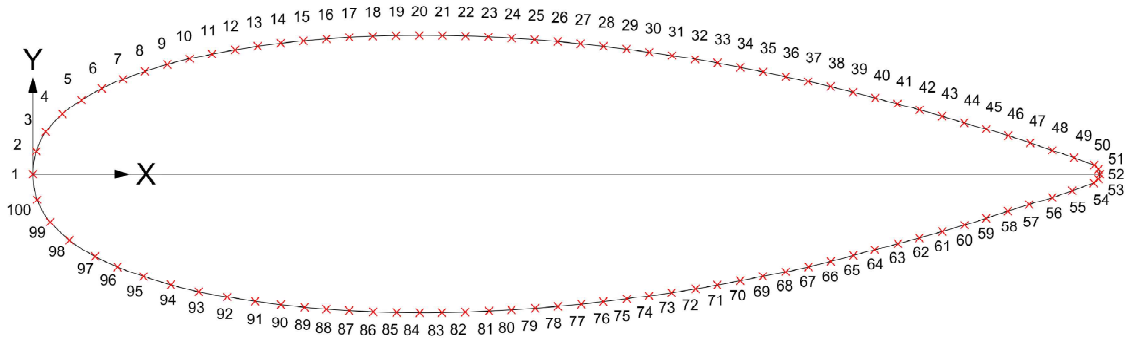

Figure C.1: Strut profile coordinates

Table C.1: Strut coordinates normalized by c_{s_x}

Point	X	Y	Point	X	Y	Point	X	Y	Point	X	Y
1	0	0	26	0.4918	0.1241	51	0.9988	0.0047	76	0.5346	-0.1198
2	0.0031	0.0212	27	0.5133	0.1221	52	1	0	77	0.514	-0.1221
3	0.012	0.0395	28	0.5348	0.1198	53	0.9986	-0.0048	78	0.492	-0.1242
4	0.0276	0.0563	29	0.5564	0.1171	54	0.9942	-0.0085	79	0.4707	-0.1259
5	0.0455	0.0694	30	0.5777	0.1143	55	0.9781	-0.0142	80	0.4485	-0.1273
6	0.0646	0.08	31	0.599	0.1111	56	0.9554	-0.0219	81	0.4275	-0.1284
7	0.0844	0.0888	32	0.6206	0.1076	57	0.9337	-0.0287	82	0.4052	-0.1293
8	0.105	0.0963	33	0.6416	0.104	58	0.9137	-0.0349	83	0.3833	-0.1297
9	0.126	0.1027	34	0.663	0.1	59	0.8935	-0.0414	84	0.3626	-0.1299
10	0.147	0.108	35	0.6844	0.0958	60	0.8731	-0.0479	85	0.3409	-0.1296
11	0.1679	0.1125	36	0.7056	0.0914	61	0.8523	-0.054	86	0.319	-0.129
12	0.1895	0.1165	37	0.7265	0.0867	62	0.8307	-0.0599	87	0.2964	-0.128
13	0.2107	0.1198	38	0.7477	0.0818	63	0.8107	-0.0652	88	0.275	-0.1266
14	0.2323	0.1225	39	0.7687	0.0766	64	0.789	-0.071	89	0.2546	-0.1249
15	0.2536	0.1248	40	0.7895	0.0713	65	0.7689	-0.0765	90	0.2324	-0.1226
16	0.2752	0.1266	41	0.8102	0.0658	66	0.7478	-0.0819	91	0.2083	-0.1195
17	0.2965	0.128	42	0.831	0.0601	67	0.727	-0.0869	92	0.1821	-0.1154
18	0.3185	0.129	43	0.8521	0.0542	68	0.7055	-0.0917	93	0.1554	-0.1102
19	0.3402	0.1296	44	0.8728	0.0482	69	0.6841	-0.0961	94	0.1293	-0.1039
20	0.3621	0.1298	45	0.8935	0.0421	70	0.6629	-0.1002	95	0.1036	-0.0962
21	0.3837	0.1297	46	0.9142	0.0358	71	0.6413	-0.1041	96	0.0793	-0.087
22	0.4054	0.1292	47	0.9347	0.0293	72	0.6212	-0.1076	97	0.0582	-0.0774
23	0.4269	0.1284	48	0.9553	0.0223	73	0.5986	-0.1112	98	0.0342	-0.0619
24	0.4486	0.1273	49	0.9757	0.015	74	0.5775	-0.1143	99	0.0162	-0.045
25	0.4702	0.1259	50	0.9947	0.0083	75	0.5567	-0.1171	100	0.004	-0.024

Appendix D

Mixed-out Flow Parameters

The mixed-out flow parameters downstream of the guide-vane row were obtained using a control volume analysis derived by Benner (2003) between the axial planes at station 2 and "mix" in Figure 4.3. The control volume analysis assumes that the flow is incompressible and the mixing occurs at constant area. As shown in Figure D.1, the static pressure and flow velocity is typically spatially non-uniform at plane 2 which corresponds to the control volume inlet plane and eventually achieves uniformity at the mixed-out plane which corresponds to the control volume outlet plane. The control volume terminations in the pitchwise direction are spaced one guide-vane pitch apart so that the conditions along these boundaries are periodic. The mixed-out velocity and total pressure quantities at the control volume outlet are given by:

$$u_{mix} = \int_0^1 u_2 \, d(y/s) \tag{D.1}$$

$$v_{mix} = \frac{\int_0^1 v_2 \, u_2 \, d(y/s)}{\int_0^1 u_2 \, d(y/s)} \tag{D.2}$$

$$U_{mix} = \sqrt{u_{mix}^2 + v_{mix}^2} \tag{D.3}$$

$$\widetilde{P}_{o,mix} = \int_0^1 P_2 \, d(y/s) - \rho \Big[\int_0^1 u_2 \, d(y/s) \Big]^2 + \rho \int_0^1 u_2^2 \, d(y/s) + \frac{1}{2} \rho \, U_{mix}^2 \quad \text{(D.4)}$$

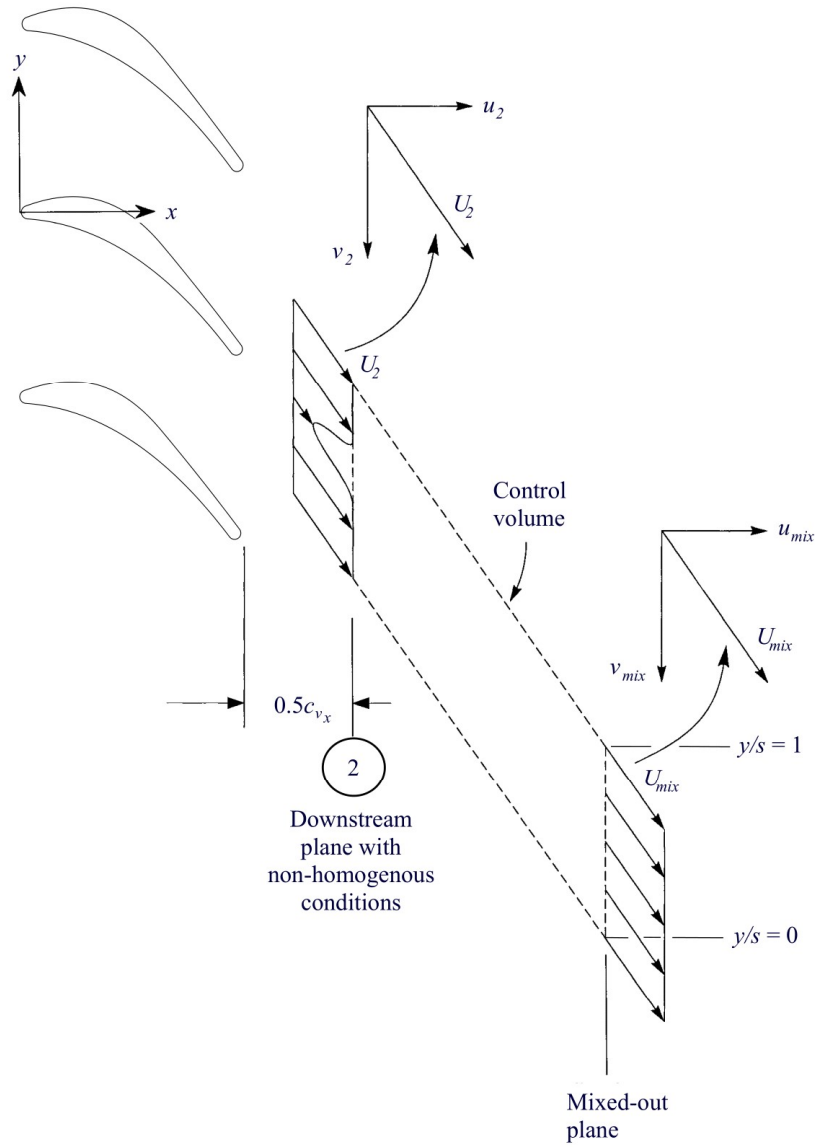

Figure D.1: Control volume used for derivation of mixed-out profile loss (adapted from Benner, 2003)

Appendix E

Grid Sensitivity Study for a Strut and a Row of Guide-Vanes in Tandem Configuration

This chapter presents the grid sensitivity study for a strut and a row of guide-vanes in tandem configuration. As shown in Figure E.1, the grid-node count, N_{wake}, in the direction of maximum velocity gradient for the strut and middle guide-vane wake was progressively doubled and the resulting momentum thickness and peak minimum flow velocity within the indicated pitchwise boundaries were calculated for five axial locations. The grid-node count, N_{wake}, extended across the entire domain in the streamwise direction as denoted by the red-coloured region shown in Figure E.1. A constant grid-node count of 103 in the pitchwise direction was used outside the region bound by the red-coloured lines for each guide-vane passage. Further increases in this grid-node count did not influence the grid sensitivity results in the middle guide-vane wake.

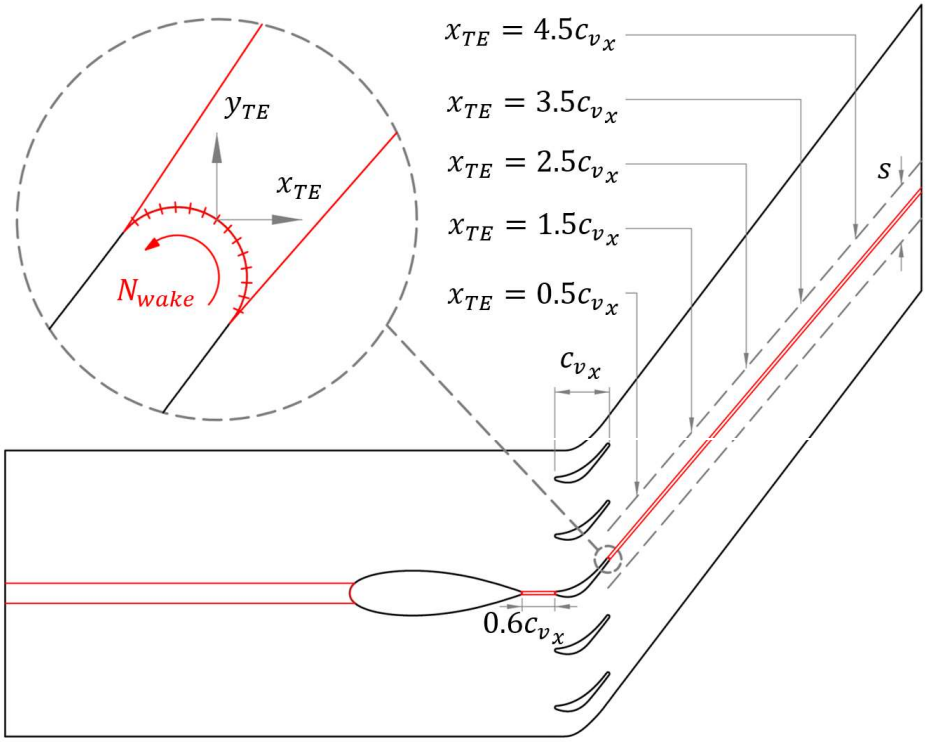

Figure E.1: Grid sensitivity analysis of tandem strut and middle guide-vane wake

The momentum thickness and peak minimum flow velocity converged to within 1% of the final value at $N_{wake} = 60$ for all five axial locations downstream of the guide-vane row trailing edge, as shown in Figure E.2 and E.3, respectively. Hence, this grid-node count was applied to all five guide-vanes and the strut. Figure E.4 presents the grid-node counts along the streamwise and wall normal directions for the strut and guide-vanes.

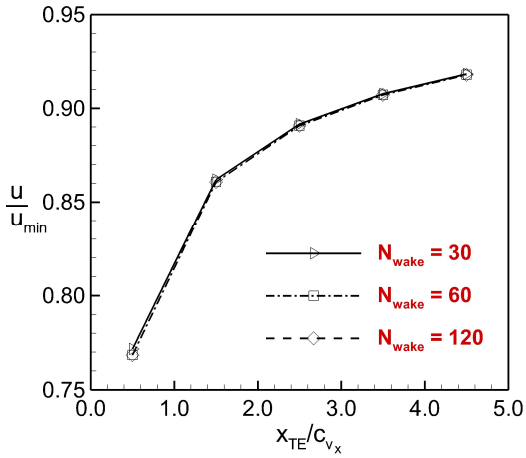

Figure E.2: Streamwise variation of minimum streamwise velocity in the wake of the middle guide-vane

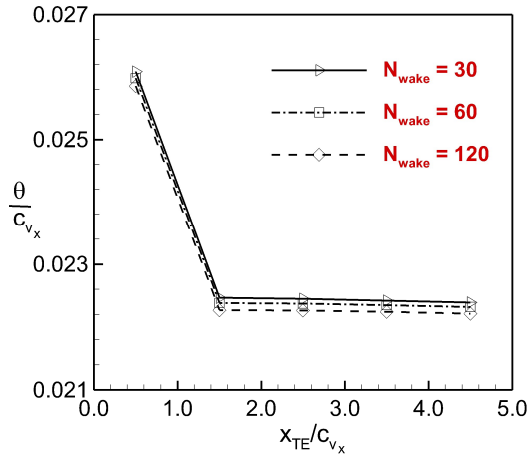

Figure E.3: Streamwise variation of momentum thickness in the wake of the middle guide-vane

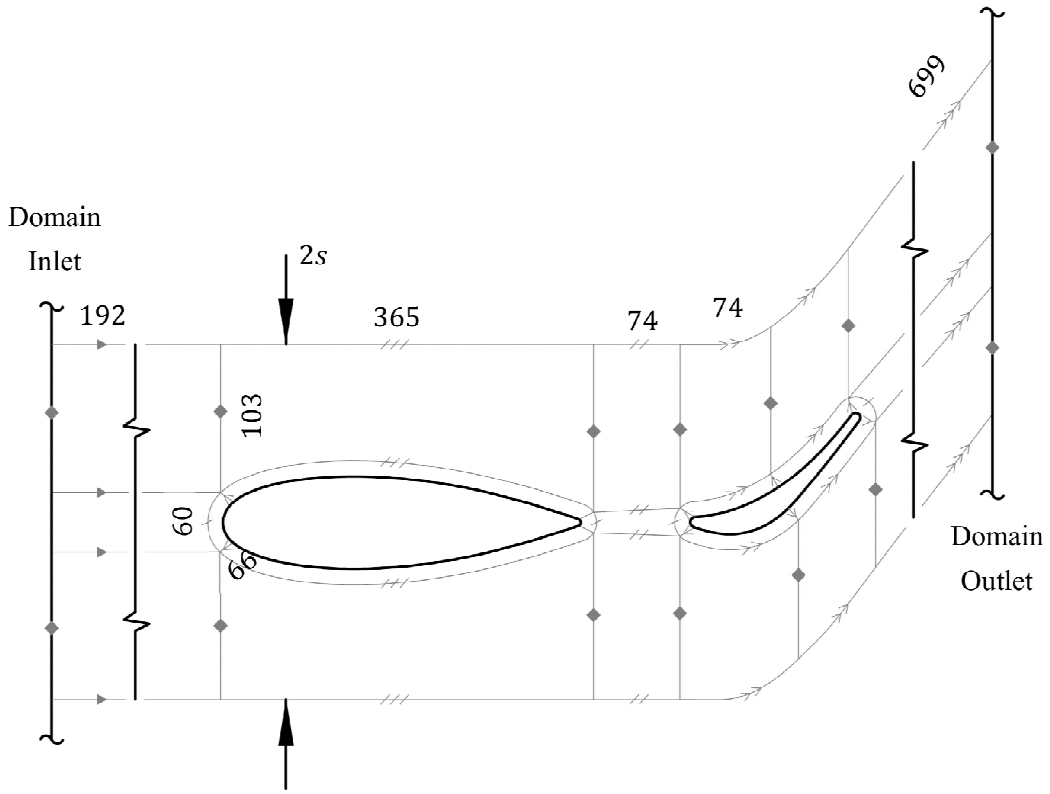

Figure E.4: Computational grid-node count for strut and a row of guide-vanes

Appendix F

Discretization Error Analysis for a Benchmark Zero-Pressure-Gradient Turbulent Boundary Layer

This chapter presents the method used to calculate the discretization error for the numerical solution of the zero-pressure-gradient turbulent boundary layer. The discretization error was estimated using the Richardson extrapolation method (Richardson, 1910) for non-integer grid refinement ratios. This method uses three progressively finer grids to extrapolate key variable(s) for a theoretical grid-node spacing of zero. The key parameter used to assess the discretization error was the momentum thickness Reynolds number, Re_θ, calculated at a streamwise location of $0.635L_{fp}$, where L_{fp} is the domain length in the streamwise direction, for three different grids with respective grid-cell-size growth rates of $5\%, 10\%$ and 15% in the wall-normal direction. The following section presents the equations used to calculate the extrapolated momentum thickness Reynolds number, $Re_{\theta_{ext}}$, corresponding to a grid of zero node spacing and the grid convergence index, GCI. The representative grid-node spacing of each grid, h, is first calculated using:

$$h = \left[\frac{1}{N} \sum_{i=1}^{N} (\Delta V_i) \right]^{\frac{1}{3}} \tag{F.1}$$

where ΔV_i is the volume of the ith cell and N is the total number of cells. Based on a representative cell height numbering scheme of $h_1 < h_2 < h_3$, the apparent order, p, is solved iteratively using Eq. F.2- F.4:

$$p = \frac{1}{\ln(h_2/h_1)} \left| \ln \left| \frac{Re_{\theta_3} - Re_{\theta_2}}{Re_{\theta_2} - Re_{\theta_1}} \right| + q(p) \right| \tag{F.2}$$

$$q(p) = \ln \left(\frac{(h_2/h_1)^p - s*}{(h_3/h_2)^p - s*} \right) \tag{F.3}$$

$$s* = 1 \cdot \left(\frac{Re_{\theta_3} - Re_{\theta_2}}{Re_{\theta_2} - Re_{\theta_1}} \right) \tag{F.4}$$

The resulting extrapolated momentum thickness Reynolds number, ${Re_{\theta_{ext}}}^{21}$, for a grid size, h_1, is given by:

$${Re_{\theta_{ext}}}^{21} = \frac{(h_2/h_1)^p Re_{\theta_1} - Re_{\theta_2}}{(h_2/h_1)^p - 1} \tag{F.5}$$

The approximate relative error, ${e_a}^{21}$, and extrapolated error, ${e_{ext}}^{21}$, for h_1 are given by:

$${e_a}^{21} = \left| \frac{Re_{\theta_1} - Re_{\theta_2}}{Re_{\theta_1}} \right| \tag{F.6}$$

$${e_{ext}}^{21} = \left| \frac{{Re_{\theta_{ext}}}^{21} - Re_{\theta_1}}{{Re_{\theta_{ext}}}^{21}} \right| \tag{F.7}$$

The GCI as defined by Roache(1996) is the percentage error between the computed value and the theoretical asymptotic numerical value. For grid size, h_1, it is given by:

$$GCI^{21} = \frac{1.25{e_a}^{21}}{(h_2/h_1)^p - 1} \tag{F.8}$$

Eq. F.5- F.8 can similarly be applied to the coarser grid size, h_2. The calculated results for h_1 and h_2 are presented in Table F.1. As shown in Table F.1, the chosen grid size, h_1, possesses a numerical error of $7.39 \times 10^{-4}\%$ for the momentum thickness Reynolds number.

Table F.1: Discretization error of computational grid for a turbulent boundary layer

Parameter	Units	Grid		
		1	**2**	**3**
N	–	3.63×10^6	1.65×10^6	1.11×10^6
h	(m)	3.3×10^{-3}	4.3×10^{-3}	4.9×10^{-3}
Re_θ	–	1410	1409	1420
p	–	18.07		
$Re_{\theta_{ext}}$	–	1410	1408	–
e_a	–	0.07	0.82	–
e_{ext}	–	6.2×10^{-4}	0.08	–
GCI	(%)	$\mathbf{7.39 \times 10^{-4}}$	0.11	–

Appendix G

Supplemental Computational Results for a Zero-Pressure-Gradient Turbulent Boundary Layer

This chapter presents the DNS results of Spalart (1988) and the numerical results of the RANS-based BSL Reynolds-stress model for a zero-pressure-gradient turbulent boundary layer. Figures G.1 and G.2 present the wall-normal (y-direction) profiles of the production, pressure-strain rate, viscous diffusion, turbulence diffusion and dissipation terms in the Reynolds-stress transport equations for $\overline{u_2'u_2'}$ and $\overline{u_3'u_3'}$, respectively, at a streamwise location corresponding to $Re_\theta = 1410$. The subscripts 2 and 3 used in the Reynolds-stress correspond to the Cartesian, y and z directions, respectively. All terms shown in Figure 4.22 are normalized by the kinematic viscosity, ν, and the friction velocity, u_τ, corresponding to $Re_\theta = 1410$.

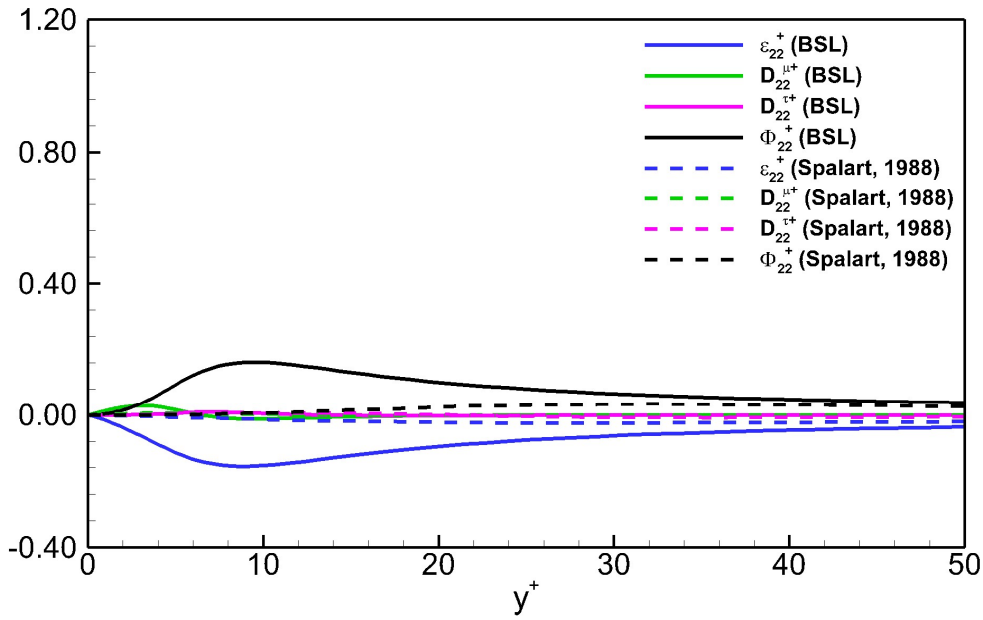

Figure G.1: Wall-normal variation of the terms in the $\overline{u_2'u_2'}$ Reynolds-stress transport equation at $Re_\theta = 1410$

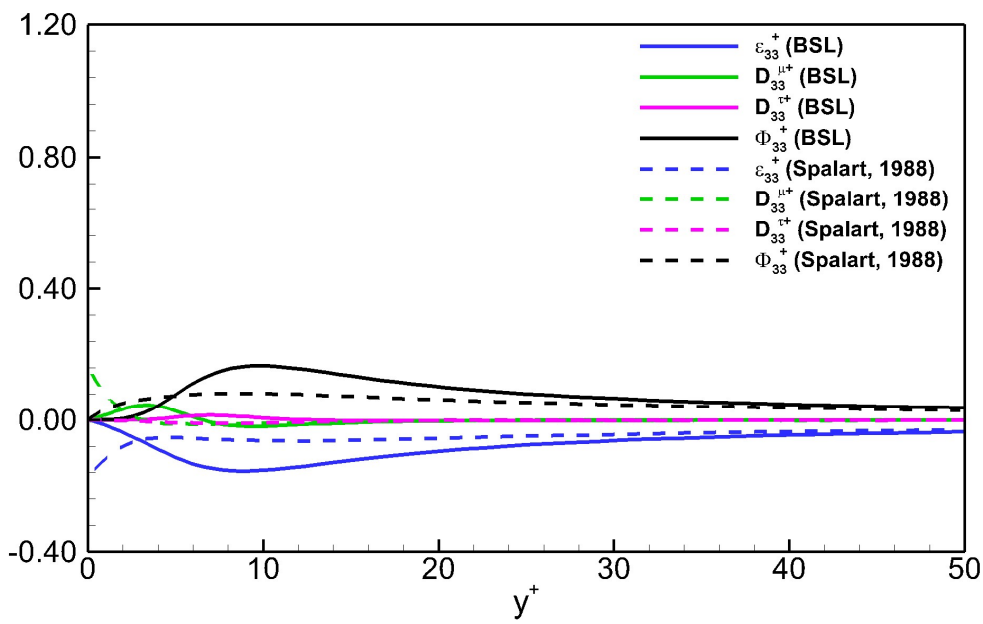

Figure G.2: Wall-normal variation of the terms in the $\overline{u_3'u_3'}$ Reynolds-stress transport equation at $Re_\theta = 1410$

Appendix H

Calibration of BSL Reynolds-stress Model for a Turbulent Planar Free-Shear Layer

This chapter presents the results of the calibration procedure used with the intent to improve the accuracy of the wake velocity profile and mixing-layer growth rate produced by the RANS-based BSL Reynolds-stress model for a planar turbulent free-shear layer. The calibration procedure involved independent, systematic adjustments to coefficients, C_1 and C_2 associated with the slow and fast sub-terms, respectively, in the pressure-strain rate term given in Eq. 3.14. As shown in Figure H.1, twelve cases were simulated. Each case is denoted by the prefix letter, A, followed by the case number. The range of magnitudes for coefficients, C_1 and C_2 were selected based on the recommendations of Yoder (2005) and based on the ability of the RANS-based BSL Reynolds-stress model to achieve proper convergence. Figure H.2 presents the velocity profile downstream of the splitter-plate at a streamwise location of $x = 0.038L_{sp}$ for all twelve cases against the experimental data of Mehta (1991) where L_{sp} is the splitter-plate length. Figure H.3 presents the mixing-layer growth rate for four cases against the experimental data of Mehta (1991).

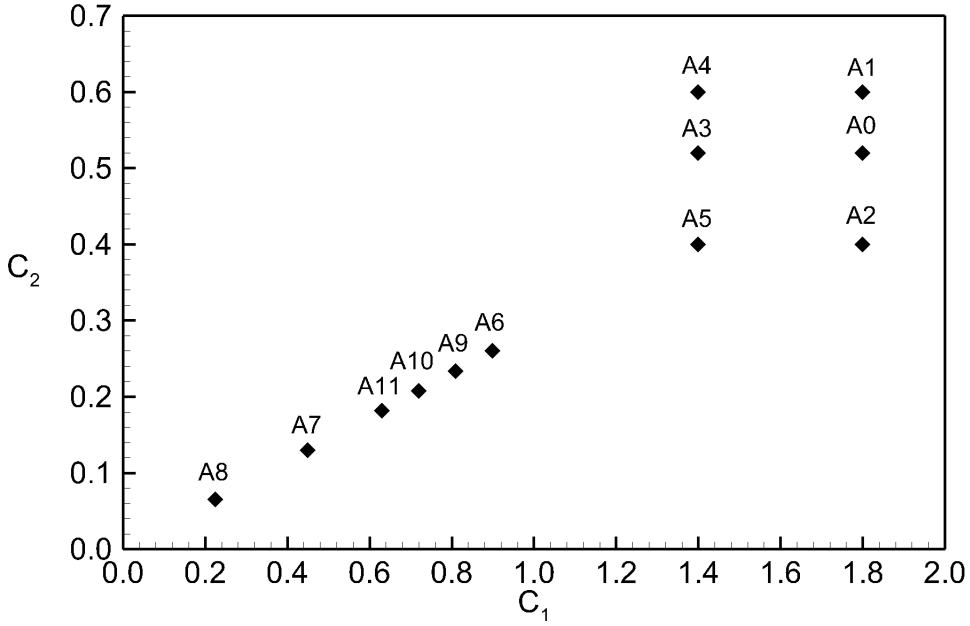

Figure H.1: Calibration coefficient values considered for the pressure-strain rate tensor, Φ_{ij}

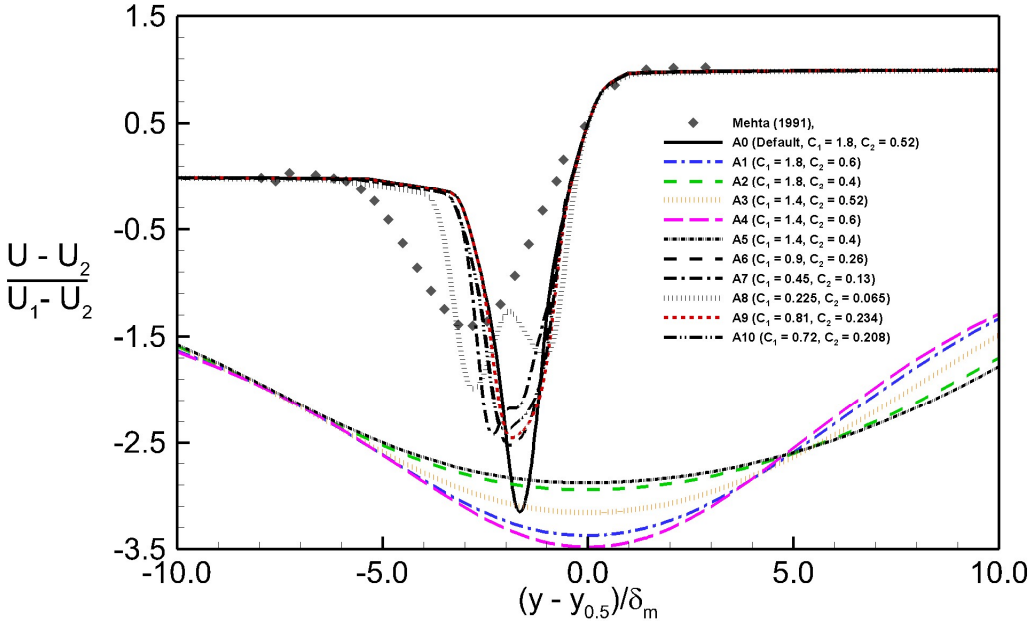

Figure H.2: Sensitivity of the planar turbulent free-shear layer velocity profile at $x = 0.038L_{sp}$ to varying values of C_1 and C_2 in the RANS-based BSL Reynolds-stress model

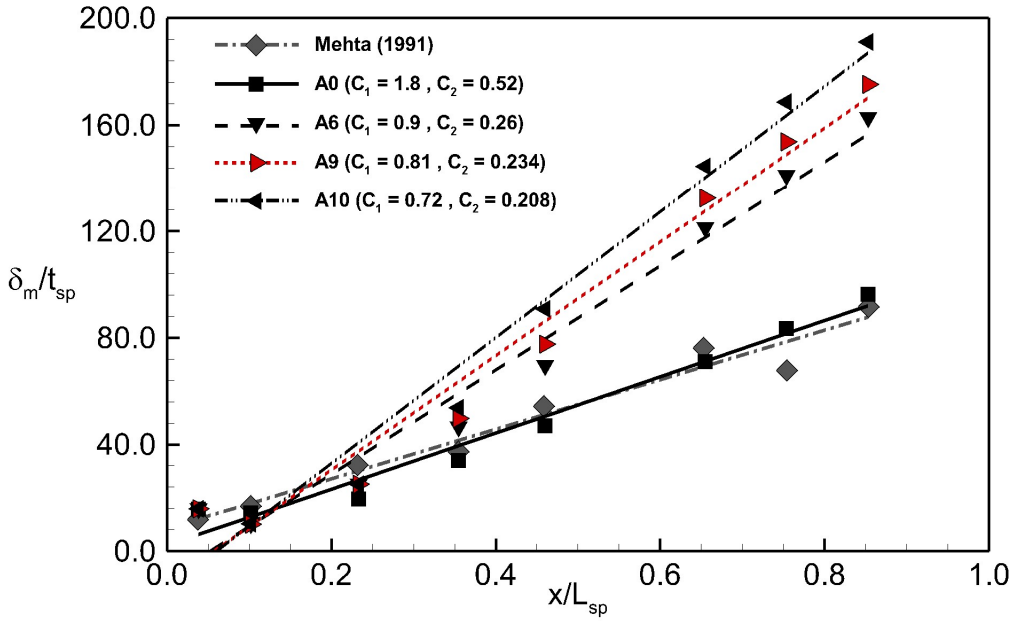

Figure H.3: Sensitivity of the planar turbulent free-shear layer mixing-layer growth rate to varying values of C_1 and C_2 in the RANS-based BSL Reynolds-stress model

Appendix I

Technical Drawings for the High-Speed Rectilinear Test Section for a Strut and a Row of Guide Vanes in Tandem Configuration

This page left intentionally blank.

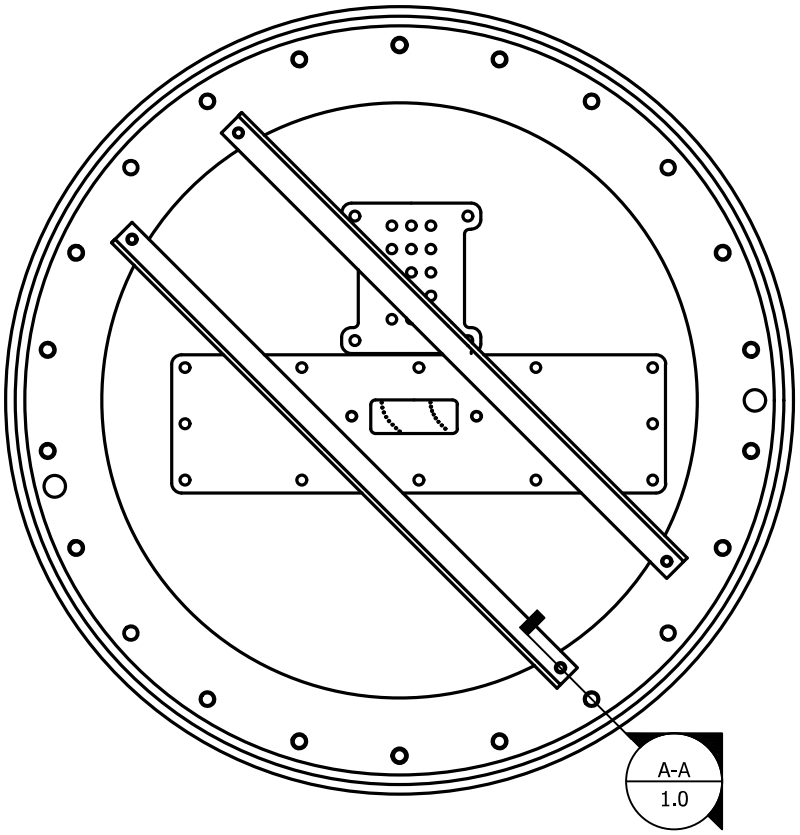

1 / 1.0 TEST SECTION ASSEMBLY

SCALE: 1:5

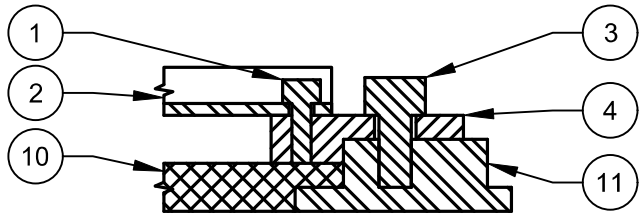

A-A / 1.0 TEST SECTION DETAIL

SCALE: 1:3

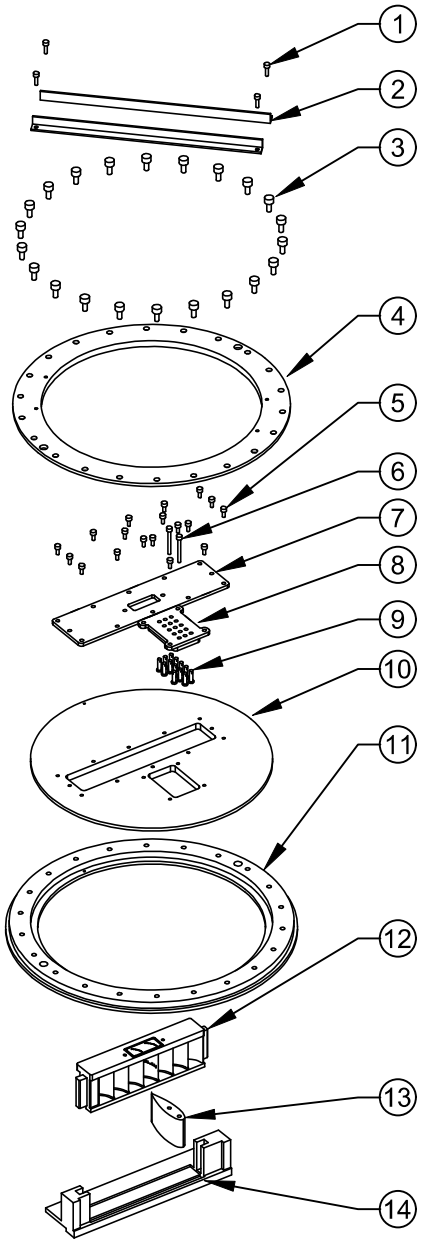

2 / 1.0 EXPLODED TEST SECTION

SCALE: NA

TAG	COMPONENT	QTY	TAG	COMPONENT	QTY	TAG	COMPONENT	QTY
1	1/4-20 UNC L3/4" BOLT	4	6	12-24 UNC L1" BOLT	2	10	PLEXIGLASS WINDOW	1
2	3/4" x 3/4" x 1/8" ANGLE	2	7	CASCADE COVER	1	11	BOTTOM RING	1
3	3/8-16 UNC L1/2" BOLT	22	8.1	STRUT ENDWALL1	1	12	GUIDE-VANE CASCADE	1
4	TOP RING	1	8.1	STRUT ENDWALL2	1	13	STRUT	1
5	1/4-20 UNC L1/2" BOLT	18	9	1/4" CLEVIS PIN	15	14	BASEPLATE (EXISTING)	1

PROJECT:

HIGH-SPEED TEST SECTION

DRAWING:

TEST SECTION ASSEMBLY

2	16-APRIL-2019
3	21-APRIL-2019
4	26-APRIL-2019
5	29-APRIL-2019
6	7-MAY-2019
7	9-MAY-2019

SIZE:	MATERIAL:	TOLERANCES:	DESIGN:	DIMENSION: INCHES	QTY: 1
8.5"x11"	SEE DRAWINGS 1.1 - 1.12	+/- 0.005 INCHES	A. BRONIPOLSKY ANDREIBRONIPOLSKY@CMAIL.CARLETON.CA	DRAWING #: 1.0	
			SHEET: 1 OF 12		

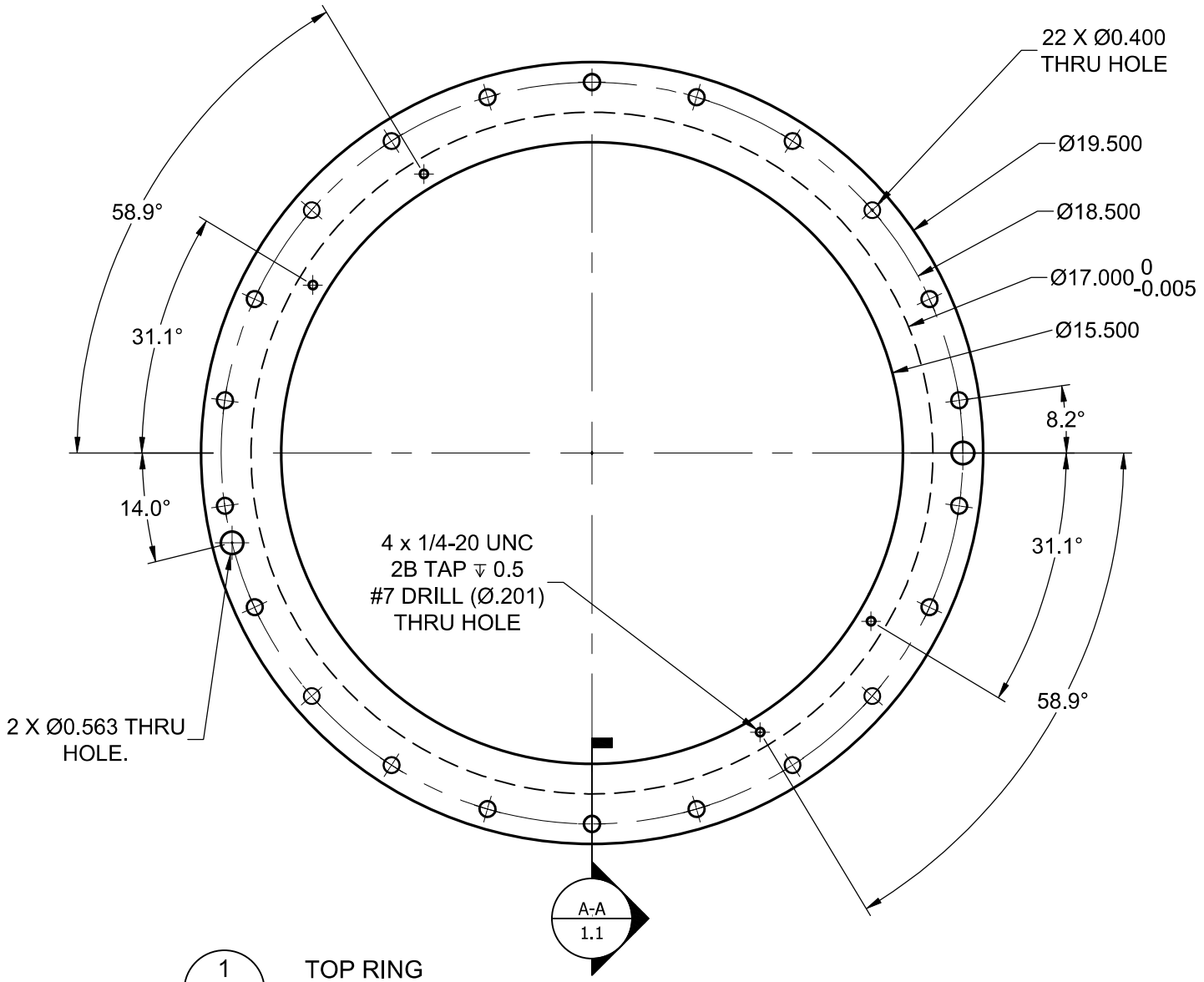

1 / 1.1 TOP RING

SCALE: 1:4

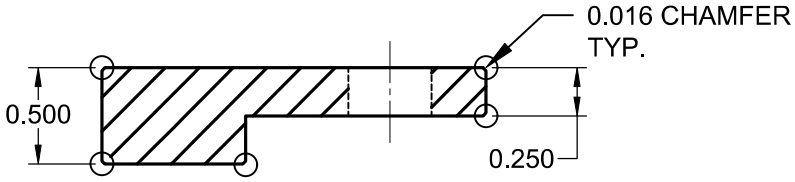

A-A / 1.1 TOP RING SECTION

SCALE: 1:1

PROJECT: HIGH-SPEED TEST SECTION	2	16-APRIL-2019	
	3	21-APRIL-2019	
	4	26-APRIL-2019	
	5	29-APRIL-2019	
DRAWING: TOP RING	6	7-MAY-2019	
	7	9-MAY-2019	
	8	13-MAY-2019	

SIZE:	MATERIAL:	TOLERANCES:		DESIGN:	DIMENSION: INCHES	QTY: 1
8.5"x11"	MILD STEEL ASTM (SA36)	+/- 0.005 INCHES		A. BRONIPOLSKY ANDREIBRONIPOLSKY@CMAIL.CARLETON.CA	DRAWING #: 1.1	
				SHEET: 2 OF 12		

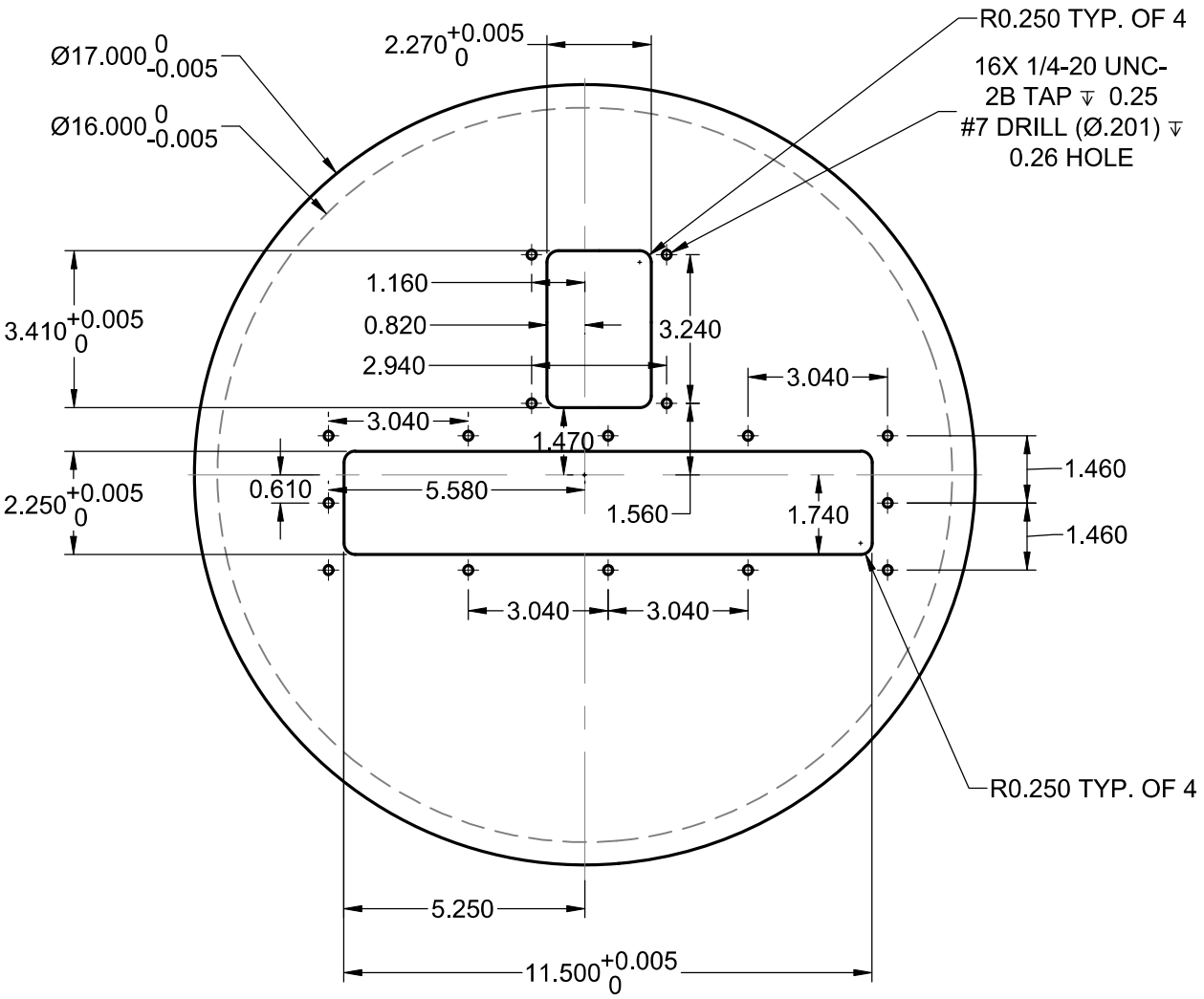

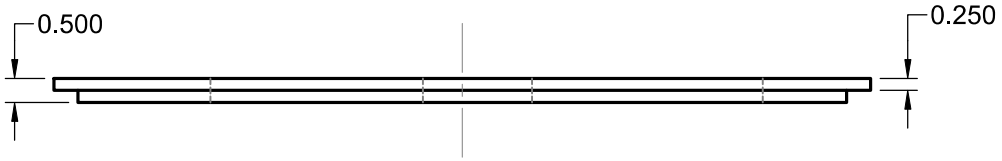

1 / 1.2 PLEXIGLASS COVER

SCALE: 1:4

PROJECT: HIGH-SPEED TEST SECTION	2	16-APRIL-2019
	3	21-APRIL-2019
	4	26-APRIL-2019
	5	29-APRIL-2019
DRAWING: PLEXIGLASS WINDOW	6	7-MAY-2019
	7	9-MAY-2019

SIZE:	MATERIAL:	TOLERANCES:		DESIGN:	DIMENSION: INCHES	QTY: 1
8.5"x11"	ACRYLIC (PMMA)	+/- 0.005 INCHES		A. BRONIPOLSKY ANDREIBRONIPOLSKY@CMAIL.CARLETON.CA	DRAWING #: 1.2	
				SHEET: 2 OF 12		

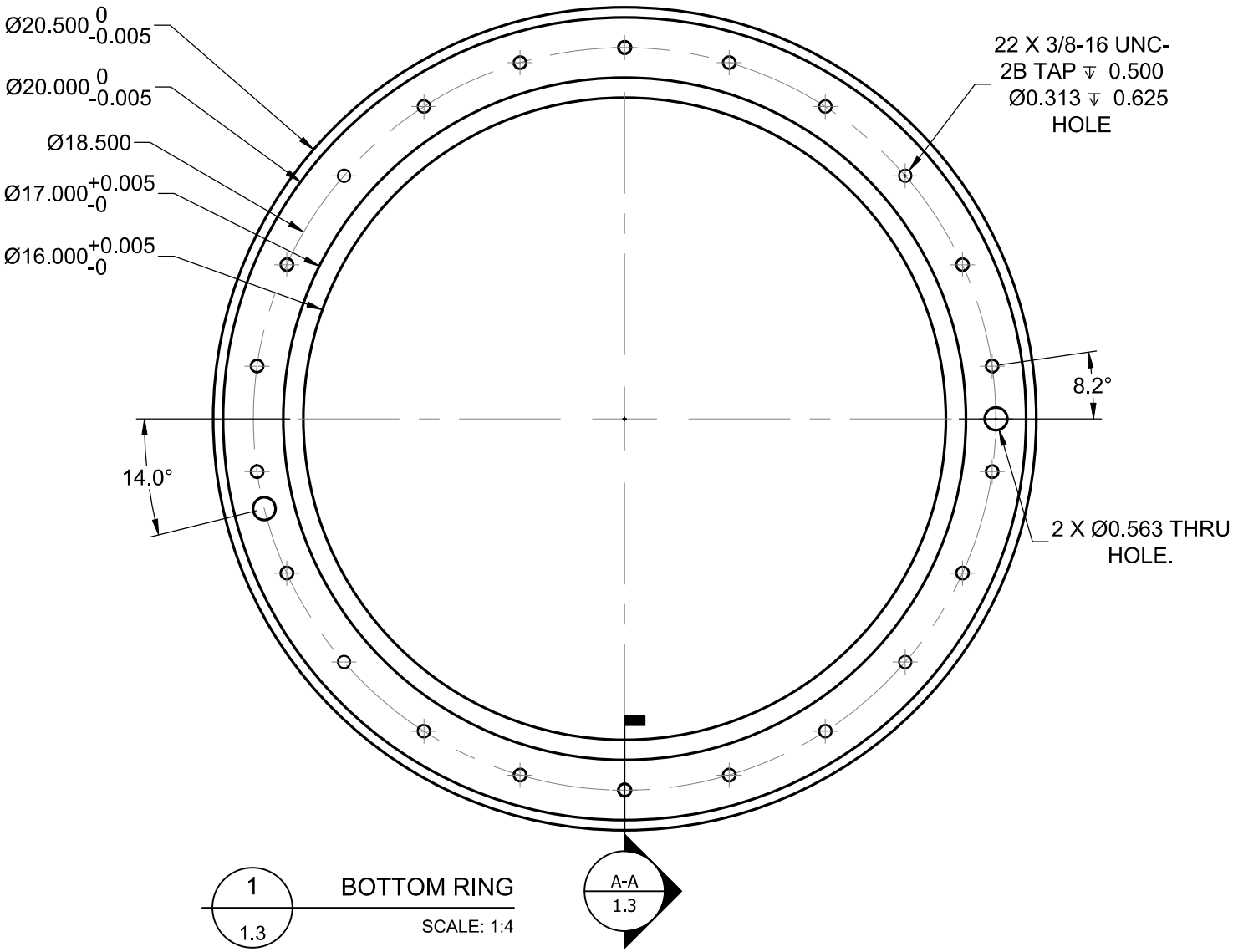

1 / 1.3 BOTTOM RING

SCALE: 1:4

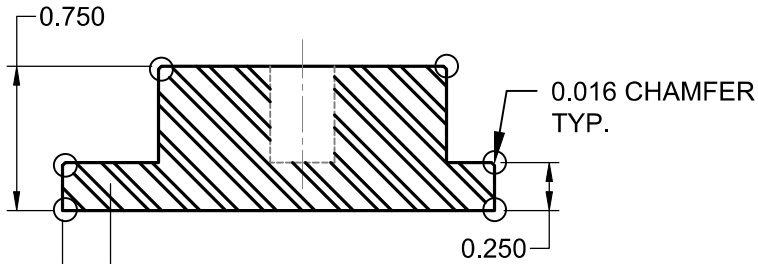

A-A / 1.3 BOTTOM RING SECTION

SCALE: 1:1

PROJECT: HIGH-SPEED TEST SECTION	2	16-APRIL-2019	
	3	21-APRIL-2019	
	4	26-APRIL-2019	
	5	29-APRIL-2019	
DRAWING: BOTTOM RING	6	7-MAY-2019	
	7	9-MAY-2019	
	8	13-MAY-2019	

SIZE:	MATERIAL:	TOLERANCES:		DESIGN:	DIMENSION: INCHES	QTY: 1
8.5"x11"	MILD STEEL ASTM (SA36)	+/- 0.005 INCHES		A. BRONIPOLSKY ANDREIBRONIPOLSKY@CMAIL.CARLETON.CA	DRAWING #: 1.3	
				SHEET: 3 OF 12		

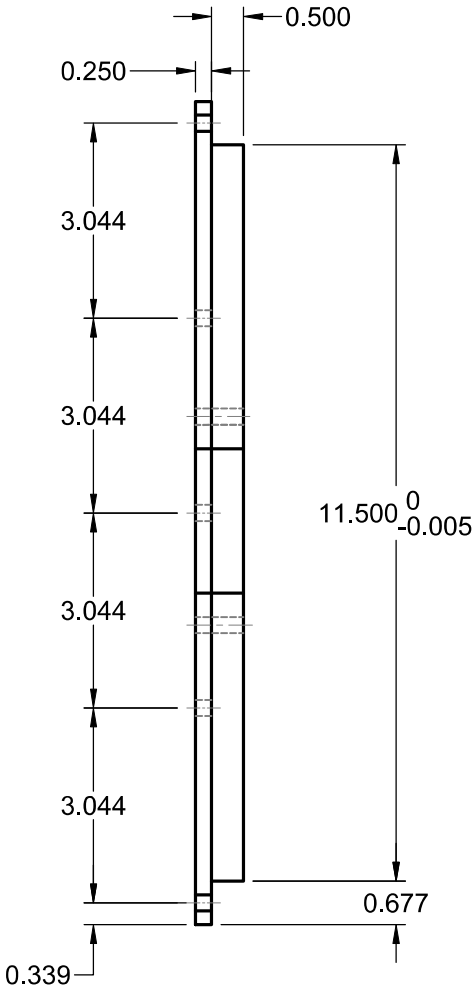

A-A 1.4 CASCADE COVER SECTION

SCALE: 1:3

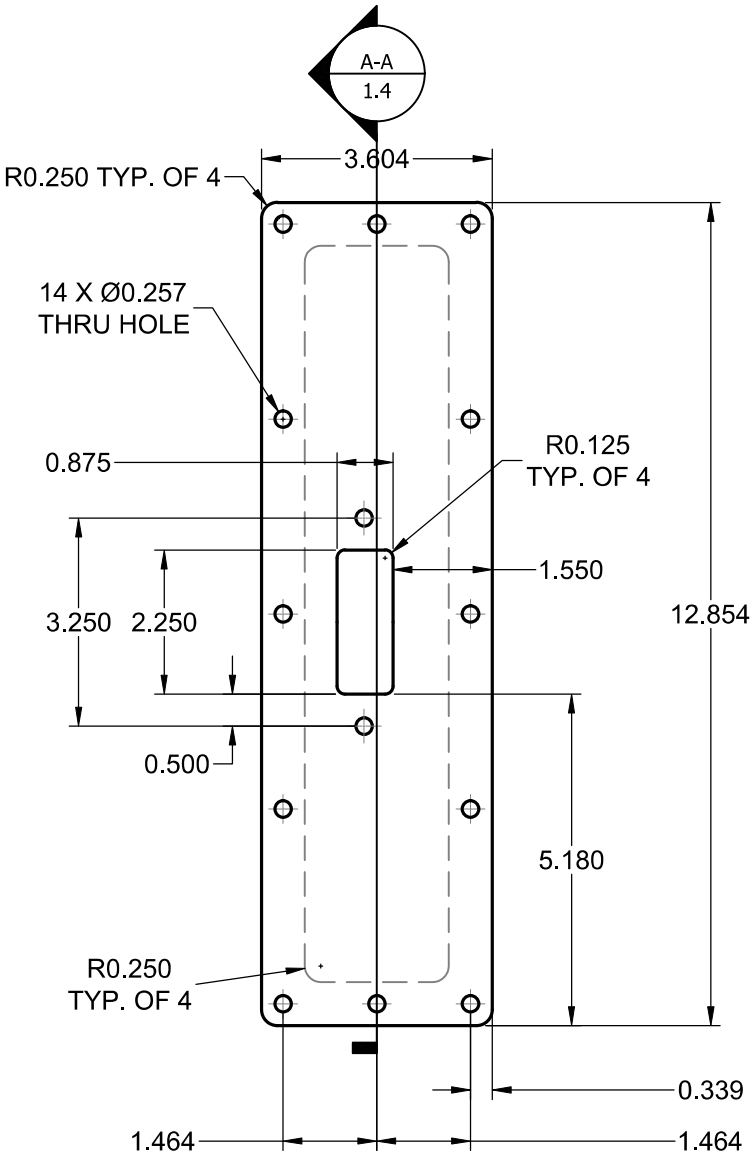

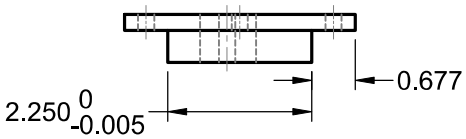

1 1.4 CASCADE COVER

SCALE: 1:3

PROJECT: HIGH-SPEED TEST SECTION	2	16-APRIL-2019	
	3	21-APRIL-2019	
	4	26-APRIL-2019	
	5	29-APRIL-2019	
DRAWING: CASCADE COVER	6	7-MAY-2019	
	7	9-MAY-2019	

SIZE:	MATERIAL:	TOLERANCES:		DESIGN:	DIMENSION: INCHES	QTY: 1
8.5"x11"	AL 6061	+/- 0.005 INCHES		A. BRONIPOLSKY ANDREIBRONIPOLSKY@CMAIL.CARLETON.CA	DRAWING #: 1.4	
				SHEET: 4 OF 12		

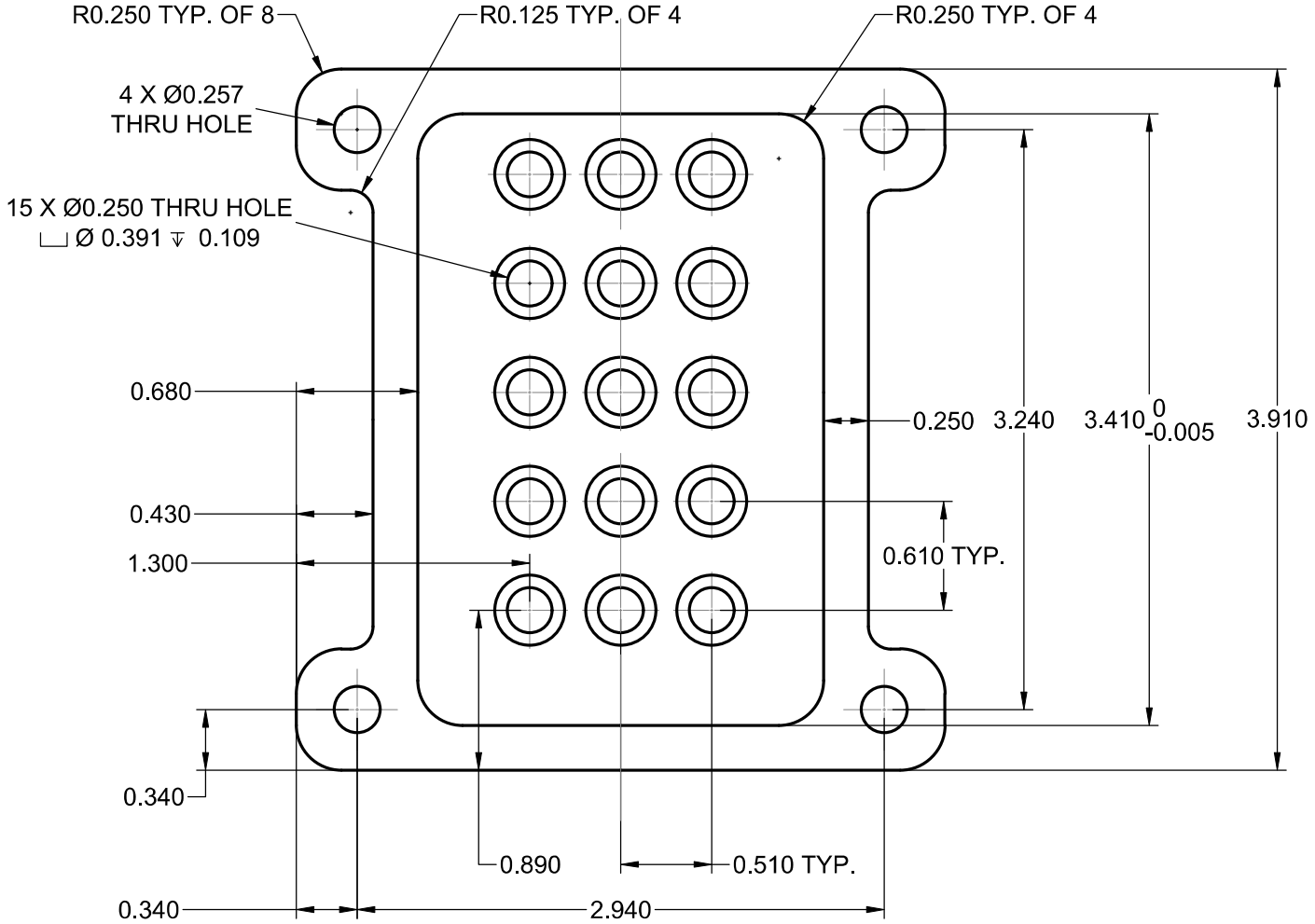

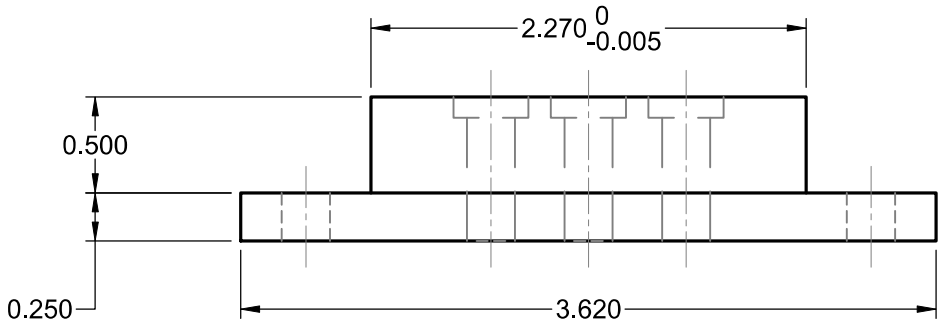

1 / 1.5 STRUT ENDWALL1

SCALE: 1:1

PROJECT: HIGH-SPEED TEST SECTION				2	16-APRIL-2019
				3	21-APRIL-2019
				4	26-APRIL-2019
				5	29-APRIL-2019
DRAWING: STRUT ENDWALL1				6	7-MAY-2019
				7	9-MAY-2019
SIZE: 8.5"x11"	MATERIAL: AL 6061	TOLERANCES: +/- 0.005 INCHES		DESIGN: A. BRONIPOLSKY ANDREIBRONIPOLSKY@CMAIL.CARLETON.CA	DIMENSION: INCHES / QTY: 1
				SHEET: 5 OF 12	DRAWING #: 1.5

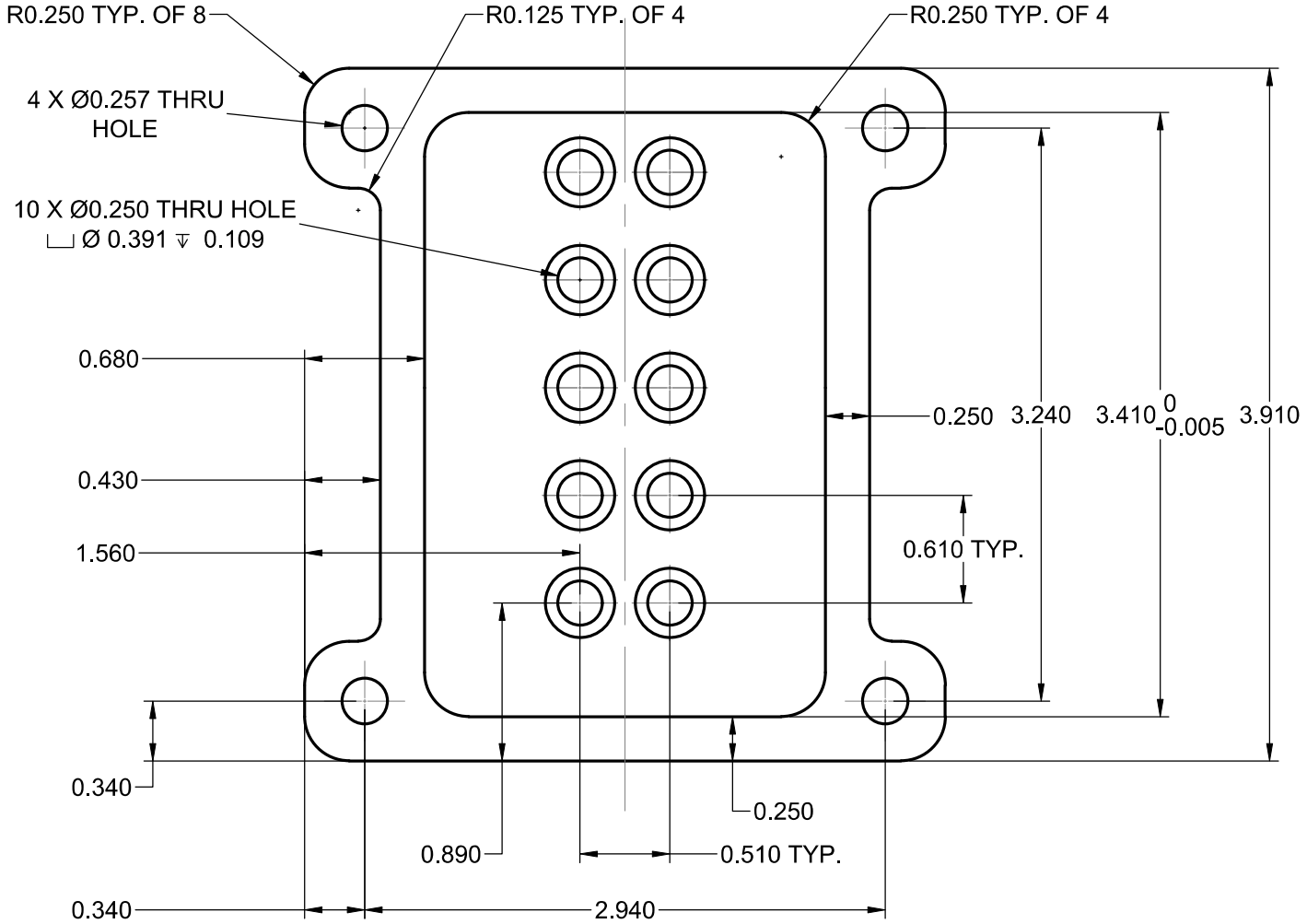

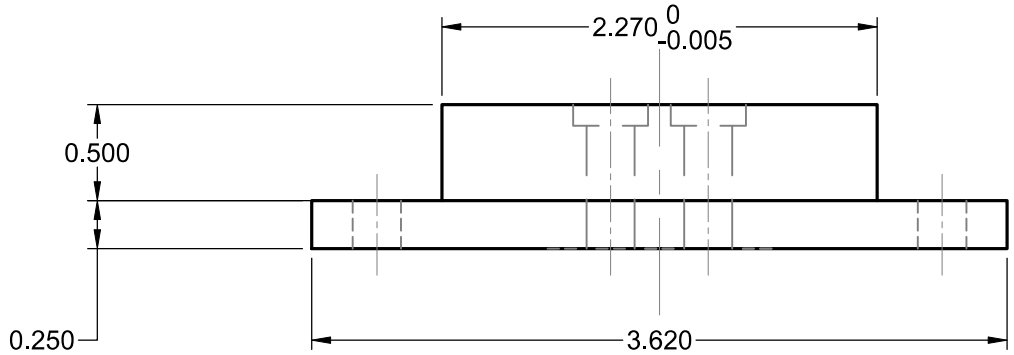

1 / 1.6 STRUT ENDWALL2

SCALE: 1:1

PROJECT: HIGH-SPEED TEST SECTION	2	16-APRIL-2019
	3	21-APRIL-2019
	4	26-APRIL-2019
	5	29-APRIL-2019
DRAWING: STRUT ENDWALL2	6	7-MAY-2019
	7	9-MAY-2019

SIZE:	MATERIAL:	TOLERANCES:		DESIGN:	DIMENSION: INCHES	QTY: 1
8.5"x11"	AL 6061	+/- 0.005 INCHES		A. BRONIPOLSKY ANDREIBRONIPOLSKY@CMAIL.CARLETON.CA	DRAWING #: 1.6	
				SHEET: 6 OF 12		

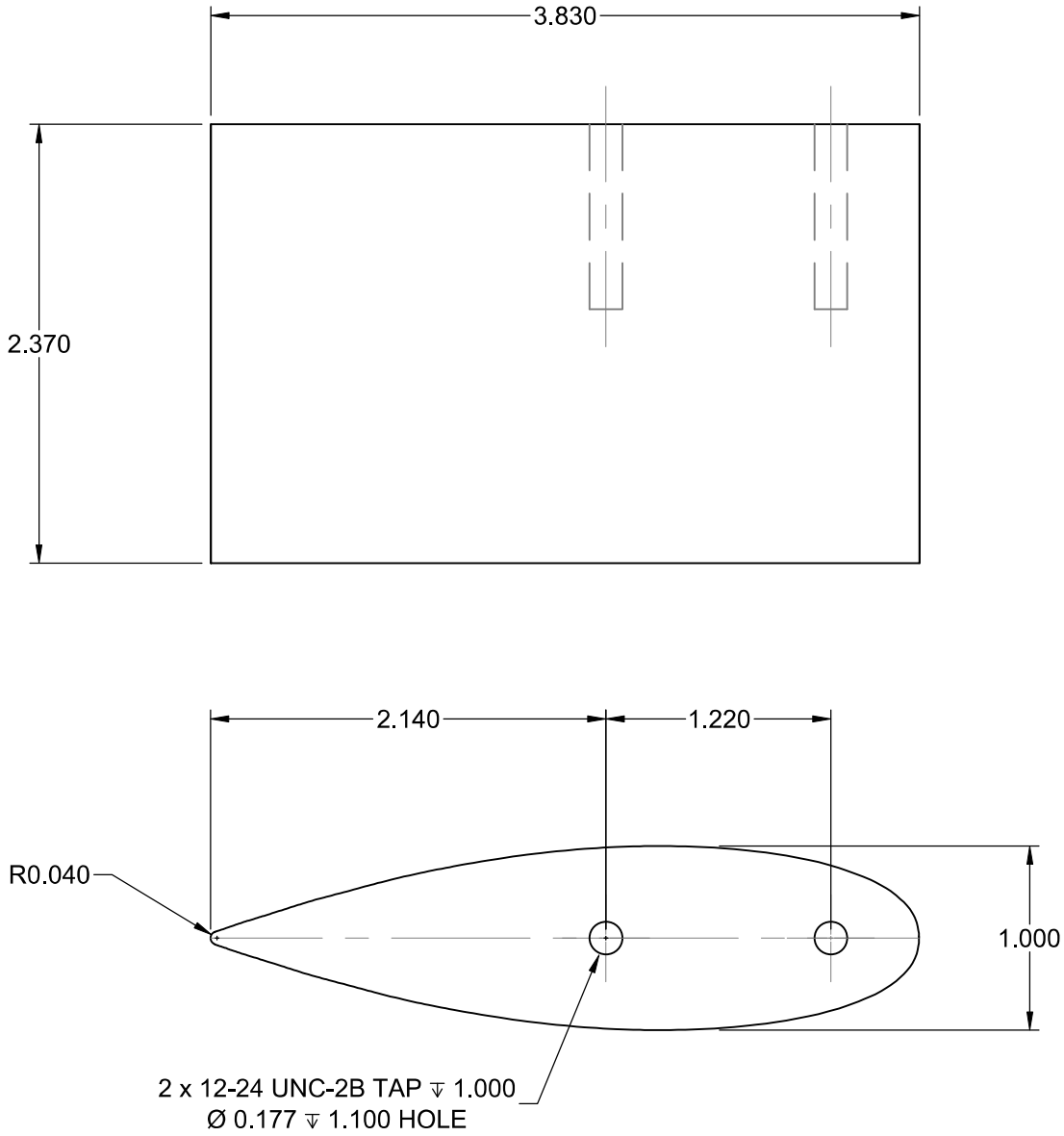

1 / 1.7 HIGH SPEED STRUT

SCALE: 1:1

NOTE
REFER TO APPENDIX C FOR STRUT PROFILE COORDINATES

PROJECT: HIGH-SPEED TEST SECTION				2	16-APRIL-2019
				3	21-APRIL-2019
				4	26-APRIL-2019
				5	29-APRIL-2019
DRAWING: STRUT				6	7-MAY-2019
				7	9-MAY-2019
SIZE: 8.5"x11"	MATERIAL: AL 6061	TOLERANCES: +/- 0.005 INCHES		DESIGN: A. BRONIPOLSKY ANDREIBRONIPOLSKY@CMAIL.CARLETON.CA	DIMENSION: INCHES / QTY: 1
				SHEET: 7 OF 12	DRAWING #: 1.7

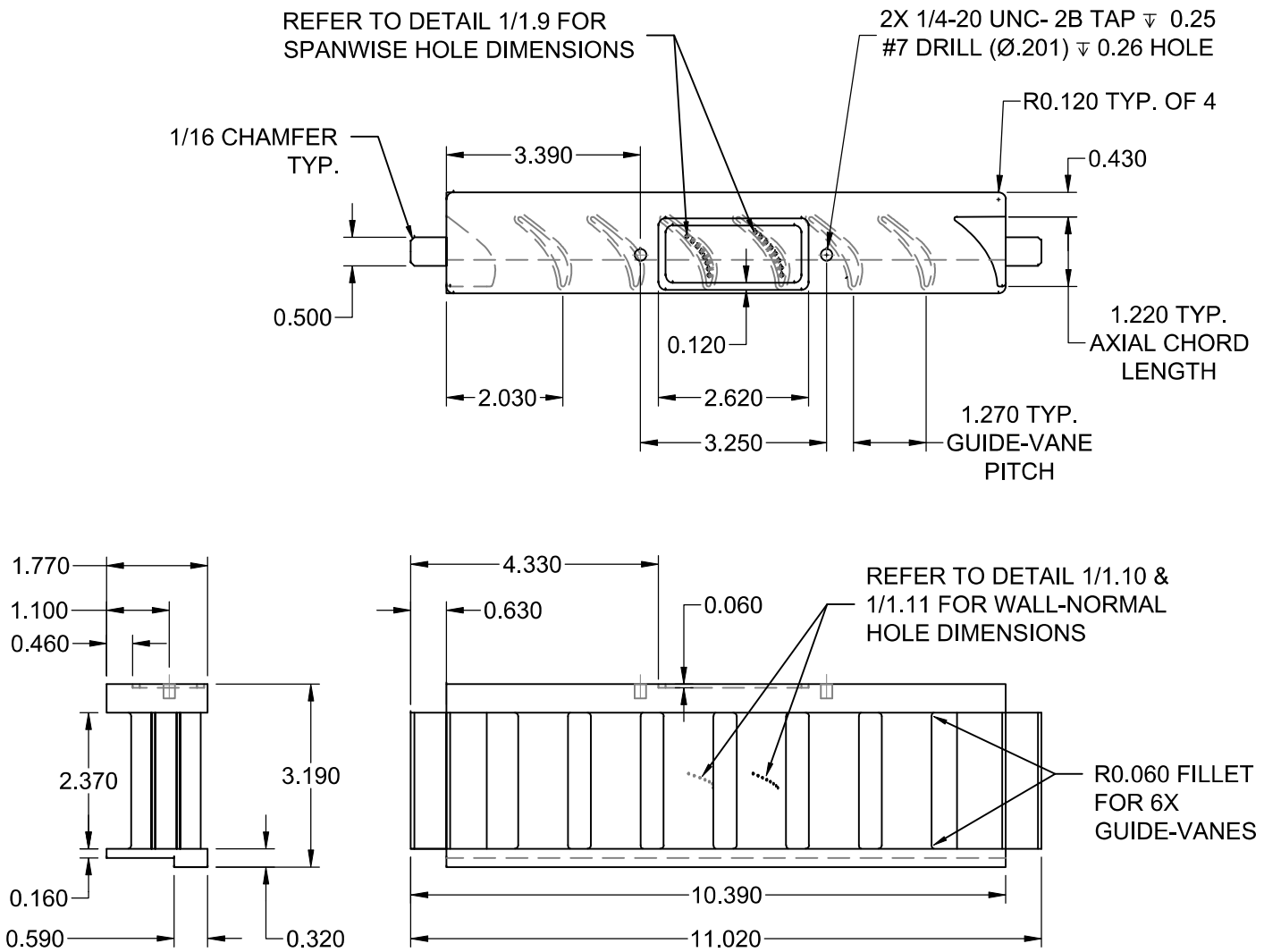

1 / 1.8 HIGH-SPEED GUIDE-VANE CASCADE

SCALE: 1:3

NOTE

REFER TO APPENDIX C FOR VANE GEOMETRY 3 PROFILE COORDINATES

PROJECT: HIGH-SPEED TEST SECTION	2	16-APRIL-2019
	3	21-APRIL-2019
	4	26-APRIL-2019
	5	29-APRIL-2019
DRAWING: GUIDE-VANE CASCADE	6	7-MAY-2019
	7	9-MAY-2019

SIZE:	MATERIAL:	TOLERANCES:		DESIGN:	DIMENSION: INCHES	QTY: 1
8.5"x11"	15-5 PH STAINLESS STEEL	+/- 0.005 INCHES		A. BRONIPOLSKY ANDREIBRONIPOLSKY@CMAIL.CARLETON.CA	DRAWING #: 1.8	
				SHEET: 8 OF 12		

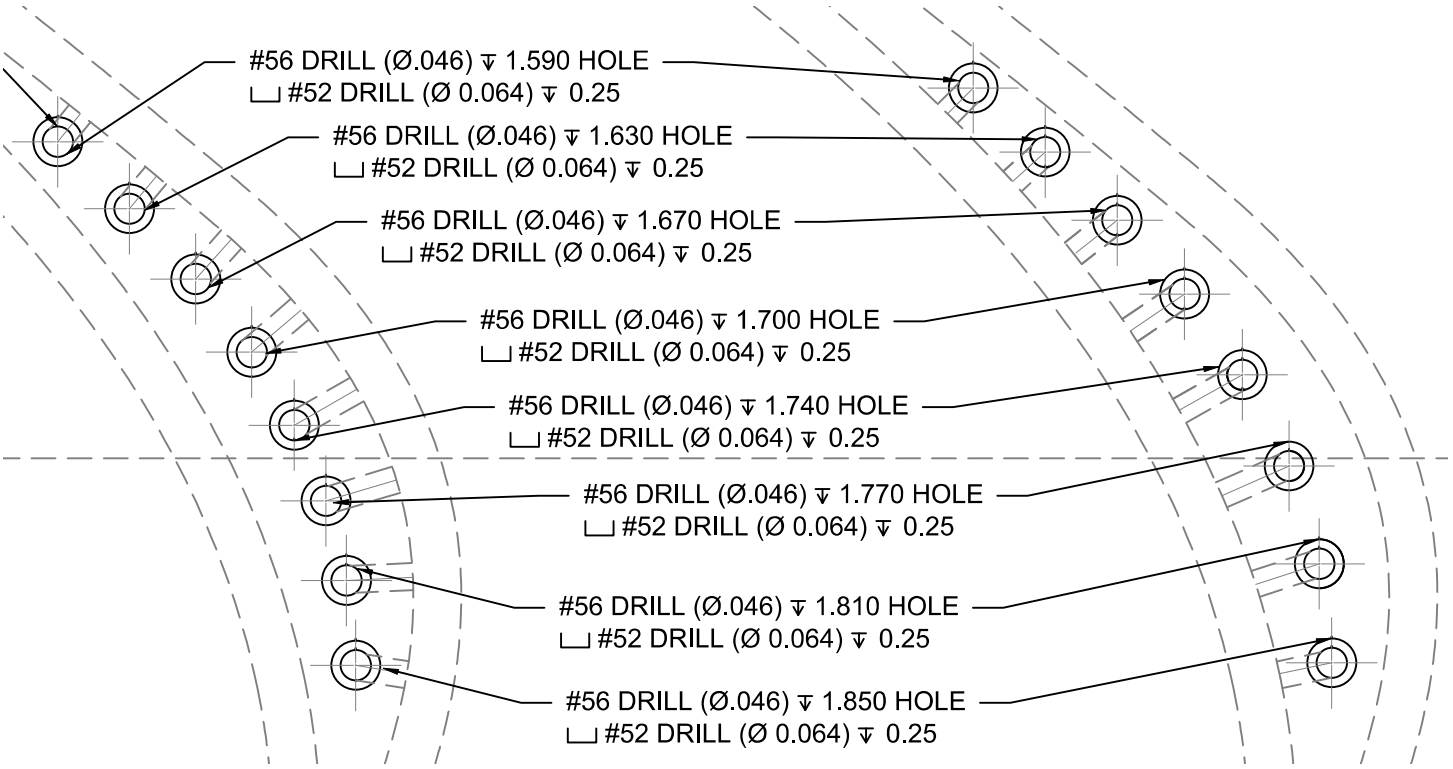

1 / 1.9 SPANWISE HOLES

SCALE: 4:1

PROJECT: HIGH-SPEED TEST SECTION				2	16-APRIL-2019
				3	21-APRIL-2019
				4	26-APRIL-2019
				5	29-APRIL-2019
DRAWING: GUIDE-VANE CASCADE DETAIL 1				6	7-MAY-2019
				7	9-MAY-2019
SIZE: 8.5"x11"	MATERIAL: 15-5 PH STAINLESS STEEL	TOLERANCES: +/- 0.005 INCHES		DESIGN: A. BRONIPOLSKY ANDREIBRONIPOLSKY@CMAIL.CARLETON.CA	DIMENSION: INCHES / QTY: N/A
				SHEET: 9 OF 12	DRAWING #: 1.9

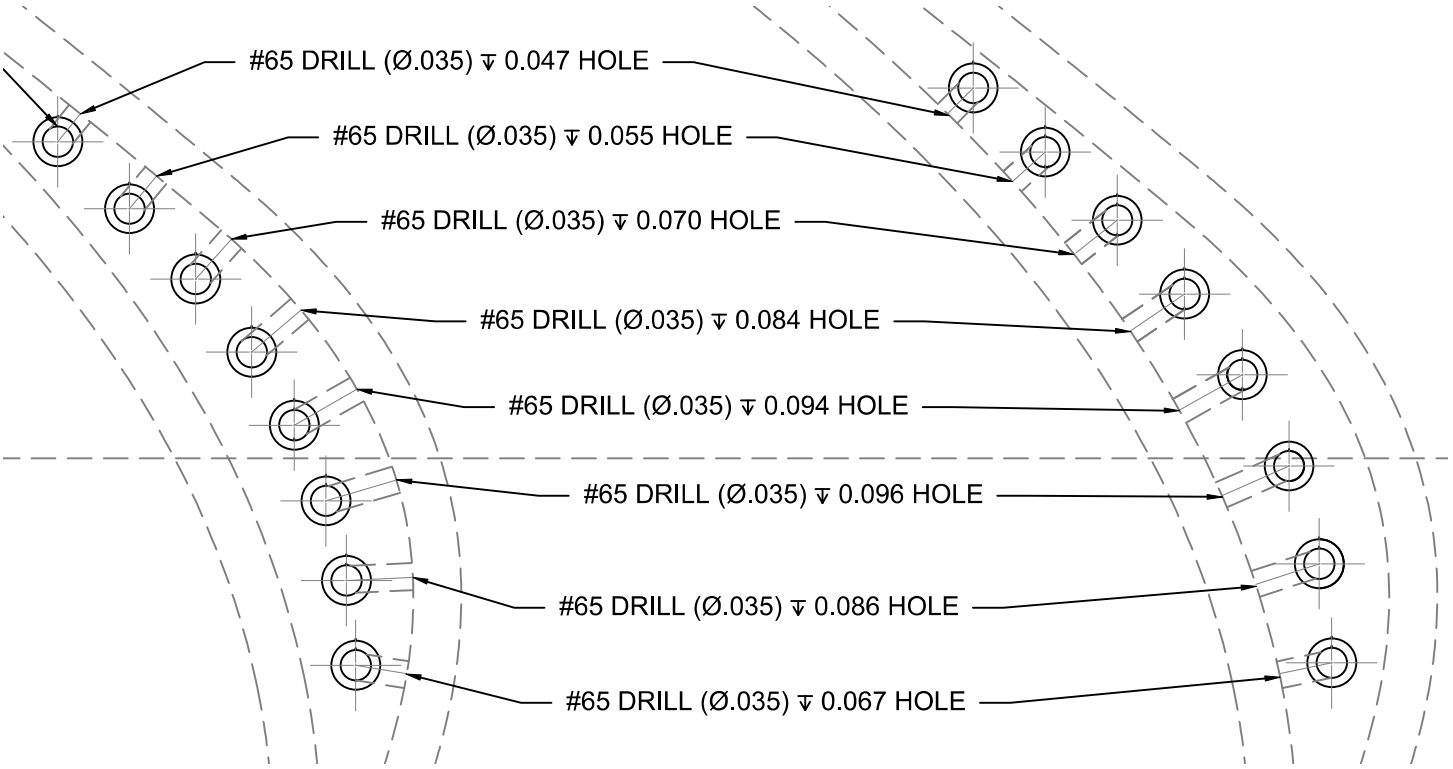

1 / 1.10 WALL-NORMAL HOLES

SCALE: 4:1

PROJECT: HIGH-SPEED TEST SECTION				2	16-APRIL-2019
				3	21-APRIL-2019
				4	26-APRIL-2019
				5	29-APRIL-2019
DRAWING: GUIDE-VANE CASCADE DETAIL 2				6	7-MAY-2019
				7	9-MAY-2019
SIZE: 8.5"x11"	MATERIAL: 15-5 PH STAINLESS STEEL	TOLERANCES: +/- 0.005 INCHES		DESIGN: A. BRONIPOLSKY ANDREIBRONIPOLSKY@CMAIL.CARLETON.CA	DIMENSION: INCHES / QTY: N/A
				SHEET: 10 OF 12	DRAWING #: 1.10

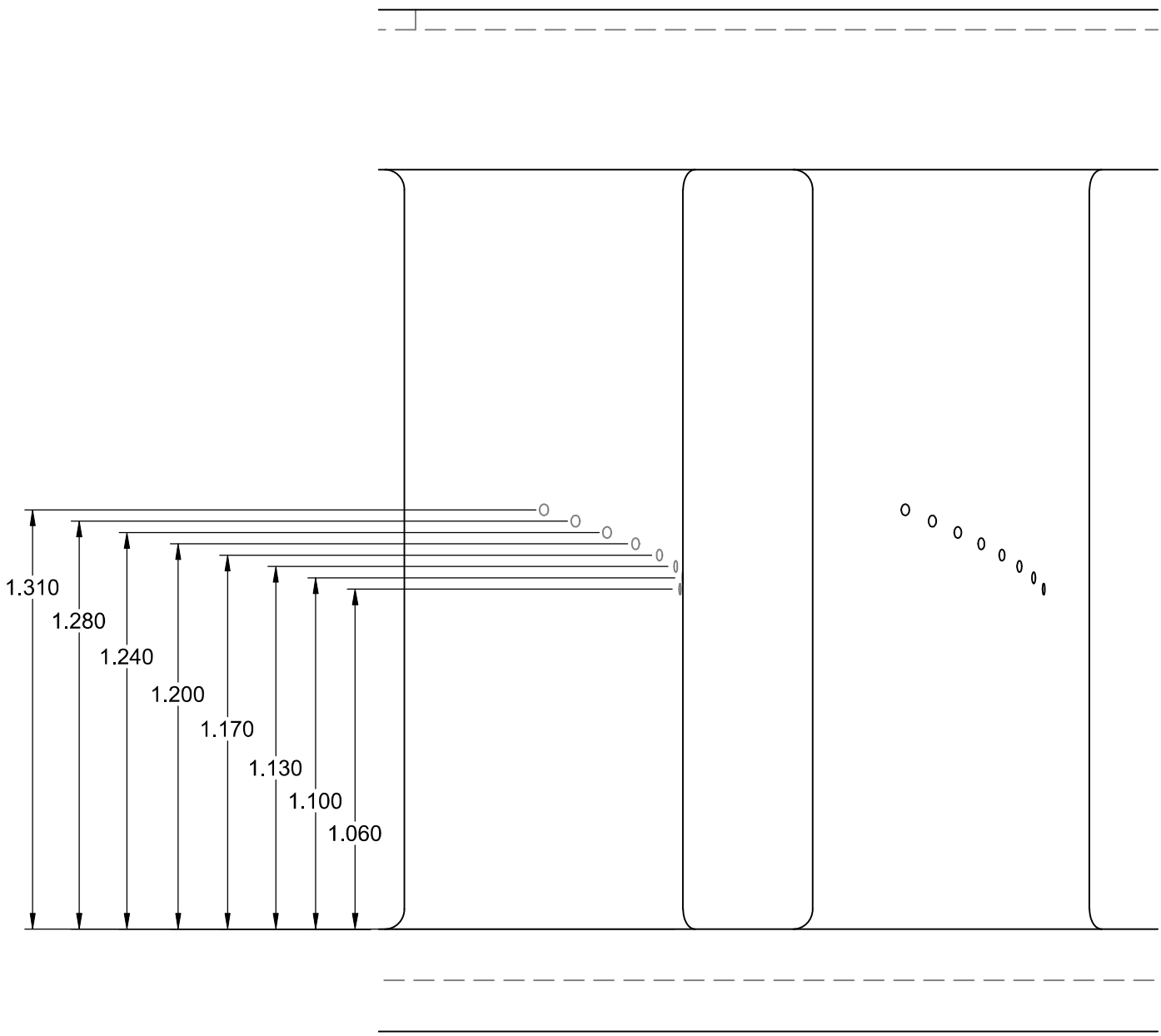

1 / 1.11 WALL-NORMAL HOLES

SCALE: 2:1

PROJECT: HIGH-SPEED TEST SECTION				2	16-APRIL-2019
				3	21-APRIL-2019
				4	26-APRIL-2019
				5	29-APRIL-2019
DRAWING: GUIDE-VANE CASCADE DETAIL 3				6	7-MAY-2019
				7	9-MAY-2019
SIZE: 8.5"x11"	MATERIAL: 15-5 PH STAINLESS STEEL	TOLERANCES: +/- 0.005 INCHES		DESIGN: A. BRONIPOLSKY ANDREIBRONIPOLSKY@CMAIL.CARLETON.CA	DIMENSION: INCHES / QTY: N/A
				SHEET: 11 OF 12	DRAWING #: 1.11

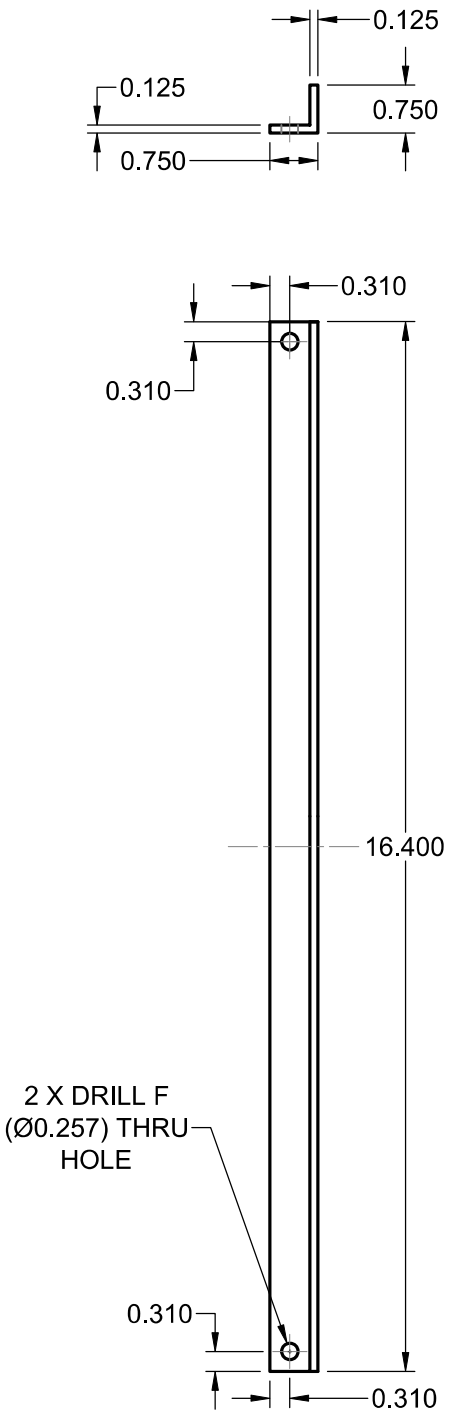

1 / 1.12 ANGLE

SCALE: 1:3

PROJECT: HIGH-SPEED TEST SECTION			2	16-APRIL-2019
			3	21-APRIL-2019
			4	26-APRIL-2019
			5	29-APRIL-2019
DRAWING: 3/4" X 3/4" X 1/8" ANGLE			6	7-MAY-2019
			7	9-MAY-2019
SIZE: 8.5"x11"	MATERIAL: AL 6061	TOLERANCES: +/- 0.005 INCHES	DESIGN: A. BRONIPOLSKY ANDREIBRONIPOLSKY@CMAIL.CARLETON.CA	DIMENSION: INCHES	QTY: 2
			SHEET: 12 OF 12	DRAWING #: 1.12	

Appendix J

High-Speed Cascade Guide-Vane Loading

This chapter presents the methodology used to calculate the anticipated maximum loading experienced by the test-section assembly during operation of the high-speed wind-tunnel at Carleton University. This loading represents the worst-case scenario that is used in the structural analysis as described in Section 5.4. The loading consists of the aerodynamic and static pressure loads applied to the test-section surfaces that are in contact with the high-speed airstream. The cascade vane loading is calculated based on the anticipated normal shock that will propagate downstream through the cascade once the wind-tunnel control valve is opened and the fully pressurized tanks begin discharging. The cascade will experience a sudden load as the shock travels through the vane passages. As shown in Figure J.1, during this period, the shock will not remain normal to the flow direction through the vane passage but will instead rotate in the x-y plane as the shock region in contact with the vane suction surface will accelerate relative to the region in contact with the pressure surface of the adjacent vane. This causes the shock to turn relative to the flow direction and ultimately terminate in a series of oblique shocks near the trailing edge. As a first order approximation, the oblique shocks are ignored and the normal shock relations are applied to calculate the vane

loading.

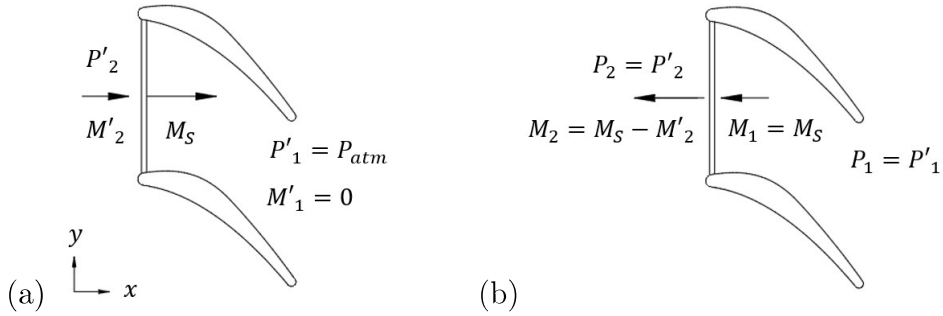

Figure J.1: Travelling shock viewed in (a) stationary frame of reference and (b) shock frame of reference

The air is assumed to travel from the storage tank to the guide-vane cascade inlet with a negligible loss in stagnation pressure, which is a conservative approximation. The static pressure at the cascade inlet, P'_2, is therefore calculated as a function of the fully charged tank stagnation pressure, P'_{o2}, and the upstream Mach number, M'_2, in the stationary frame of reference using the isentropic relation given by:

$$\frac{P'_2}{P'_{o2}} = \left[1 + \frac{(\gamma - 1)}{2} M'_2\right]^{\frac{-\gamma}{\gamma-1}} \tag{J.1}$$

where γ is the specific heat ratio for air. The upstream Mach number, M'_2, in the stationary frame of reference is unknown but can be related to the shock Mach number, M_S, through:

$$M'_2 = M_S - M_2 \tag{J.2}$$

where M_2 is the Mach number in the shock frame of reference as shown in Figure J.1 b). Because M_S is unknown, it is solved iteratively by invoking the

static pressure and Mach number relations across a normal shock given by:

$$\frac{P_2}{P_1} = 1 + \frac{2\gamma M_1^2 - (\gamma - 1)}{\gamma + 1} \tag{J.3}$$

$$M_2 = \frac{(\gamma - 1)M_1^2 + 2}{2\gamma M_1^2 - (\gamma - 1)} \tag{J.4}$$

where M_1 is equal to M_S. The pressure at the cascade exit in both the stationary (P_1') and shock (P_1) frame of reference is conservatively set equal to atmospheric pressure, P_{atm}. By applying this pressure to Eq. J.3, the upstream pressure, P_2, can be calculated and checked against P_2' from Eq. J.1 since both values must be equal for a given value of M_S. Based on the iterative procedure shown in Figure J.2, M_S converges at 1.62 which gives a shock velocity of 562 m/s and a total travel period through the cascade of 5.5×10^{-5} seconds.

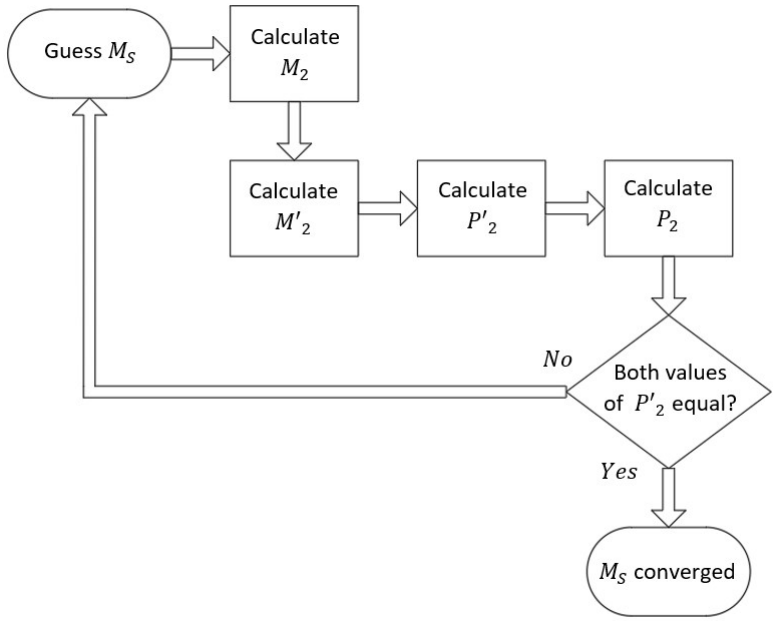

Figure J.2: Shock Mach number calculation

The vane loading is derived from the simulated surface pressure plot presented in Figure 4.6 for Vane Geometry 3 and repeated in Figure J.3. Using the stagnation and static pressure, P'_{o_2} and P'_2, respectively, upstream of the shock for the inlet reference condition, the static pressure distribution acting on both the suction, P_s, and pressure, P_p, surfaces is calculated using Eq. 2.4 and then integrated over the entire guide-vane surface area to produce the axial, F_x, and tangential, F_t, guide-vane loading, respectively, given by:

$$F_x = \int_0^{c_{vx}} P_p cos(\theta_p) h_v dx - \int_0^{c_{vx}} P_s cos(\theta_s) h_v dx \tag{J.5}$$

$$F_t = \int_0^{c_{vx}} P_p sin(\theta_p) h_v dx - \int_0^{c_{vx}} P_s sin(\theta_s) h_v dx \tag{J.6}$$

where, θ_p and θ_s is the vane surface normal angle, along the pressure and

suction surfaces, respectively, and h_v is the guide-vane span. The final vane loading and flow parameters are summarized in Table J.1.

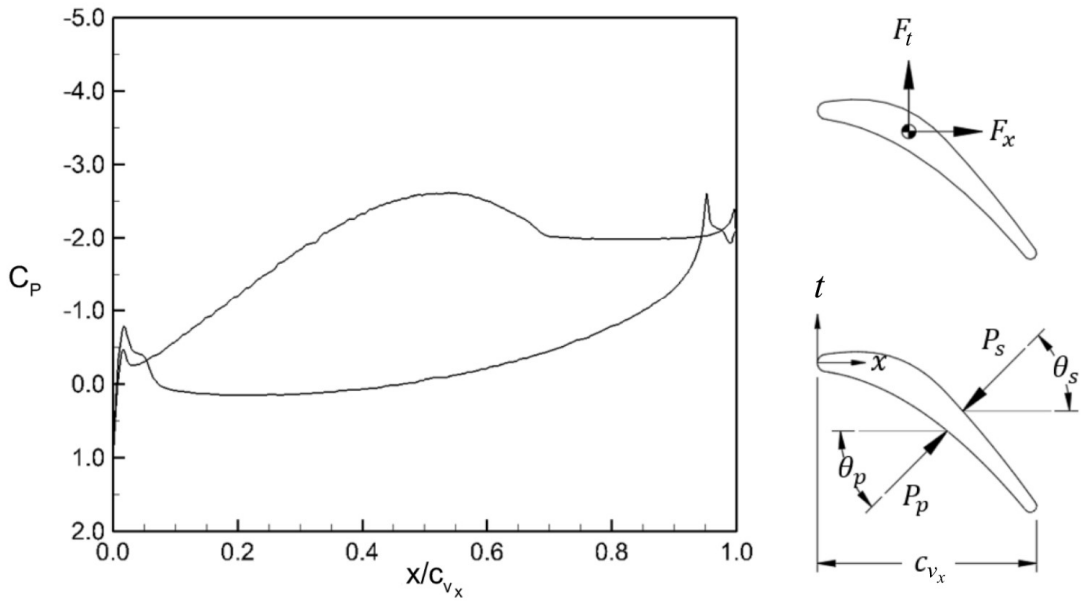

Figure J.3: High-speed cascade guide-vane loading

Table J.1: High-speed wind-tunnel flow parameters used in structural analysis

P_1(Pa)	101,000
P_1'(Pa)	101,000
P_2(Pa)	293,850
P_{o_2}'(Pa)	700,000
P_2'(Pa)	293,850
M_2	0.44
M_2'	1.19
M_S	1.62
F_x(N)	409
F_t(N)	631
F_{total}(N)	752

Appendix K

Additive Manufacturing

This chapter presents a summary of the additive manufacturing (AM) process and the fatigue strength and surface finish of metal parts produced via AM. This review forms the basis of the material and AM process selection for the high-speed cascade that will be subject to high subsonic Mach numbers in the Carleton University high-speed wind-tunnel.

K.1 Additive Manufacturing

AM is a manufacturing process in which parts are fused layer by layer using a localized energy source such as a laser or electron beam. This is in contrast to conventional subtractive manufacturing techniques such as milling and cutting, which require the removal of material for part creation. AM allows for the manufacture of complex geometries including internal channels and cavities while requiring less raw material (Zhang et al., 2018). These manufactured parts, however, possess higher surface roughness, less dimensional accuracy, anisotropic material properties, and porosity when compared to conventionally manufactured parts (Srivatsan and Sudarshan, 2015). AM has been classified according to different groupings including build material, state of the raw material and fusion mechanism (Gibson et al., 2013). In the case of metals,

AM processes are generally grouped into powder bed fusion techniques and direct energy deposition techniques (Gu, 2015; Blinn et al., 2013).

K.2 Powder Bed Fusion

The typical powder bed fusion (PBF) technique is presented in Figure K.1. This process uses a roller to smoothly distribute a thin layer of powder particles across a platform known as a "bed". Particle sizes generally vary between $20 - 100\mu m$ (Leuders, 2018; Kasperovich and Hausmann, 2015; Reimer et al., 2014). An energy source in the form of a laser or electron beam is used to fuse the powder particles either through sintering or melting. The beam traces out the cross section of the part within each layer and then the bed is lowered and the process is repeated. The build area is usually kept at elevated temperatures via an infrared lamp and sealed within an enclosure. Where laser sources are used, the build area is pressurized with an inert shielding gas such as nitrogen or argon. For electron beam sources, the enclosure is held at near-vacuum conditions to prevent interactions between the electrons and surrounding gas. Lasers are more commonly used despite being less energy efficient than electron beams (Gibson et al., 2013). Generally, there are four different fusion mechanisms used in PBF: solid-state sintering, chemically-induced binding, liquid-phase sintering and full melting (Gibson et al., 2013; Kruth et al., 2007). Solid-state sintering is driven by molecular mass diffusion at low temperatures and is often an unintended byproduct in PBF that can lead to undesirable part growth resulting from the fusion of surrounding powder to the outer extremities of the part. Chemically-induced binding is used primarily for ceramic materials and is not applicable to metal powders. Liquid-phase sintering uses a portion of powder particles that become molten

to bind the remaining solid, structural powder particles. Fusion under this mechanism is accomplished due to the different melting points of the binding and structural powders, which are combined either as two sets of particles, composite particles or coated particles (Gibson et al., 2013). In the context of additive manufactured metals such as Titanium, Stainless Steel and Cobalt-based alloys, the full melting mechanism is the most common (Herzog et al., 2016) and will be discussed in greater in detail.

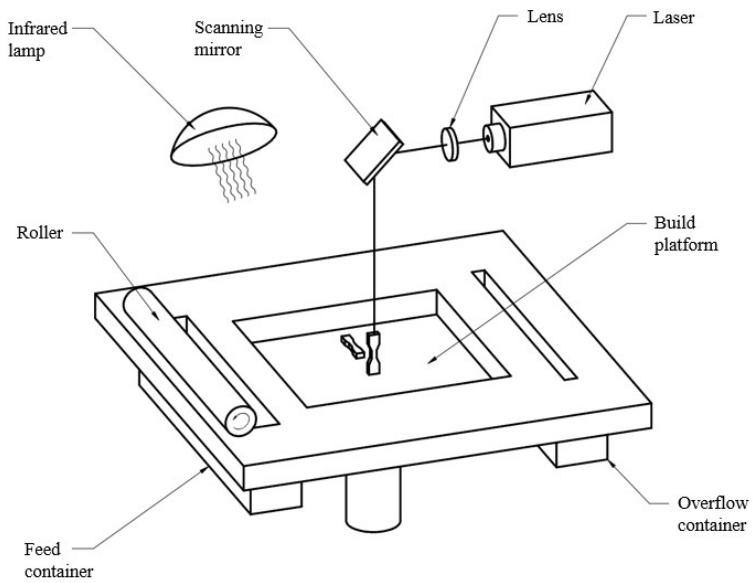

Figure K.1: Typical powder bed fusion setup

K.2.1 Full Melting Mechanism

The full melting mechanism uses higher laser intensities to melt the powder particles at depths exceeding the layer thickness. Several different terminologies exist for this process including Selective Laser Sintering (SLS), Selective Laser Melting (SLM), Direct Metal Laser Sintering (DMLS) and Laser Cusing. The terminology varies between manufacturers; SLM is the most widely cited

in the literature. Full melting of the powder produces nearly 100% dense metal parts with minimal porosity. Kasperovich and Haussmann (2015) measured a minimum relative porosity volume of 0.08% for as-built TiAl6V4 and Leuders (2013) measured a value of 0.23% for the same alloy manufactured using different process parameters (Section K.4). In both cases, porosity was further reduced with post-heat treatment (Section K.5.2). Slotwinski et al. (2014) measured a volumetric porosity range of $0.468 - 16.86\%$ for 40 specimens manufactured at three different scan speeds: 800mm/s, 1600mm/s, 3200mm/s and correlated higher porosity levels with higher scan speeds and larger scan spacing.

The high cooling rates ($10^4 - 10^6 Ks^{-1}$) associated with SLM often result in residual stresses that can distort the final part (Gokuldoss et al., 2017). These stresses are predominantly tensile in the outer part regions and compressive in the interior regions (Li et al., 2018). Mugwagwa et al. (2018) studied distortion in 60mm long cantilered beams manufactured from tool steel powder at scan speeds ranging from 300mm/s to 1000mm/s. A maximum distortion of 1.2mm or 2% of beam length was observed for the least porous ($< 2\%$) specimens. Li et al. (2015) studied curling in rectangular sheets manufactured using different scanning patterns. A maximum curling height of 0.67% of total length was observed for a unidirectional scan pattern oriented parallel to the part length. Generally, residual stresses increase with scan length (Mercelis and Kruth, 2006), making larger parts more susceptible to distortions. Under these conditions, grid based scan patterns have shown to reduce residual stresses (Carter et al., 2012).

K.3 Direct Energy Deposition

The direct energy deposition (DED) mechanism differs from the full melting mechanism employed in PBF by melting the material as it is deposited (Srivatsan and Sudarshan, 2015). The material can be delivered to the source as a powder or a solid via a wire-feed. Similar to PBF, the melting is accomplished with either a laser or electron source. DED is preferable when repairing existing parts, however, it suffers from lower dimensional accuracy and rougher surface finishes when compared to PBF techniques (Sames et al., 2016). As shown in Table 1.1, this shortcoming is largely attributed to the thicker build layer and larger beam spot diameter of DED.

Table K.1: Typical layer thickness and minimum feature size of PBF and DED (adapted from Sames et al., 2016)

Process	**Typical Layer Thickness (μm)**	**Beam Diameter (μm)**
PBF	20-100	75-100
DED - Powder Fed	250	100-200
DED - Wire Fed	3000	16,000

K.4 Process Parameters

Process parameters can be broadly categorized into the following groups: laser-related parameters, scan-related parameters, powder-related parameters and temperature-related parameters (Gibson et al., 2013). Laser parameters refer to the laser power, spot diameter and pulse duration. Scan parameters refer to the scan speed and pattern/spacing. Powder parameters refer to the powder size, shape, layer thickness and material properties. Temperature parameters refer to the powder bed temperature and temperature gradients. The

process parameters are strongly interrelated and their combined effect on the final properties are an ongoing area of research (Gu et al., 2013). Thijs et al. (2010) and others have presented the effect of laser power, scan speed, scan spacing and scan pattern on the microstructure and porosity of additive manufactured metals. The volumetric energy density, VEM, is a commonly used parameter, expressed in J/mm^3, that combines four of the process parameters and is given by:

$$VEM = \frac{P_L}{V_s dt} \tag{K.1}$$

where P_L is the laser power (Watts), V_s is the scan speed (mm/s), d is the hatch spacing (mm) and t is the layer thickness (mm). Despite the exclusion of other important parameters such as the scan pattern and spot diameter, the volumetric energy density is a relatively good indicator of the types of defects that may exist in the completed part (Fayazfar et al., 2018). Lower energy densities lead to insufficient fusion in areas where the powder cannot melt to form a uniform solid (Zhang et al., 2017). These areas are characterized by elongated voids. At higher energy densities, spherical pores form largely as the result of trapped gases that originate in the powder feed stock (Vastola et al., 2018). The irregularly shaped defects associated with lower energy densities are generally more detrimental to the fatigue life of the part (Molaei and Fatemi, 2017). The correlation between volumetric energy density and defect shape has been validated by Gong et al. (2013) and Kasperovich and Hausmann (2015).

K.5 Influences on Fatigue Characteristics

In addition to the process parameters mentioned, other factors such as build direction, post-heat treatment and surface roughness can influence the fatigue characteristics of additive manufactured parts (Afkhami et al., 2019).

K.5.1 Build Orientation

The build orientation of additive manufactured parts affects the cooling rate and hence the final microstructure of the metal (Shrestha et al., 2019). The part strength and fatigue properties are also dependent on the relative orientation of the loading axis. As shown in Figure K.2, when the loading axis is parallel to the build direction, the part is considered vertical, and when the loading axis is normal to the build direction, the part is considered horizontal. Horizontal parts tend to experience higher cooling rates and faster solidification as a result of their higher aspect ratio (d/t), where d is the cross sectional length of a given layer and t is the layer thickness (Yadollahi et al., 2016; Blinn et al., 2018). Higher aspect ratios translate to longer manufacturing time intervals between layers which typically lead to a more refined grain structure and increased strength (Yadollahi et al., 2016).

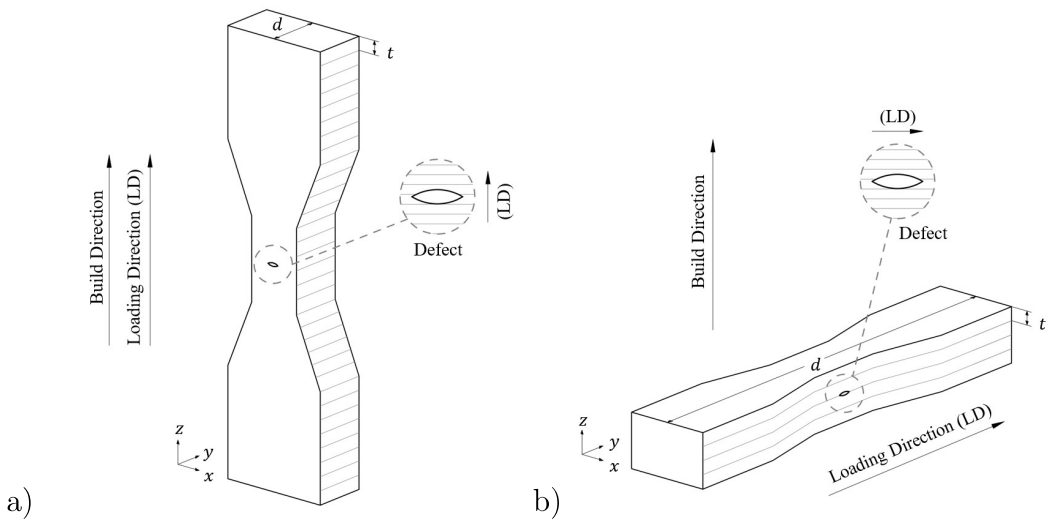

Figure K.2: a) Vertical build and b) Horizontal build

As shown in Table K.2, horizontal parts tend to have higher fatigue strengths, despite generally having a higher percentage of porosity when compared to an equivalent vertical part (Ziolkowski et al., 2014). Vertical parts tend to possess larger sized defects that are unfavourably oriented relative to the loading axis (Yadollahi et al., 2016; Blinn et al., 2018; Ziolkowski et al., 2014). As shown in Figure K.2, the elongated defects resulting from weak interfacial links between layers are present in both horizontal and vertical parts. The highest stress concentrations are located at the defect corners of the vertical part which are orientated normal to the loading axis. This arrangement is more detrimental to fatigue life than in horizontal parts where the defect is oriented parallel to the loading axis (Afkhami et al., 2019).

Table K.2: Fatigue limits of metals manufactured via AM with different build orientations

Material	Mechanism	Fatigue Strength (MPa)	$\sigma_{min/max}$	Orientation	Reference
Ti-6Al-4V	Wrought	650	-1.0 at 10^7 cycles	–	Mower et al. (2016)
	DMLS	400		V (HIP & Machined)	
	DMLS	400		H (HIP & Machined)	
Ti-6Al-4V	Wrought	670	-0.2 at 0.2 x 10^6 cycles	–	Edwards & Ramulu (2013)
	SLM	100		V	
	SLM	170		H	
Ti-6Al-4V	EBM	390	0.1 at 10^7 cycles	V	Svensson & Ackelid (2010)
		450		H	
Ti-6Al-4V	EBM	540	0.1 at 10^7 cycles	V(HIP)	Svensson & Ackelid (2010)
		550		H(HIP)	
316L	Wrought	340	-1.0 at 10^7 cycles	–	Mower et al. (2016)
	DMLS	150		V	
	DMLS	280		H	
17-4PH	Wrought	450	-1.0 at 10^7 cycles	–	Mower et al. (2016)
	DMLS	110-270		V	
	DMLS	440		H	
15-5PH	DMLS	507	-1.0 at 10^7 cycles	V	Croccolo et al. (2017)
	DMLS	480		H	
	DMLS	690		45°	

H = Horizontal

HIP = Hot Isostatic Pressing(Subsection K.5.2)

$\sigma_{min/max}$ = Stress Ratio

V = Vertical

K.5.2 Heat Treatment

Residual stresses in additive manufactured metals are often detrimental to the fatigue strength (Leuders, 2013; Li et al., 2018). To mitigate this, the bed

temperature can be kept near the powder melting point during manufacturing (Ali et al., 2017). Alternatively, post-processing heat treatments such as annealing and hot isostatic pressing (HIP) can be applied to the part. The exact treatment must be tailored to each metal to accommodate its different strengthening mechanisms based on grain structure, martensitic content and precipation hardening (Afkhnami et al., 2018). Incorrect treatments can reduce fatigue life, as demonstrated by Yadollahi et al. (2017) who observed a reduction in high cycle fatigue strength of 17-4 PH Stainless Steel, caused by precipitation hardening after heat treatment. According to Leuders et al. (2013) and Kasperovich and Hausmann (2015), improvements in fatigue strength can only be achieved with significant reductions in porosity. This is normally accomplished through hot isostatic pressing which involves heating the metal under pressure. Table K.3 presents a sample of studies comparing fatigue strengths between as-built and heat treated additive manufactured metals.

Table K.3: Fatigue endurance limits of AM steels with post-heat treatments

Material	Mechanism	Fatigue Strength/Life	$\sigma_{min/max}$	Heat Treatment	Reference
Ti-6Al-4V	SLM	27 x 10^3 cycles	-1.0 at σ_a = 600 MPa	As built	Leuders et al. (2013)
		93 x 10^3 cycles		800°C for 2h	
		290 x 10^3 cycles		1050°C for 2h	
		>2000 x 10^3 cycles		920°C at 100 MPa for 2h	
Ti-6Al-4V	EBM	200 MPa	0.1 at 10^7 cycles	As built	Hrabe et al. (2017)
		250 MPa		650°C for 5h in air	
		550 MPa		900°C, argon at 100 MPa for 2h	
Ti-6Al-4V	SLM	29 x 10^3 cycles	-1.0 at σ_a = 600 MPa	As built	Thone et al. (2012)
		93 x 10^3 cycles		800°C for 2h	
		290 x 10^3 cycles		1050°C for 2h	
		>2000 x 10^3 cycles		920°C at 100 MPa for 2h	
Ti-6Al-4V	EBM	296 MPa	-1.0 at 10^7 cycles	As built	Svensson & Ackelid (2010)
		518 MPa		HIP	
316L S.S.	SLM	267 MPa	-1.0 at 2 x 10^6 cycles	As built & Machined	Riemer et al. (2017)
		294 MPa		650°C for 2h & Machined	
		317 MPa		1150°C at 100 MPa for 4h & Machined	
AlSi10Mg	SLM	2 x 10^5 cycles	0.1 at σ_a = 126 MPa	As built	Aboulkhair et al. (2017)
		3 x 10^6 cycles		520°C for 1h, quenched & aged for 6h at 520°C	

EBM = Electron Beam Melting

$\sigma_{min/max}$ = Stress Ratio

σ_a = Stress Amplitude

K.5.3 Surface Roughness

Additive manufactured metals generally suffer from rougher surface finishes in comparison to their wrought counterparts (Srivatsan and Sudarshan, 2015). This is largely attributed to the partially melted or unmelted powder particles on the surface which act as crack initiation sites leading to reduced fatigue life (Chan et al., 2013). As shown in Table K.4, conventional smoothing techniques such as machining and media blasting can improve the high cycle fatigue of additive manufactured metals.

Table K.4: Fatigue endurance limits of AM steels with varying surface finishes

Material	Mechanism	Fatigue Strength/Life	$\sigma_{min/max}$	Surface Finish	R_a (μm)	Reference
Ti-6Al-4V	SLM	210 MPa	0.1 at 10^7 cycles	As-built	13	Wycisk et al.(2013)
		510 MPa		Polished	0.5	
		435 MPa		Shot-Peened	2.9	
Ti-6Al-4V	SLM	60 x 10^3 cycles	0.1 at σ_a=600 MPa	As-built	38.5	Chan et al.(2013)
		80 x 10^3 cycles		EDM	7.67	
Ti-6Al-4V	EBM	30 x 10^3 cycles	0.1 at σ_a=600 MPa	As-built	131.43	Chan et al.(2013)
		50 x 10^3 cycles		EDM	5.12	
S316L	SLM	130 MPa	-1.0 at 10^6 cycles	As-built	13.29	Uhlmann et al.(2017)
		170 MPa		VF	1.74	
		240 MPa		Machined	1.08	
S316L	SLM	200 MPa	0.1 at 10^6 cycles	As-built	10.0	Spierings et al.(2013)
		256 MPa		Machined	0.4	
		269 MPa		Polished	0.1	
630	SLM	219 MPa	0.1 at 10^6 cycles	As-built	13.7	Stoffregen et al.(2014)
		492 MPa		Machined	0.2	

EBM = Electron Beam Melting

EDM = Electrodischarging machining

$\sigma_{min/max}$ = Stress Ratio

VF = Vibratory Finish

σ_a = Stress Amplitude

K.6 Applicability to the High-Speed Guide-vane Cascade

Based on Tables K.2 - K.4, the lowest fatigue limit of any metal material in the literature is on the order of 30 x 10^3 cycles making the fatigue limit inconsequential to the material selection criteria for the high-speed cascade, given that the cascade will be subjected to no more than 1000 aerodynamic load

cycles in the Carleton University high-speed wind-tunnel. The selection of the cascade material is thus largely a function of the yield strength and minimum achievable surface roughness. The material must be capable of withstanding the aerodynamic loads in the wind-tunnel while having a smooth surface finish to prevent influencing the aerodynamics of the guide-vanes. For this reason, the cascade was chosen to be manufactured using a powder bed fusion process followed by post-manufacturing surface treatment to ensure an aerodynamically smooth surface. Aerodynamic smoothness is achieved when the surface roughness elements of the finished material lie entirely within the viscous sublayer of the developing turbulent boundary layer on the guide-vane surface. Due to the wide variation in surface topographies, there is no general agreement on a single parameter to quantify the surface roughness in the context of its aerodynamic effects. The most commonly used parameter is the equivalent sand-grain roughness height, k_s, proposed by Schlicting (1936). This roughness height is based on the data of Nikuradse (1933) who measured skin friction losses through roughened pipes lined with sand-grains of a known diameter. Schlicting (1936) used this data to correlate different types of roughness such as rivets and bumps to the sand-grain roughness of Nikuradse (1933). The equivalent sand-grain diameter proposed by Schlicting (1936) can be extended to flow over an airfoil using the following expression:

$$\frac{k_{s,adm}}{c} \leq \frac{100}{Re_c} \tag{K.2}$$

where $k_{s,adm}$ is the maximum admissible sand-grain roughness height that is fully contained in the viscous sublayer, c is the chord length, and Re_c is the chord-based Reynolds number. Eqn K.2 is commonly used to establish whether the surface of an airfoil qualifies as aerodynamically smooth. Because k_s is not

a true physical dimension that can be measured using either profile (2D) or areal-based (3D) methods, different measurable parameters are used instead, such as the average roughness height, R_a, the rms roughness, R_q, and to a lesser extent, the average peak to valley roughness height, R_z. Other parameters such as kurtosis and skewness are also sometimes used. Numerous correlations have been developed for gas-turbine engines to relate the measurable roughness parameters to k_s. Bons (2010) provides a summary of these correlations which vary significantly as given by:

$$1 < \frac{k_s}{R_a} < 10 \tag{K.3}$$

$$2.1 < \frac{k_s}{R_q} < 4.8 \tag{K.4}$$

$$0.2 < \frac{k_s}{R_z} < 3.5 \tag{K.5}$$

Typically, material data sheets for additive manufactured parts present the surface roughness after media blasting or polishing. Table K.5 presents the surface roughness and yield strength of metal alloys manufactured using a common, modern brand of metal-based additive manufacturing system, the EOS 290.

Table K.5: Material properties of additive manufactured metals using the EOS 290 "printer"

Metal	**Surface Roughness (μm)**		**Yield Strength* (MPa)**	**Build Direction**
AlSi10Mg	Shot-peened	$R_a = 7 - 10$ $R_z = 50 - 60$	240±10	Vertical
S.S. 316L	Shot-peened	$R_a = 5\pm2$ $R_z = 30\pm10$	470	Vertical
	Polished	$R_z < 1$		
S.S. 15-5PH	Shot-peened	$R_a \approx 5$ $R_z \approx 25$	930±75	Vertical
	Polished	$R_z < 0.5$		
S.S. 17-4PH	Shot-peened	$R_a = 7.5$ $R_z = 40$	720	Vertical
Ti6Al4V	Shot-peened	$R_a = 5 - 9$ $R_z = 20 - 50$	965	Vertical

*As built

Based on the properties listed in Table K.5, 15-5PH Stainless Steel was chosen to be the most suitable material for the high-speed guide-vane cascade. This metal offers comparatively higher strength, minimal distortion (<0.2%), and the lowest possible surface roughness. Based on a maximum average peak-to-valley roughness height of $R_z = 0.5\mu m$ for polished, 15-5PH Stainless Steel as listed in Table K.5, a conservative estimate of the equivalent sand-grain diameter was calculated using Eqn K.5 to be $k_s = 3.5R_z$. This corresponds to a normalized sand-grain roughness height of $k^+ < 5$ which satisfies the minimum requirements for an aerodynamically smooth surface.